



**HAL**  
open science

# Single shot lensless imaging with coherence and wavefront characterization of harmonic and FEL sources

Aura Inés Gonzalez Angarita

► **To cite this version:**

Aura Inés Gonzalez Angarita. Single shot lensless imaging with coherence and wavefront characterization of harmonic and FEL sources. Physics [physics]. Université Paris Sud - Paris XI, 2015. English. NNT : 2015PA112055 . tel-01309808

**HAL Id: tel-01309808**

**<https://theses.hal.science/tel-01309808>**

Submitted on 1 May 2016

**HAL** is a multi-disciplinary open access archive for the deposit and dissemination of scientific research documents, whether they are published or not. The documents may come from teaching and research institutions in France or abroad, or from public or private research centers.

L'archive ouverte pluridisciplinaire **HAL**, est destinée au dépôt et à la diffusion de documents scientifiques de niveau recherche, publiés ou non, émanant des établissements d'enseignement et de recherche français ou étrangers, des laboratoires publics ou privés.



UNIVERSITÉ PARIS-SUD

ÉCOLE DOCTORALE 288:  
ONDES ET MATIÈRE

Effectuée au: Laboratoire Interactions, Dynamique et Lasers, IRAMIS, DSM  
Commissariat à l'Énergie Atomique, Saclay.

## THÈSE DE DOCTORAT

PHYSIQUE

Présentée par

**AURA INES GONZALEZ ANGARITA**

Single shot Lensless Imaging with coherence and  
wavefront characterization of harmonic and FEL  
sources

**Date de soutenance:** 14/04/2015

**Composition du jury:**

Directeur de thèse:	M. Hamed MERDJI	Ingénieur de Recherche CEA (LIDyL-CEA)
Rapporteurs:	M. Eric MEVEL	Professeur (CELIA, Université Bordeaux)
	M. Sylvain RAVY	Directeur de recherche CNRS (Université Paris-Sud)
Examineurs:	M. Marc HANNA	Chargé de recherche CNRS (Institut d'Optique)
	M. Gilles MAYNARD	Directeur de recherche CNRS (Université Paris-sud)
	M. Jérôme PRIMOT	Directeur de recherche ONERA (ONERA - DOTA)



SINGLE SHOT LENSLESS IMAGING WITH COHERENCE AND WAVEFRONT CHARACTERIZATION  
OF HARMONIC AND FEL SOURCES

© 2015 Aura Gonzalez  
All rights reserved  
Printed in Paris, 2015

Commissariat à l'Énergie Atomique  
Direction Science de la Matière  
Institut Rayonnement Matière Saclay  
Laboratoire Interactions, Dynamique et Lasers  
Bâtiment 522  
F-91191 Gif-sur-Yvette  
France

<http://iramis.cea.fr/LIDyL/>

This thesis was typeset with the  $\text{\LaTeX}$ -system and the memoir class, using a model developed by the smart people of the Atomfysik division at Lund University.

*El propósito que lo guiaba no era imposible, aunque sí sobrenatural. Quería soñar un hombre: quería soñarlo con integridad minuciosa e imponerlo a la realidad. Ese proyecto mágico había agotado el espacio entero de su alma...*

Jorge Luis Borges. (Las ruinas circulares)

*A Filomena y Héctor. Mis padres.*

# ACKNOWLEDGMENTS

---

This thesis started with the wish of moving out of my “known universe” to explore new applications of coherent radiation (and it finished with more than coherence). I want to thank all the people that helped me with the initial decision. First of all, I want to thank my family for the encouragement and endless love. To my mother, for her huge effort and for our successful project of creating new dimensions that allowed us to stay together.

To my advisor, Hamed Merdji, thanks for sharing with me the opportunity to work in the Attophysics group at CEA-Saclay. Thanks for your support during my thesis and for the continuous ideas of collaborations in different projects. This thesis is the result of these numerous collaborations.

I want to start by thanking the members of the Attophysics group. The work at CEA has been done between helpful colleagues that were willing to share their knowledge with me in a friendly atmosphere (and imaginary Cowboys fights on the corridor).

To Willem Boutu, thanks for the long discussions about my work. Thanks for keeping a chair next to your desk to listen to the day to day reasoning of this PhD student; sometimes full of incoherence but with the hope of improving it by propagation (that reminds me to thank you for laughing at my bad jokes). To Bertrand Carré for following attentively the evolution of my work and sharing some long nights of data acquisition (with cheese, bread and transport included). To Pascal Salieres, thanks for making me part of the ATTOFEL network. The participation in this Marie Curie Action network was an exceptional academic experience. To Thierry Ruchon for the discussions about attosecond generation (I have the feeling that in a future I could even work as a post doc with you).

In an experimental thesis we have to build real experiments. Luckily, I had the constant help of Marc Billon, Gilles Le Chevalier, Sara Kieffer, André Fillon, Didier Guyader for the technical support. And a great laser team: Olivier Gobert, Michel Perdrix and Delphine Guillaumet, thanks for your essential help.

I also want to thank the administrators Veronique Gerecny and Jacqueline Bandura, for these hundreds of documents that allowed me each year to have a pink document to stay in France, to have health insurance. . . and all these “little details” that are needed to live in this world.

To the post docs, that worked with me in different projects. Thanks to Anna Borta and

Benjamin Barbrel (for the hard work to allow that 1% of nanometer movement). To Mathieu Ducouso (for teaching me about networking). To Bianca Iwan, you not only shared the same vocation as Willem, to listen to me for hours, you also helped me with meaningful advises for this manuscript.

Equally, I want to thank the PhD students that worked with me, David Gauthier (Finalement, “Je parle français... un peu mieux”), Xunyou Ge (who wanted to implement a biological solution for beam stabilization), Fan Wang (for sharing these long beamtimes at CEA), Julien Samaan (Mais, il est où Julien?). To the PhD students from the “ATTO-part”, Nan Lin, Antoine Camper, Vincent Gruson and Romain Geneaux for sharing the lab and the laser with me (and sometimes sharing some refreshing beverages to celebrate the week of hard work). I also want to thank the PhD students that arrived at the end of my thesis, Remy Cassin, Dominik Franz and Lou Barreau for the discussions and laughs.

I thank the different groups that I have had the fortune to work with. In chronological order, to Phil Bucksbaum’s group at PULSE Institute - Stanford, in particular to Douglas Broege (thanks for teaching me about ultrafast absorption), to James Cryan and James Glowonia (for the laser and the discussions at lunch), to James White (thanks for Aura’s room, the afternoons playing with Miu and the talks with your family). To the group of Philippe Zeitoun à LOA-ENSTA, with whom I had the opportunity to collaborate on different projects. To Jacek Krywinsky and John Bozek from AMO station at LCLS, thanks for sharing your machine time with me. To the group of Franck Fortuna at the CSNSM (Orsay), particularly to Laurent Delbecq et Cedric Baumier, thanks for teaching me to do nano-objects with the focused ion beam. To the group of Marta Fajardo at IST, Portugal, particularly to Gareth Williams and Swen Künzel, many thanks for the different projects that we worked on together. To Giovany de Ninno from FERMI-ELETTRA, thanks for the beam time at ELETTRA. To Guillaume Dovillaire and Samuel Bucourt from Imaging Optic, thanks for your support.

I want to thank the members of the jury Eric Mevel, Sylvain Ravy, Marc Hanna, Guilles Maynard and Jérôme Primot for accepting to review my thesis, and for their essential remarks to my work.

To my friends (the ones out of the lab), all my gratitude for these years of great times. To Viviana Dionicio, Viviana Agudelo, Luisa Castillo, thanks for sharing your madness with me. To Julian Lopez, for the emergency calls. To Yobani Mejia, Oscar Rincón, Yaneth Marcela and Ricardo Amezaquita for long discussions on optics and life. To Doris Cadavid, for the essential coffee times on skype and the visit in Paris. To Mario Zapata, for the discussions about life and research. To “Les soirées du 120 bis” for the great times in Paris.

Finally, to the person that shares the hobby of imagination with me. That shares with me his love, smiles and dreams. Te amo Thimothée.

# CONTENTS

---

---

<b>Acknowledgments</b>	<b>v</b>
<b>Introduction</b>	<b>1</b>
<b>1 Single shot characterization of XUV spatial coherence</b>	<b>13</b>
1.1 Characterization of single pulse spatial coherence of HH and FEL sources . . . . .	15
1.1.1 Description of the method . . . . .	16
1.1.2 Accumulation . . . . .	20
1.2 Experimental results with HH sources . . . . .	23
1.3 Extension of single shot method to the Fresnel regime . . . . .	30
1.4 Partially coherent holographic imaging . . . . .	32
1.5 Conclusions . . . . .	37
<b>2 Soft X-ray wavefront characterization and applications</b>	<b>39</b>
2.1 Wavefront characterization with a Hartmann sensor . . . . .	40
2.2 Optimization of soft and hard X-ray focusing systems . . . . .	42
2.2.1 Experimental results at AMO-LCLS . . . . .	45
2.2.2 Experimental results at FERMI ELETTRA . . . . .	48
2.3 Sensing FEL plasma dynamics via wavefront measurements . . . . .	55
2.4 Conclusions . . . . .	60
<b>3 3D Stereo setup imaging with harmonic sources</b>	<b>63</b>
3.1 High harmonic beamline . . . . .	65
3.2 Two sources stereo lensless setup . . . . .	67
3.2.1 Two parallel plates setup . . . . .	67
3.2.2 Prism setup . . . . .	75
3.3 Conclusions . . . . .	78
<b>4 Multi wavelength lensless imaging</b>	<b>79</b>
4.1 Imaging with multiple harmonic orders . . . . .	80
4.2 Experimental demonstration of multiple wavelengths holographic imaging . . . . .	87
4.2.1 Experimental setup . . . . .	87
4.2.2 Spectrally resolved results . . . . .	88
4.2.3 Broadband overlapped reconstruction . . . . .	92

4.3	Conclusions . . . . .	96
<b>5</b>	<b>Perspectives</b>	<b>99</b>
	<b>Conclusions</b>	<b>111</b>
	<b>References</b>	<b>115</b>

# INTRODUCTION

---

One of the main challenges that has driven the different imaging techniques is the improvement of the spatial resolution. This is of course motivated by the wish of the human being to see what is hidden from our natural imaging system (an aperture, one lens and a detector, that is to say the eye). Consequently, the first solutions from the *XVIIth* century were naturally based on the improvement of this basic optical system. New components (lenses arranged in a smart way) were added, but the eyes were still used as a part of the detection. Such systems included among other, the telescope of Galileo Galilei, aiming at seeing what was as far as the stars, and the optical microscope of Zacharias Janssen to observe objects as small as a cell.

The invention of the optical microscope generated an immense impact on the development of biological research (the discovery of cells, the study of bacteria, etc). However, there was still the open question on how to further increase the resolution. The diffraction limit theory of Ernest Abbe in 1873 showed that the limit of the spatial resolution in an optical microscope is related to the point-like source diffraction. In this way, the optimal resolution is given by half of the source wavelength and is thus limited in the visible spectral range to sub-micrometer. The consequence is that improving the spatial resolution can be achieved by reducing the wavelength of the source of the illumination. Around 1904, the first ultraviolet (UV) microscope was constructed allowing an improvement of the resolution by a factor two. Pushing this idea to the extreme, in 1931 the first electron microscope was created replacing photons with electrons. This technique allows nowadays atomic like spatial resolutions, i.e. few angstroms.

After Röntgen's discovery of X-rays in 1895 [75], point-projection microscopy with a resolution of a few microns was developed [24]. But only around 1946 the scientific community started to be more interested in X-ray microscopy [47]. Working with very short wavelengths led researchers back to the first problem, i.e. the improvement of the optical systems. The biggest constraint of X-ray microscopy is the limitation in the spatial resolution which is related to the manufacturing quality of X-ray optics. The first works were focused on the development of new X-ray optics, like the crossed mirror system K-B (Kirkpatrick and Baez) designed at Stanford University in 1948 and currently used worldwide in different synchrotron or free electron laser (FEL) facilities as focusing systems.



It is well known that X-rays offer a path to the finest vision in space. Besides spatial resolution, X-rays can penetrate into objects opaque to visible light or electrons [63]. On one hand, X-ray crystallography demonstrated that X-ray diffraction is a powerful tool for characterizing objects at the atomic scale ( $\text{\AA}$ ), provided that they are repeated, for instance quasi periodically in a crystalline structure. However, this technique is restricted to samples that can be crystallized. On the other hand, X-ray microscopes are today of considerable use in both life and materials sciences, imaging typically  $\mu\text{m}$  size objects with tens of nm resolution. However, they meet the limits of lens-based instruments, in terms of resolution and field of view.

What imaging technique would allow access to high resolution in non crystalline structures, overcoming any focusing manufacturing limitation? Modern optics brought the answer with diffraction and Fourier optics, providing the theory needed to develop lensless imaging techniques and eliminate the constraint induced by the quality of the lenses.

In general, the diffraction depends on the object transmittance  $t(\vec{r})$  and the incoming field  $V_0(\vec{r})$  that irradiates the object [39]. Lets us remember that the transmittance function describes the amplitude and phase properties of the object. In general, it also depends on the incoming field. For example, an object can be transparent for certain wavelengths but opaque for others. In imaging, we are interested in the complex transmittance since it contains the object information. Consequently, in the following the term "object image" is referring to the transmittance function of the object.

As the diffraction pattern carries all the information of the transmittance function and the incoming beam, it is possible to use the diffraction to retrieve the transmittance function. It is the basic principle of lensless imaging techniques. If the properties of the incoming beam are known and the complex diffraction pattern can be measured, it is possible to retrieve the transmittance function by doing a back propagation of the diffraction. The main constraint applying this simple idea is that our sensors (cameras) detect only the intensity while the phase of the diffraction pattern is lost. This is the well known phase problem.

Furthermore, the propagation function depends on the spatial coherence of the field [38]. The simplest scenario is the case of a spatially coherent and monochromatic field. In this case, the far field diffraction of the incoming field through an object placed in the plane of coordinates  $\vec{r} = (x, y)$  (Fig. 0.1) is given by [39],

$$V(\vec{\rho}, z) = \frac{-ie^{ikz} e^{\frac{k}{2z}\vec{\rho}^2}}{\lambda z} \iint_{-\infty}^{\infty} V_0(x, y) t(x, y) e^{\frac{-2\pi i}{\lambda z}(\xi x + \eta y)} dx dy, \quad (1)$$

where  $V_0(x, y)$  is the incoming field of wavelength  $\lambda$  that irradiates an object of transmittance  $t(x, y)$ .  $z$  is the distance from the object plane to the detection plane of coordinates  $\vec{\rho} = (\xi, \eta)$ .

The double integral in Eq. 1 corresponds to a Fourier transform of the transmitted beam  $V(x, y) = V_0(x, y) t(x, y)$ , as a function of the normalized coordinates  $(\xi/\lambda z, \eta/\lambda z)$ , which

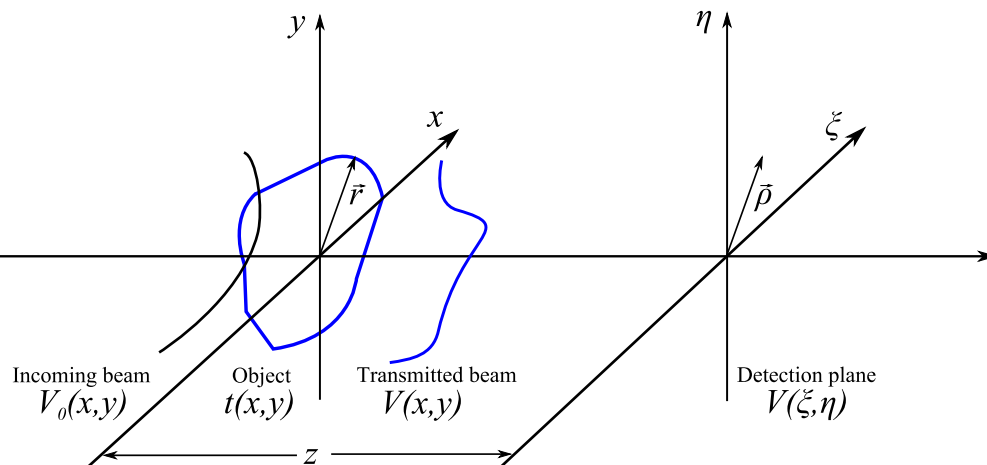


Figure 0.1: Diffraction of an incoming field  $V_0(\vec{r})$  through a transmittance function  $t(\vec{r})$ . The diffraction of the transmitted field  $V(x,y)$  is detected at the plane of coordinates  $\vec{\rho} = (\xi, \eta)$

spatially scale the Fourier transform with the wavelength  $\lambda$ .

$$V(\vec{\rho}, z) = \frac{-ie^{ikz} e^{\frac{k}{2z}\vec{\rho}^2}}{\lambda z} T(\vec{\rho}) \Big|_{\vec{\rho}/\lambda z}. \quad (2)$$

$T(\vec{\rho})$  is the Fourier transform of the transmitted field  $V(x,y)$ . It means that, if we are able to detect the phase and the amplitude of the diffraction pattern, the image of the object can be retrieved by taking the inverse Fourier transform of the complex diffraction pattern. However, as explained before, only the intensity of the diffraction pattern  $I(\vec{\rho}) = |V(\vec{\rho}, z)|^2$  is detected.

Two main solutions that have been successfully adopted to solve this problem are: Fourier transform holography (FTH) [23, 32, 41, 56, 85] based on the holographic method proposed by Gabor [30] in 1948, and coherent diffractive imaging (CDI) [11, 29, 61, 80] based on an iterative algorithm proposed by Gerchberg and Saxton [36] in 1972. Gabor [30] presented the idea of a lensless imaging technique to overcome the problem of aberrations induced at short wavelengths. This so-called holographic method was meant to improve the resolution of electron imaging limited by the spherical aberration of the electron lenses. The resulting "electron interference microscope" proposed by Gabor is what we know as "in line holography". In this configuration only a part of the incident beam is diffracted by the object, while the other part of the beam acts as the holographic reference. From the interferogram produced by the diffracted beam and the reference it is possible to encode the phase. Gabor's original idea was to illuminate the recorded hologram to generate the reconstruction [30]. However this idea was not applied and instead optical holography experienced a remarkable development after the discovery of the laser. Optical holograms are

usually detected on a photoresist which is a photo-sensitive material. The illuminated areas are removed chemically and then the interferogram that encodes the phase of the object diffraction is printed on the material. A later illumination with a source similar to the reference allows the object reconstruction. While it could seem impossible to have a photoresist to record an hologram generated with a X-ray source, or to find a reference beam for the post illumination of the hologram, the experimental application of this technique was successfully achieved with an X-ray source generated in a synchrotron by using a photoresist specially designed for this radiation [44]. This experimental constraint was overcome with digital holography. In this case, the interferogram is detected with a CCD camera and the back propagation leads to the numerical reconstruction of the object. This technique has been successfully applied with XUV sources [23, 32, 56].

Nevertheless, the use of a reference is an important experimental constraint. In the case of FTH, the size of the reference is closely related to the resolution that can be reached in the object reconstruction. Moreover, the preparation of the sample implies the location of a reference next to it which is not in general possible and thus limits the use of the technique. Therefore, different methods were proposed to solve the general problem: obtaining the object reconstruction (amplitude and phase) from the amplitude of the diffraction pattern without the use of a reference. One of the most important solution is the iterative algorithm introduced by Gerchberg and Saxton [36] in 1972. Their work was based on the iteration of the back and forward propagation between the detection and object planes. The constraints included in their algorithm are the measurement of the object intensity in the object plane and the intensity of the diffraction pattern (Fig. 0.2).

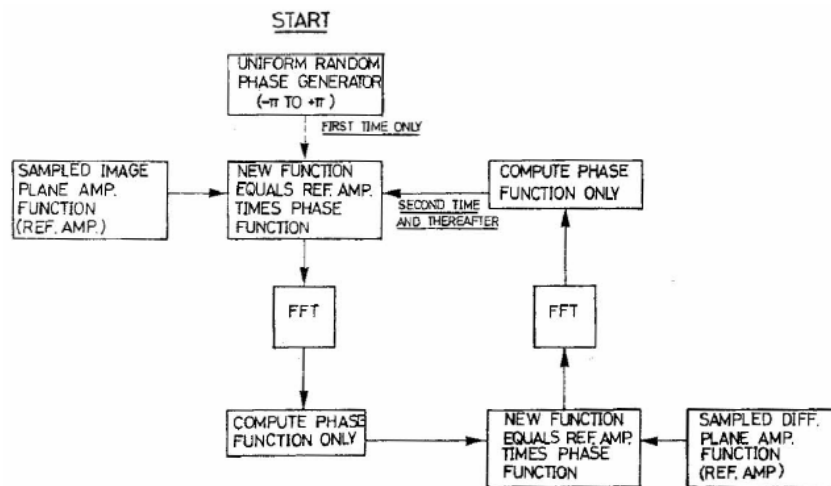


Figure 0.2: Schematic representation of phase retrieve algorithm proposed by Gerchberg and Saxton [36].

The idea to uniquely solve the diffracting object from the intensity of the X-ray diffraction on a crystal was proposed by Sayre [79] in 1952. Twenty years after, Gerchberg and

Saxton presented the X-ray diffraction from crystals as one of the possible applications for their iterative imaging algorithm [36]. But it was only in 1980 that Sayre suggested the possibility of doing imaging using a single isolated object, and not a periodic crystal, to produce a continuous X-ray diffraction pattern not restricted only to Bragg peaks.

Independently of Sayre's work, in 1978 Fienup [29] proposed an iterative algorithm based on the solution of Gerchberg and Saxton [36]. His iterative algorithm, called "error-reduction approach", imposed a new set of object constraints (Fig. 0.3). One of the main differences to the original work is the elimination of the constraint imposed in the object plane, thus making possible the object reconstruction using only the measurement of the diffraction pattern intensity. To achieve this, Fienup introduced the concept of "support function". Instead of knowing the object amplitude he forced the solution in the object plane to be zero outside of the support. Therefore, the support is a zone that contains the object. It can be calculated from the autocorrelation of the object, i.e. the Fourier transform of the measured diffraction pattern. Moreover, Fienup's algorithm was proposed as a solution to improve the resolution in astronomical imaging with diffraction-limited measurements of the modulus of the object Fourier transform. Due to the nature of the astronomical application, the object was described as a real, non-negative function. In the case of complex valued objects the reconstruction is then more difficult. In 1987, Fienup [28] proposed a modification of his iterative algorithm eliminating the non-negative constraint and using only a support constraint. Over the years, Fienup developed different variations of his algorithm [27]. The faster convergence is achieved with the hybrid input output (HIO) algorithm.

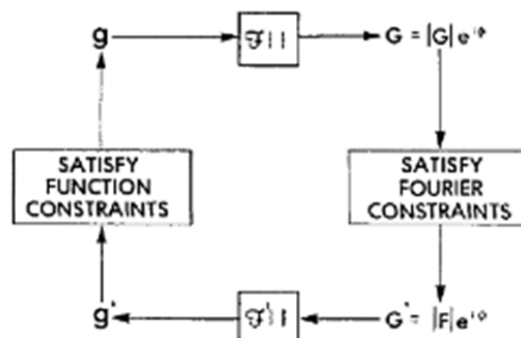


Figure 0.3: Block diagram of error reduction algorithm proposed by Fienup [29].

The uniqueness of the solution is one of the main issue in the phase problem. Indeed, multiple complex objects may generate the same amplitude in the diffraction pattern. Therefore, multiple solutions could fit the experimental measurements. In 1982 Bates [8] showed theoretically that the Fourier phase problem has an unique solution if sufficient oversampling is made. Based on the oversampling proposed by Bates [8], Miao et al. [60] proposed an oversampling ratio that relaxes the sampling conditions determined by Bates.

They introduced the oversampling ratio in the iterative algorithms to improve the image reconstruction. Using these iterative algorithms, Miao et al. [61] demonstrated for the first time CDI reconstruction of a non crystalline sample by using an X-ray diffraction pattern generated with synchrotron radiation. After this demonstration, different modifications of the CDI algorithms have been proposed. The support constraint from Fienup's work [27] has been improved by using the Shrinkwrap algorithm developed by Marchesini et al. [55]. In this case, the support is not a fixed input of the CDI iterative algorithm but instead is updated along the reconstruction process. The first approximation of the support is given by the autocorrelation and each "n" iterations it is improved using a threshold on the current best guess of the object. This solution has been successfully implemented experimentally with XUV sources [6, 7, 12, 52].

A remarkable development of the lensless imaging techniques using coherent X-ray sources has pushed down the spatial resolution to the nanometer scale [11, 23, 32, 41, 56, 61]. If the diffraction limit can be reached, the use of coherent X-ray sources has the potential of generating atomic vision.

However, though atoms can be imaged in space, conventional synchrotron sources do not allow accessing the fastest processes in matter at the atomic scale, which is the new frontier towards femtosecond to attosecond time resolution.

Contemporary to the diffraction theory of Abbe, the British photographer Eadweard Muybridge presented the first solution to follow motions faster than the temporal resolution of the human eye ( $\sim 0.1$  second to perceive images individually). To answer the famous question: "whether all four feet of a horse were off the ground at the same time while trotting" (Fig. 0.4) recorded a sequence of pictures by using a fast shutter with millisecond resolution. The idea of using a flash of light instead of using a fast shutter was proposed in 1832 by Joseph Plateaus with the invention of the stroboscope. This technique is applied to periodic movements. When the frequency of the flash light is equal to the cyclic speed of the object (or a unit fraction), the object seems stationary or moving slowly. A millisecond temporal resolution was achieved with the first electric stroboscope created by Etienne Oehmichen in 1917. Thanks to the short pulse duration and short wavelengths of X-ray sources, this technique has been recently used with phase-controlled stroboscopic X-ray pulses of a synchrotron [74] to study biomolecules vibrations with a temporal resolution on the picosecond scale and a sub-nm spatial resolution.

To follow faster movements we need faster shutters and the fastest shutter is light itself. The use of short temporal pulses of lasers as the fast shutter of a photographic camera pushed down the achievable temporal resolution to the femtosecond scale ( $10^{-15}$ s). During the last two decades, femtosecond laser pulses have been successfully used in femtochemistry to study atomic and molecular dynamics involved in chemical reactions [93].

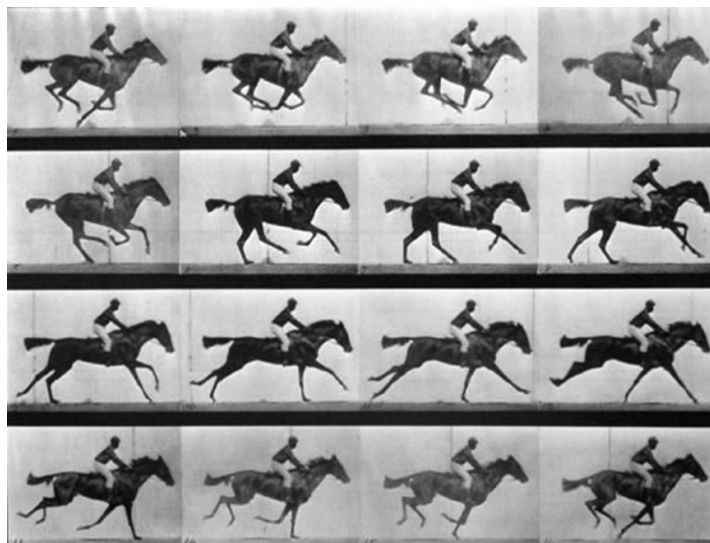


Figure 0.4: The horse in motion by Eadweard Muybridge in 1878.

The pulse duration of X-ray sources has been pushed down to the femtosecond scale with the development of Free electron laser (FEL) [42]. FELs generate tunable, coherent and high power radiation within a large range of wavelengths from millimeter to ultraviolet or even X-ray (XFEL). The very first single shot imaging demonstrated in 2006 [12] has opened the route to femtosecond time resolved nanoscale studies [6, 13]. In-situ single shot images of biological samples with nanometer resolution have been realized for the first time using the CDI technique at the Stanford free electron laser (LCLS) [83] (Fig. 0.5). Those measurements are of strong interest as a large gap exists in the knowledge of their structure in the range from about 30 nm to 500 nm. In fact, these length scales remain uncharted territory for many other biological systems.

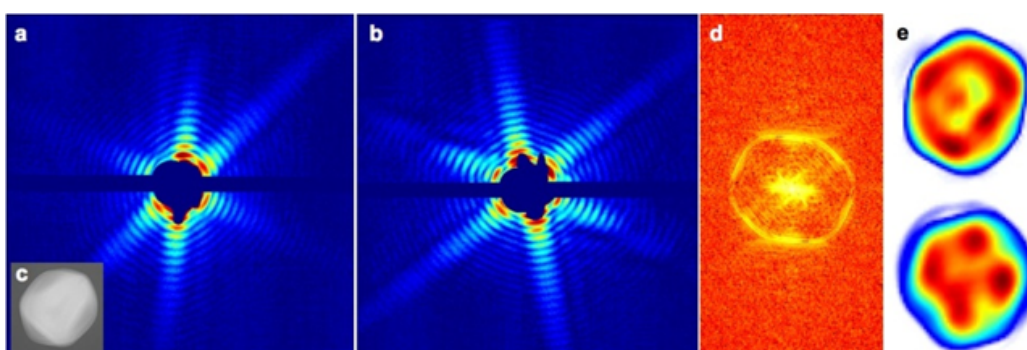


Figure 0.5: First results from LCLS where single mimivirus particles were injected into the FEL beam. Recorded diffraction patterns (left) and image reconstruction of the virus (right) [83].

Contrary to the large-scale facilities needed for FELs (order of kilometers in length), XUV and soft X-ray coherent radiation may be generated in smaller facilities (much more accessible compared to the expensive FEL beam-time). High harmonic generation (HHG) is a non-linear process with remarkable properties. HHG produces coherent XUV and soft X-ray radiation with femtosecond and attosecond ( $10^{-18}$ s) pulse duration. It has been discovered simultaneously at Saclay by Ferray et al. [26] and Chicago by Mcpherson et al. [57]. HH radiation is generated by a very strong non-linearity induced in an atomic gas jet submitted to an intense infrared pump laser. The generation of ultrafast HH radiation can be described in three steps (Corkum PB. [18], M et al. [51], Schafer et al. [82]) confined in a gas jet of some  $\mu\text{m}$  that can be extended to some cm to achieve a stronger signal.

Compared to FEL sources, HHG produces a lower flux of soft X-ray coherent photons but without jitter problems thanks to the natural synchronization of the HH emission with the laser that drives the generation. Practically, FELs have a higher flux of hard X-ray coherent photons with few femtosecond pulse duration and jitter of the order of tens of fs. The difference in flux of photons restricted lensless imaging techniques to large-scale facilities during some years after the first single shot imaging experimental demonstration. In 2007, Richard Sandberg and colleagues have succeeded in demonstrating CDI using a kHz table-top laser driven HHG source with a spatial resolution of 214 nm [76]. The brightness of the harmonic beam was still limited, and the exposure time (at the scale of an hour) was far from reaching single shot ultrafast nanoscale imaging, required in ultrafast dynamical studies. In 2009, our research group at CEA (Commissariat à l'Énergie Atomique et aux Énergies Alternatives) has demonstrated the first single-shot CDI using a table-top femtosecond soft X-ray laser harmonic source [73]. An isolated test nano-object was reconstructed with 119 nm spatial resolution in a single 20 fs - long shot. The spatial resolution in single shot acquisition was pushed to 70 nm after optimizing the HHG beamline [34]. Reaching the diffraction limit imposes high quality beam conditioning and properties. Indeed, in CDI the image reconstruction quality and resolution is limited by the signal to noise ratio (SNR) of the diffraction pattern and the beam properties, in particular wavefront and coherence. In fact, it is a direct consequence of the beam propagation. Any variation in the wavefront of the incident beam has to be taken into account in the incoming field  $V_0(x,y)$  that is diffracted by the object (Eq. 1). Furthermore, in case of a partially coherent beam, the far field diffraction is not longer described by a Fourier transform of the transmitted beam (Eq. 1) [38]. Thus, additionally to the knowledge of the phase and intensity of the incoming field, a characterization of the spatial coherence is also needed.

At the beginning of the 21<sup>st</sup> century, the first experimental measurement of a train of 250 attosecond pulses was demonstrated [43, 69], thus pushing down the temporal resolution of ultrafast time-resolved measurements, from femtosecond to attosecond time scales which are mostly related to electron motion. This train of attosecond pulses was a superposition of five consecutive harmonics generated by HHG process in an atomic gas jet submitted to

an intense infrared pump laser. Pioneering experiments demonstrated the measurements of electron dynamics with attosecond resolution, such as the measurement of the lifetime of M-shell vacancies of krypton [22], the intra-atomic transient electron dynamics [45] and the observation of the motion of a D2+ vibrational wave packet with a precision of about 200 attoseconds [65]. In May 2010, a German group has demonstrated the new world record for the shortest controllable time for a light pulse – 12 attoseconds [19], which is half of the atomic unit of time – 24 attoseconds. However, experimental measurement combining atomic distance scale (sub-nanometer resolution) and attosecond time resolution is not yet demonstrated. This big challenge will require the invention of new imaging techniques with broadband sources to achieve sub-atomic unit resolution simultaneously in space and time. 3D motion of electrons would then be accessible. This foreseen revolution will open a new era of physics and ultimately influence chemistry, biology and future technologies.

### **Aim and Outline of this Thesis**

The principal aim of this work, started in 2011, was to study XUV imaging in single shot, towards the development of new imaging techniques and new applications using HH and FEL sources. This thesis is divided in two parts, the first is focused on the characterization of the sources and the second on the development of new imaging techniques. The results presented are the product of different experimental campaigns performed during this thesis and using HH sources at CEA-Saclay, LOA-ENSTA, and FEL facilities at LCLS-Stanford and FERMI@ELETTRA- Trieste.

Chapter 1 presents a new technique for single shot characterization of spatial coherence. The characterization of the coherence has several uses. On one hand, the diffraction of the source depends on the coherence [38], making knowledge of the coherence important for applications based on interferometric techniques. Consequently, lensless imaging techniques are related to the degree of coherence [35, 87, 90, 91]. The knowledge of the spatial coherence can be used as an input in lensless image reconstruction to improve the image quality. Furthermore, the growing interest of the XUV community in developing XUV optics opens the possibility of future applications in imaging with XUV optical systems. In this case, the resolution is also related to the spatial coherence of the source. On the other hand, the coherence of the source allows studying the physics of the generation [20, 88]. The understanding of the process and the relation of the diffraction with the coherence opens the possibility of XUV beam shaping.

In this chapter we present a single shot measurement of the coherence that doesn't require the knowledge of the shot to shot intensity distribution. The chapter starts presenting the theoretical background of spatial coherence. The second part details the theory of the single shot technique based on a two-dimensional array of apertures that samples the incoming field. Experimental results of spatial coherence measurements on a XUV beam



(harmonic 25 from an IR laser,  $\lambda = 32$  nm) performed on our beam line are presented. A comparison between the experimental measurements and simulations validates the single shot technique.

A theoretical description, developed to expand the method of spatial coherence characterization in the Fresnel regime, is presented. This opens the possibility of spatial coherence characterization in real time at XFEL facilities.

Finally, the theoretical description of Fourier transform holography with a partially coherent source is presented. We deduce an analytical relation between the object reconstruction and the spatial coherence of the source. Using the spatial coherence characterization presented in this chapter, it is then possible to compensate the modulation induced by the spatial coherence in the object reconstruction.

In chapter 2 different applications of the XUV wavefront characterization are presented. The expertise achieved in the ATTO-Physics group at CEA-Saclay on soft XUV wavefront characterization using a commercial UV Hartmann sensor (paper III) was applied to FEL sources. Two applications have been developed during the work of this thesis. The first one consists in the optimization of the KB focusing system at the LCLS AMO station (SLAC, Stanford) and the second to the imaging beamline DiProy (FERMI@ELETTRA-Trieste) characterization, via wavefront sensing (see paper II).

As an application, wavefront sensing was used to follow LCLS produced plasma dynamics during the early (sub-ps) stages of X-ray heating. The target was probed with short ( $< 40$  fs) pulses of XUV (15 – 60 nm) radiation created by HHG, which penetrated through the plasma target. As this radiation propagates through the sample, it is either absorbed or scattered in the forward direction, undergoing a change in phase. Wavefront sensing was then used as a method to detect the phase changes induced by the variation of the plasma refractive index. The experiment, conducted in July 2013 at the MEC (Matter in extreme conditions) station at LCLS, is the first FEL pump - HH probe experiment performed at the LCLS.

The second part of the thesis is dedicated to single shot lensless imaging techniques and is presented in chapters 3 and 4.

In chapter 3 we present an extension of our 2D ultrafast nanoscale imaging techniques to obtain 3D images. It is based on the stereo viewing of our sample. Ultrafast *single shot 3D stereo imaging* would allow lowering the impact of X-ray exposure in image reconstruction together with a 3D perception of the object. Single shot techniques are the solution to follow dynamics in the case where the object will irreversibly be transformed or destroyed after being pumped. The stereo imaging presented in this chapter is based on human vision. Our right and left eyes take two 2D images at different observation angles of the object and the brain combines these images to give the 3D perception. Each image is associated to the other with a spacing (given by the parallax) and a different color or polarization (this encoding is called an anaglyph). The use of filters in front of the eyes to observe the anaglyph allows

to the brain to separate each lateral projection related to each eye's image. It is not a real 3D imaging but already provides much more interesting information about the object than a 2D image. In this chapter, we present different experimental solutions to the generation of two soft X-ray sources and the generation of an anaglyph. The experimental results were obtained in different campaigns at the HH beamline of CEA-Saclay.

Chapter 4 presents experimental work on imaging using a broadband source with a discrete spectrum. The experiments have been conducted using a holographic imaging technique and a comb of three harmonics (H23, H25, H27) in single shot data acquisition. We present experimental results with the simultaneous reconstruction of spectrally resolved images at each harmonic wavelength. The distance object-reference determines the separation between the multiple wavelengths reconstructions. The option of having a superposition of the spectral reconstruction was also studied. This opens the possibility of performing imaging with broadband spectrum sources that support attosecond pulses. A blurring in the reconstruction is induced by the overlap of the spectral reconstructions. The minimum blurring effect is determined by the source bandwidth and the spatial dimensions of the object. These two parameters determine the possible conditions to perform attosecond imaging

Finally, we present the general conclusions from the work done during the thesis, together with the perspectives drawn from this work.



---

# SINGLE SHOT CHARACTERIZATION OF XUV SPATIAL COHERENCE

---

XUV sources generated by HHG or FEL provide pulses with a partial spatial coherence [50, 88] and a temporal coherence shorter than the pulse duration [9]. In this case, there are some restrictions for the characterization of the spatial coherence due to the short wavelengths and short pulse duration. Most of the optical devices used to characterize the coherence are not available for XUV sources. Moreover, the short pulse duration requires methods of characterization in single shot to study the dynamics of the generation process with a resolution equivalent to the pulse duration.

The characterization of the coherence has different uses. On one side, the diffraction of light depends on its coherence [38], making the knowledge of the coherence important for applications based on interferometric techniques. That is the case in lensless imaging, where the quality of the image reconstruction is related to the degree of coherence of the illuminating light source [35, 87, 90, 91]. On the other hand, the coherence of the light source allows studying the physics of the generation [20, 88]. The understanding of the process and the relation of the diffraction with the coherence opens the possibility of XUV beam shaping. Additionally, the knowledge of the spatial coherence can be used as an input in lensless image reconstruction to achieve better image quality.

Experimentally, HHG and FEL sources exhibit shot to shot variations in the yield and the coherence. An open question is: how does the spatial coherence fluctuate from shot to shot? Single shot data would help in assigning this either to the generation process or to instabilities (pointing fluctuations for example). To answer this question, it is necessary to develop methods of characterization in single shot. Up to now, all the methods require the characterization of the intensity distribution of the incoming beam, but measuring both coherence and intensity in the same shot is difficult in the XUV range, because of the lack of beamsplitters. In this chapter we present a new method of characterization in single shot that needs only one diffraction measurement. This method is based on a variation of the

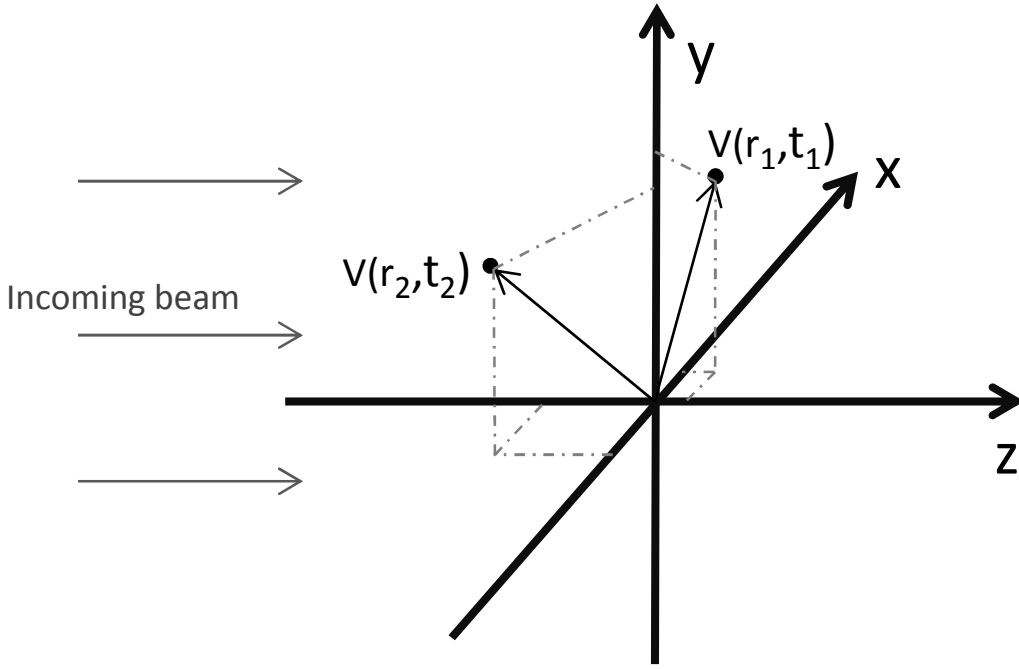


Figure 1.1: Two points separated in space and time.

interference of multiple apertures of Mejía and González [58].

The coherence is a statistical measurement of the correlation that exists between the field oscillations at two different points and times  $V(\vec{r}_1, t_1)$  and  $V(\vec{r}_2, t_2)$ . For a field that is statistically stationary and ergodic (the fact that it is stationary and ergodic allows that the ensemble averages are independent of the origin of time and then the ensemble average in Eq1.1 can be given by a temporal average) the second order coherence is given by the cross-correlation function  $\Gamma(\vec{r}_1, \vec{r}_2; t_1, t_2)$  [54],

$$\Gamma(\vec{r}_1, \vec{r}_2; t_1, t_2) = \langle V^*(\vec{r}_1, t_1) V(\vec{r}_2, t_2) \rangle_T \quad (1.1)$$

where  $\langle \rangle_T$  denotes the temporal average, and  $\vec{r} = (x, y)$  is the spatial coordinate at the plane where the measurement of the coherence is made (Fig 1.1). The spatial or the temporal coherence can be isolated in Eq. 1.1 by making the temporal delay  $\tau = t_1 - t_2$  or the spatial separation  $\vec{d}_{12} = \vec{r}_1 - \vec{r}_2$  equal to zero, respectively. It corresponds either to the experimental case of an interferometer with amplitude splitting (Michelson interferometer) or to the one with wavefront splitting (Young interferometer).

In the particular case of  $\tau = 0$ , Eq. 1.1 denotes the mutual intensity  $J(\vec{r}_1, \vec{r}_2) = \Gamma(\vec{r}_1, \vec{r}_2; \tau = 0)$ . The complex degree of spatial coherence  $\mu_{12}$  (for the following part of the text it will be called the spatial coherence) is defined in terms of the mutual intensity as,

$$\mu(\vec{r}_1, \vec{r}_2) = \frac{J(\vec{r}_1, \vec{r}_2)}{\sqrt{J(\vec{r}_1, \vec{r}_1)} \sqrt{J(\vec{r}_2, \vec{r}_2)}} \quad (1.2)$$

with  $\sqrt{J(\vec{r}_i, \vec{r}_i)} = I(\vec{r}_i)$  the intensity in each one of the points  $i = (1, 2)$ . The spatial coherence  $\mu_{12}$  is limited by [38]

$$0 \leq \mu(\vec{r}_1, \vec{r}_2) \leq 1 \quad (1.3)$$

the two limits represent the incoherent case  $\mu_{12} = 0$  and the fully coherent one  $\mu_{12} = 1$ . The case of a partial spatial coherence corresponds to  $0 < \mu_{12} < 1$ .

There are different methods to measure the spatial coherence. Historically, the first method is the interference of two sources presented by Young and studied with more details by Zernike and Wolf. A direct consequence of the definition of the coherence in Eq. 1.1 is that the spatial coherence is a function of the vectorial position of two points  $\vec{r}_1$  and  $\vec{r}_2$  and more exactly of the vectorial separation between these points  $\vec{d}_{12} = \vec{r}_1 - \vec{r}_2$ . It implies that the characterization of the spatial coherence requires the measurement of the coherence at different separations  $\vec{d}_{12} = \vec{r}_1 - \vec{r}_2$ . The methods based on the two source interference [64, 78] are time consuming and are not suitable for single pulse characterizations because the parameter  $\vec{d}_{12}$  must be changed for each interferogram. An alternative method using the interference of multiple apertures allows measuring the spatial coherence at different distances with one interferogram [37, 58]. Le Déroff et al. [50] proposed a technique for the characterization of the spatial coherence of XUV sources where, with one interferogram, it is possible to measure the spatial coherence at different separation vectors  $\vec{d}_{12} = \vec{r}_1 - \vec{r}_2$  associated to a given magnitude of separation  $|\vec{d}_{12}|$ . And then, a characterization as a function of the magnitude of separation  $|\vec{d}_{12}|$  also implies multiple interferograms. There are other methods based on the Wigner function representation of the field. In this case, it is possible to determine the coherence through an edge diffraction [16], analyzing the propagation of the partial coherent field as described by the Wigner function [2]. The comparison of the diffraction with and without the edge is needed which does not allow to use this method in single pulse configuration. Phase space tomography based on the Wigner function [67] can be used to measure the spatial coherence. This technique has some limitations [17]. It is limited to paraxial fields and the intensity must be measured in a large region that includes the far field. For a characterization in single pulse configuration, the multiple intensity measurements make necessary the development of an experimental system to register the diffraction at different planes in single pulse.

---

## 1.1 Characterization of single pulse spatial coherence of HH and FEL sources

In this section a new method to characterize the spatial coherence is presented. This method does not need any measurement of the intensity distribution of the field, which makes it

a powerful tool for the spatial coherence characterization of single pulses. The method is based on a variation of the spatial coherence characterization with multiple apertures [37, 58] that allows measuring the spatial coherence at different vectors of separation  $\vec{d}_{nm}$  with only one far field interferogram. The characterization of the spatial coherence is made as a function of the magnitude of the separation  $|\vec{d}_{nm}|$  at some separations  $\vec{d}_{nm}$  fixed by the distribution of apertures. There is a complementary method to characterize the spatial coherence of XUV sources where using only one interferogram it is possible to measure the spatial coherence as a function of the vectorial separation  $\vec{d}_{nm}$  for a fixed magnitude of separation  $|\vec{d}_{nm}|$  [50]. In both cases, the intensity is needed to retrieve the spatial coherence. In the method proposed by Le Déroff et al. [50], the intensity was found with the diffraction of the incident field through the edge of the mirrors that form the experimental setup. This assumption can be done for a particular case: when the diffraction of the partial coherent field is similar to the coherent approximation.

The new method presented in this section uses a multiple aperture interferogram [37, 58] generated by a NRA (non-redundant array) of apertures. The two dimensional NRA of apertures has been designed to generate a consistent set of solvable equations that allows calculating the spatial coherence and the intensity at the position of each aperture. It can be applied in the case that the magnitude of the spatial coherence is shift invariant. It means that the spatial coherence is a function of only the magnitude of the separation  $|\vec{d}_{nm}|$ .

### 1.1.1 Description of the method

It has been shown that the use of a NRA of  $N$  apertures allows measuring the coherence of all the pairs of apertures  $\{n,m\}$  ( $n,m = 1,2,\dots,N$ ) contained in the NRA, if the intensity of the light source is known. The measurement of the coherence is made using the Fourier transform of the interferogram generated by the diffraction of the field through the array. The Fourier transform of the interferogram is a distribution of peaks centered at the different vectors of separation of the pairs of apertures  $\vec{d}_{nm} = \vec{r}_n - \vec{r}_m$  [37, 58].

$$\tilde{I}(\vec{r},z) = \Lambda(\vec{r}) \otimes \left[ \sum_{n=1}^N I_n \delta(\vec{r}) + \sum_{n=m+1}^N \sum_{m=1}^{N-1} \sqrt{I_n I_m} \times \left\{ \mu_{mn} \delta(\vec{r} - \vec{d}_{nm}) + \mu_{mn}^* \delta(\vec{r} + \vec{d}_{nm}) \right\} \right]. \quad (1.4)$$

Where  $\Lambda(\vec{r})$  is the autocorrelation of the function that describes the geometry of each aperture  $h(\vec{r})$ . For circular apertures of radius  $a$ ,  $h(\vec{r}) = \text{circ}(\vec{r}/a)$ . In the case of a NRA the amplitude at each peak is proportional to the magnitude of the coherence  $\mu_{mn}$  and the intensity ( $I_n, I_m$ ) of the pair of apertures at a separation vector  $\vec{d}_{nm}$ . The magnitude of the coherence  $|\mu_{nm}|$  is given by

$$|\mu_{nm}| = \frac{|C_{nm}|}{\sqrt{I_i} \sqrt{I_j}} \frac{S_0}{|C_0|}, \quad (1.5)$$

where  $|C_{nm}|$  is the peak magnitude of the Fourier transform of the diffraction pattern (NRA autocorrelation) centered at  $\vec{d}_{nm} = \vec{r}_n - \vec{r}_m$ .  $S_0 = \sum I_n$  is the total intensity of the field thought the NRA and  $|C_0|$  is the magnitude of the central peak of the spectrum.

To eliminate the constrain imposed by a parallel characterization of the beam intensity on the NRA, we can generate a NRA of a minimum number of  $N = 3$  apertures in a configuration where  $|\vec{d}_{nm}|$  is constant for all the pairs  $\{n,m\}$  (Fig. 1.2).

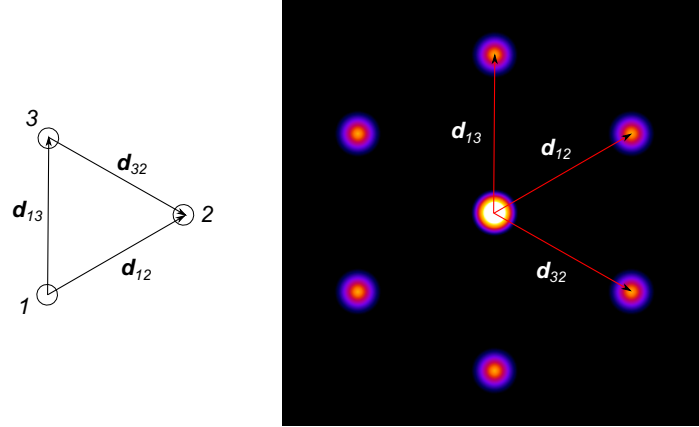


Figure 1.2: Right, NRA with equal  $|d_{nm}|$ . Left, Fourier transform of the diffraction pattern generated by the NRA (NRA autocorrelation).

From Eq. 1.5 we have a set of 3 equations.

$$\begin{aligned} |\mu_{12}| &= \frac{C_{12}}{\sqrt{I_1 I_2}} B_0 \\ |\mu_{13}| &= \frac{C_{13}}{\sqrt{I_1 I_3}} B_0 \\ |\mu_{23}| &= \frac{C_{23}}{\sqrt{I_2 I_3}} B_0 \end{aligned} \quad (1.6)$$

where  $B_0 = S_0/|C_0|$ . This set of 3 equations with 6 unknowns can be solved in the case where the magnitude of the coherence is shift invariant. The solution can be found by referring to the intensity of one aperture that we will call "the reference aperture". The solution to the set in Eqs.1.6 is then given by

$$\begin{aligned} |\mu_{nm}| I_1 &= \frac{C_{12} C_{13}}{C_{23}} B_0 \\ I_2 &= I_1 \left( \frac{C_{23}}{C_{13}} \right)^2 \\ I_3 &= I_1 \left( \frac{C_{23}}{C_{12}} \right)^2 \end{aligned} \quad (1.7)$$

Even when the solution is given in terms of the intensity of the reference aperture, the measurement of the intensity is not needed. The multiplicative factors  $I_1$  and  $B_0$  can be



normalized after interpolation of the spatial coherence to  $\vec{d}_{nm} = 0$  where we can apply the condition  $\mu_{nn} = 1$ .

Using this as a basis we can build a NRA with  $N > 3$  apertures generated by a superposition of different sets of 3 apertures. In the case that all the sets of 3 apertures share one reference aperture (Fig. 1.3), the solution for the NRA with  $N > 3$  can be given in terms of the intensity of only one reference aperture. After normalization, the degree of coherence is found directly for a set of  $N(N - 1)/2$  pairs of apertures from one interferogram and without the measurement of the intensity.

To further illustrate the method we have designed a NRA with 7 apertures shown in Fig. 1.3 (a). The autocorrelation of the NRA (Fig. 1.3 (b)) presents the different separation vectors  $\vec{d}_{nm}$  of the 21 pairs of apertures that make the array. The simulation of the Fourier transform of the interferogram (Eq. 1.4) has been made using a Gaussian distribution of intensity ( $w_I = 5.2 \mu\text{m}$ ) and a Gaussian degree of coherence ( $w_c = 4 \mu\text{m}$ ). With the simulated values of  $C_{nm}$  and Eqs. 1.7 the degree of coherence is calculated assuming an unknown intensity.

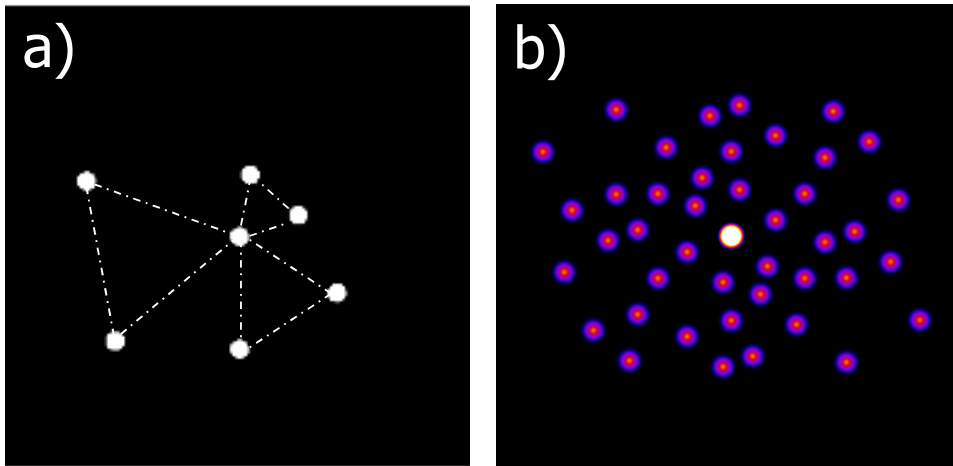


Figure 1.3: Left, NRA using 3 sets of NRA with equal distance, marked with the dotted line. Right, the autocorrelation of the NRA.

The result of the simulation is presented in Fig. 1.4. In this case, the Gaussian distribution of the intensity (Fig. 1.4 (a)) is centered at the NRA reference aperture. The position of each aperture is marked with a black circle. Fig. 1.4 (b) shows to the degree of coherence of reference (bold line) and to the calculated one (black squares). The result is shown in 1D because we have assumed a shift invariant coherence. The result demonstrates clearly that

it is possible to retrieve the degree of coherence without the measurement of the intensity through the diffraction of a single pulse.

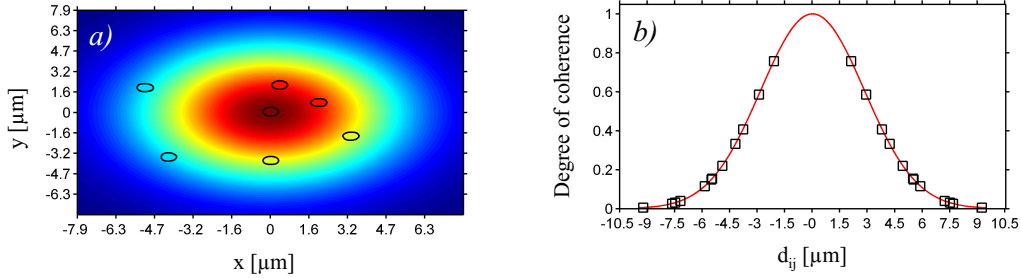


Figure 1.4: a) Gaussian beam profile centered at the NRA reference aperture. The aperture positions are marked with the black circles. b) Simulation of  $|\mu_{nm}|$  (bold line) and normalized reconstruction (squares) assuming the intensity is unknown.

It has been found before that the pointing stability in a XUV source is critical for the measurement of the coherence. In the case of single pulse characterization using a Young interferometer with the supposition of equal intensity at each aperture, Vartanyants et al. [88] showed that the experimental error induced is highly dependent of the beam pointing. This beam pointing issue is solved with the new method presented in this section. Fig. 1.5 shows that the result is independent of the beam position. In this case, a shift in the position of the Gaussian distribution of the intensity is considered. The beam is centered at  $(-1.6, -1.1)\mu\text{m}$  with respect to the NRA reference aperture (Fig. 1.5 (a)). The result of the characterization of the coherence (Fig. 1.5 (b)) is equal to the case of the beam centered with respect to the array (Fig. 1.4). This result is directly related to the fact that the method presented does not use any restriction on the intensity distribution.

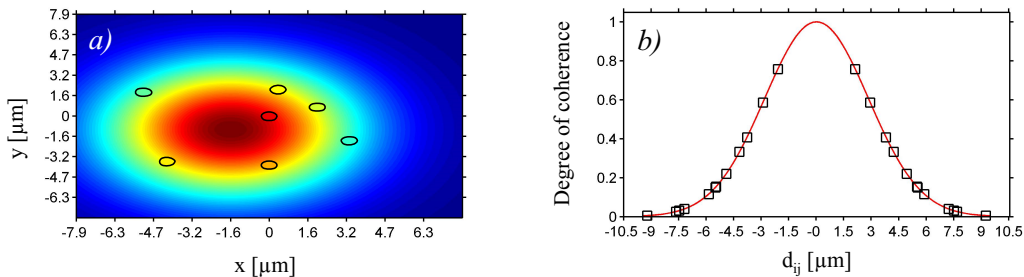


Figure 1.5: a) Gaussian beam profile centered at  $(-1.6, -1.1)\mu\text{m}$  with respect to the NRA reference aperture. The aperture positions are marked with the black circles. b) Simulation of  $|\mu_{nm}|$  (bold line) and normalized reconstruction (squares) assuming that the intensity is unknown.

### 1.1.2 Accumulation

Variations in the pointing stability of the XUV sources can introduce errors in retrieving the coherence. One of the most common errors presented in the precedent section corresponds to the assumption of equal intensity in the Young two pinholes scheme [88]. In this case, even single pulse measurements present a large error because the pointing stability makes it impossible to preserve the original supposition about the intensity. An additional error is generated in the case of an accumulation of multiple pulses. Indeed, as the temporal coherence of the XUV sources is comparable to the pulse duration, the accumulation will generate an incoherent sum of the pulses. The mutual intensity in this case can not be described by the total intensity at each aperture. Let us look at the easiest cases, Young interferometer with a single pulse and the incoherent accumulation of two pulses (Fig. 1.6). In the case of single shot, it is known that the visibility of the Young interference pattern is a function of the spatial coherence and the intensity of the apertures [38]. The visibility is equal to the spatial coherence only in the particular case where the intensity is the same in both apertures. The second line of Fig. 1.6 presents the incoherent accumulation of 2 pulses. The third line presents the Young interference produced when we suppose that the intensity at each aperture is equal to the total intensity after the accumulation of the 2 pulses, i.e.  $I_{1T} = (I_1^1 + I_1^2)$  and  $I_{2T} = (I_2^1 + I_2^2)$ . If the intensity  $I_1 = I_2$  in each one of the pulses, then the visibility is equal to the spatial coherence and the analysis with the total intensity is valid. However, if there is a variation in the intensity of the two apertures for one of the pulses, the visibility will be different from the spatial coherence. Moreover, the assumption of the total intensity would lead to a different value of visibility, inducing errors in the calculation of the spatial coherence. As a consequence, the pointing stability generates a larger error if the assumption of the total intensity is made.

Fig. 1.7 presents the comparison of the two sources interferogram technique with a pointing instability for the two configurations: single pulse and accumulation. To avoid the measurement of the intensity, the approximation of equal intensity on the two pinholes has been used. The simulation have been performed using an elliptic profile of intensity  $I = I_0 e^{-2(x^2/w_x^2 + y^2/w_y^2)}$  with horizontal and vertical sizes of  $w_x = 5 \mu m$  and  $w_y = 7.07 \mu m$  and a Gaussian coherence  $\mu_{nm} = e^{-2(d_{nm}^2/w_c^2)}$  with  $w_c = 14.1 \mu m$ . The beam pointing is simulated using a random function with respect to the center of the array and the maximum shift is equal to the beam size ( $5 \mu m$ ). A total of 200 positions were considered. The results presented in Fig. 1.7 are normalized to the maximum value i.e. the result at  $|\vec{d}_{ij}| = 1.3 \mu m$ . Clearly we can see that the supposition of equal intensity (visibility = spatial coherence) generates a large dispersion in the single pulse case (blue line generated by the blue crosses that represent the result for each pulses). The maximum error is 47% with respect to the spatial coherence of reference. In the case of the accumulation of multiple shots (black squares), the maximum error is reduced to 21% but is still very large.

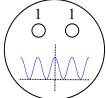
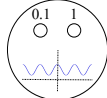
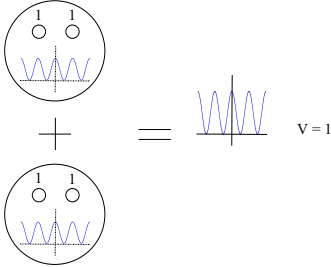
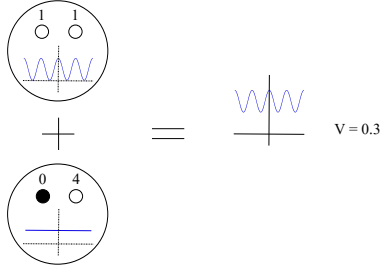
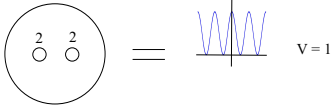
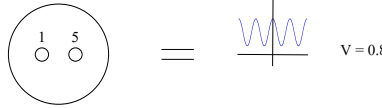
	Equal Intensity	Intensity variation
Single shot $V = \mu_{12} \frac{\sqrt{(I_1 I_2)}}{(I_1 + I_2)}$	 $V = 1$ $\mu = V$	 $V = 0.6$ $\mu \neq V$
Accumulation : Experiment $V = 2\mu_{12} \frac{\sqrt{I_1^1 I_2^1} + \sqrt{I_1^2 I_2^2}}{(I_{1T} + I_{2T})}$ $I_{1T} = I_1^1 + I_1^2$ $I_{2T} = I_2^1 + I_2^2$	 $V = 1$	 $V = 0.3$
Accumulation : Total intensity analysis $V = 2\mu_{12} \frac{\sqrt{I_{1T} I_{2T}}}{(I_{1T} + I_{2T})}$	 $V = 1$	 $V = 0.8$

Figure 1.6: Young interference in the case of equal intensity at the apertures ( $I_1 = I_2$ ) and with intensity variations ( $I_1 \neq I_2$ ). The first line presents the result with a single pulse. The second line shows the incoherent superposition of two pulses. The third line presents the result when the total intensity analysis is made  $I_{1T} = (I_1^1 + I_1^2)$  and  $I_{2T} = (I_2^1 + I_2^2)$ .

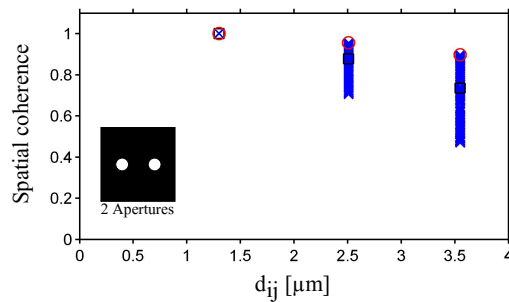


Figure 1.7: Double pinhole case. Single pulse calculation of the spatial coherence for 200 pulses with pointing instability (blue crosses). The Young method with the assumption of equal intensity has been used. The multiple crosses generate a vertical blue line. The black squares present the simulation of the spatial coherence calculation after the accumulation of the 200 pulses interferences. The beam spatial coherence is marked with the red circles. The results of the spatial coherence is normalized to the spatial coherence calculated at  $|\vec{d}_{ij}| = 1.3 \mu m$ .

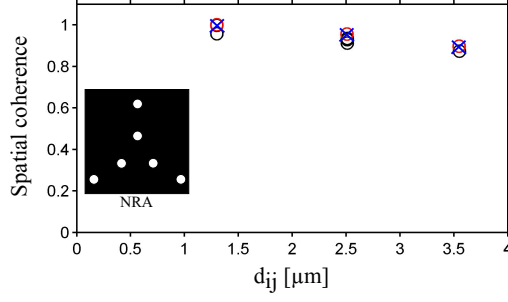


Figure 1.8: NRA case. Single pulse calculation of the spatial coherence, using the multiple apertures method, for 200 pulses interferences with pointing instability (blue cross). Simulation of the spatial coherence after the accumulation of the 200 pulses interference (black circles). Spatial coherence of reference (red circles). The results of the spatial coherence is normalized to the spatial coherence calculated at  $|\vec{d}_{ij}| = 1.3 \mu m$ .

In the case of the single pulse method with a NRA, the result of the simulation is presented in Fig. 1.8. The single pulse result is then equal to the spatial coherence of the reference (red circles). When the accumulation of 200 pulses is considered, an error is induced in the measurement. The maximum induced error corresponds to 3% of the spatial coherence of the reference, which is smaller than the error induced in the accumulation with the Young interferometer.

When we consider the incoherent accumulation of  $M$  pulses that do not interfere, the visibility of the two source interferogram is given by

$$V = 2\mu_{nm} \frac{\sum_{k=1}^M \sqrt{I_n^k I_m^k}}{\sum_{k=1}^M (I_n^k + I_m^k)}, \quad (1.8)$$

where  $I_n^k$  represents the aperture  $n$  illuminated by the pulse  $k$ . The spatial coherence  $\mu_{nm}$  is supposed to be shift invariant. From Eq. 1.8 it is clear that the individual intensity for each pulse is needed to retrieve the spatial coherence. The supposition of a unique intensity at each aperture  $I_1$  and  $I_2$  implies that Eq. 1.8 must be modified as:

$$V = 2\mu_{nm} \frac{\sqrt{I_{nT} I_{mT}}}{I_{nT} + I_{mT}}, \quad (1.9)$$

where  $I_{nT} = \sum_{k=1}^M I_n^k$  is the total intensity in the aperture  $n$  after the accumulation of  $M$  pulses. In the particular case where the beam position is fixed, we have  $I_n^k = I_n$ , and if the 2 apertures have the same intensity  $I_n = I_m$  then Eqs 1.8 and 1.9 give the usual result  $V = \mu_{nm}$ . Otherwise it is necessary to measure the individual intensity for each pulse to avoid the error induced from the discrepancy between the Eqs. 1.8 and 1.9.

In the case of the NRA method, if we consider the accumulation case, Eqs. 1.5 becomes

$$\begin{aligned}
|\mu_{13}| &= \frac{C_{13}}{\sum_{k=1}^M \sqrt{I_1^k I_3^k}} \frac{S_0}{|c_0|} \\
|\mu_{23}| &= \frac{C_{23}}{\sum_{k=1}^M \sqrt{I_2^k I_3^k}} \frac{S_0}{|c_0|} \\
|\mu_{12}| &= \frac{C_{12}}{\sum_{k=1}^M \sqrt{I_1^k I_2^k}} \frac{S_0}{|c_0|}
\end{aligned} \tag{1.10}$$

Using the relations given in Eq. 1.7 supposes an unique intensity for each aperture  $I_n = \sum_{k=1}^M I_n^k$ . This is the source of the error in Fig. 1.8. An exact solution to the set of equations 1.10 can be made if the intensity of the beam is known for each pulse. A comparison of Eqs. 1.10 with the supposition of an unique intensity  $I_n = \sum_{k=1}^M I_n^k$ , and the Eq. 1.9 shows that the error induced in the case of the 2 sources interference and the method of multiple apertures is the same. The difference in the error induced in the simulations (Figs. 1.8 - 1.7) is the additional assumption that  $I_n = I_m$ . The results show clearly that even in the case of accumulation of signal with a beam pointing instability the use of the method with multiple apertures is a better option. It generates a smaller error than the assumption of equal intensity in the 2 source interferometer. Even if we measure the total intensity at each aperture for the 2 source interferometer the result will be the same as in the case of the multiple apertures where the measurement of the intensity is not needed. If we want to avoid errors with the accumulation of the signal then we need to measure the intensity of each pulse or use the single pulse technique presented in this chapter.

## 1.2 Experimental results with HH sources

Two different NRA (Fig. 1.9) were used to characterize of the spatial coherence of a high harmonic source.

The NRA were patterned using a focused ion beam in a  $\text{Si}_3\text{Ni}_4$  membrane of 250nm thickness with a gold layer of 50 nm. The NRA with 6 apertures (Fig. 1.9 (a)) has an overall size of  $4 \mu\text{m} \times 4 \mu\text{m}$  with an aperture diameter of 380 nm, while for the NRA with 5 apertures (Fig. 1.9 (b)) the aperture diameter is 400 nm and the NRA overall size is  $3.5 \mu\text{m} \times 3.3 \mu\text{m}$ . The first NRA is composed of two concentric arrays of 3 equidistant apertures (apertures  $\{1,2,3\}$  and  $\{4,5,6\}$ ). In the case of a beam with a shift invariant spatial coherence, if the distance  $|\vec{d}_{41}| = |\vec{d}_{12}|$  we have that  $|\mu_{14}| = |\mu_{12}|$  and the system of equations generated with the array (Fig.1.9 (a)) can be solved in terms of one reference aperture. The intensity of each aperture can be calculated in terms of the aperture reference using Eq. 1.7.

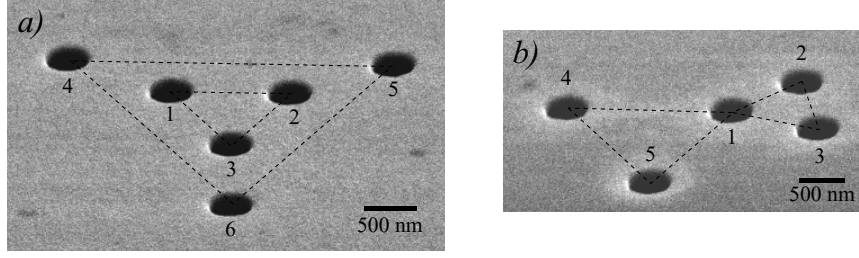


Figure 1.9: SEM image of the NRA use to measure the coherence of a high harmonic beam. They have been produced using the focused ion beam of the CSNSM facility in Orsay. The image has been taken at an angle of  $60^\circ$  due to geometry of the focused ion beam. a) NRA with 6 apertures b) NRA with 5 apertures.

$$\begin{aligned}
 I_2 &= I_1 \left( \frac{C_{23}}{C_{13}} \right)^2, & I_3 &= I_1 \left( \frac{C_{23}}{C_{12}} \right)^2, \\
 I_4 &= I_1 \left( \frac{C_{23}C_{14}}{C_{12}C_{13}} \right)^2, & I_5 &= I_4 \left( \frac{C_{56}}{C_{46}} \right)^2, \\
 & & I_6 &= I_4 \left( \frac{C_{56}}{C_{45}} \right)^2,
 \end{aligned} \tag{1.11}$$

The spatial coherence of the different pairs of apertures  $\{n,m\}$  can be calculated with the relation  $\mu_{nm} = C_{nm} / (\sqrt{I_n I_m} B_0)$ .

In the case of the NRA with 5 apertures (Fig. 1.9 (b)), we have two systems of 3 equidistant apertures ( $\{1,2,3\}$  and  $\{1,4,5\}$ ) with the aperture 1 as a common reference aperture. The solution to the system of equations can be directly solved applying Eq.1.7 to each one of the two equidistant systems.

$$\begin{aligned}
 I_2 &= I_1 \left( \frac{C_{23}}{C_{13}} \right)^2, & I_3 &= I_1 \left( \frac{C_{23}}{C_{12}} \right)^2, \\
 I_4 &= I_1 \left( \frac{C_{45}}{C_{15}} \right)^2, & I_5 &= I_1 \left( \frac{C_{45}}{C_{14}} \right)^2,
 \end{aligned} \tag{1.12}$$

The NRA is shown in (Fig. 1.9) were used to measure the spatial coherence of a table-top high harmonic beamline generated with the IR femtosecond laser LUCA at CEA-Saclay, France. The HH beam was generated by focusing the IR beam ( $f = 5.6$  m) in a gas cell full of Neon. The measurements were made with two different parameters of generation, a gas cell of 5 cm length with a gas pressure of 6.0 mbar and 6.5 cm length with a gas pressure of 5.5 mbar. The soft X-ray beam delivers up to  $4 \times 10^{10}$  photons per pulse, within a spectral bandwidth  $\lambda/\Delta\lambda = 150$  and 20 fs pulse duration [73]. The coherence of the 33rd harmonic ( $\lambda = 24$  nm) was measured in the focal plane of an off axis parabola of 200 mm focal length. The selection of the harmonic is made with a  $B_4C/Si$  multilayer coating deposited on one half of the parabola (the other half has a coating to select H39). The beam size at the focal plane of the parabola is  $5 \mu\text{m} \times 7 \mu\text{m}$ . The far-field diffraction pattern of the NRA was

registered with an X-ray CCD camera at a distance  $z = 30 \pm 1$  mm from the NRA. The CCD has  $2048 \times 2048$  square pixels with a size  $p = 13.5 \mu\text{m}$ .

Fig. 1.10 presents the experimental results using the NRA of 6 apertures (Fig. 1.9 (a)). The diffraction pattern (Fig. 1.10 (a)) corresponds to the accumulation of 200 pulses. The Fourier transform of the diffraction pattern (Fig. 1.10 (b)) is the experimental NRA autocorrelation illuminated with the harmonic beam (H33). Fig. 1.10 (c) is the simulation of the NRA autocorrelation in the case of a uniform beam profile and a full spatial coherence. In that particular case, all the peaks of the autocorrelation have the same value. The experimental autocorrelation presents all the peaks associated to the 15 pairs of apertures of the NRA. It means that the whole NRA was illuminated and that the degree of coherence between the different pairs of apertures is larger than zero. That is a direct consequence of the proportionality between the amplitude of the peaks in the autocorrelation with the spatial coherence and intensity of each pair of apertures. The nonuniform intensity profile and the partial spatial coherence of the beam generate the variations in the amplitude of the peaks in the experimental autocorrelation.

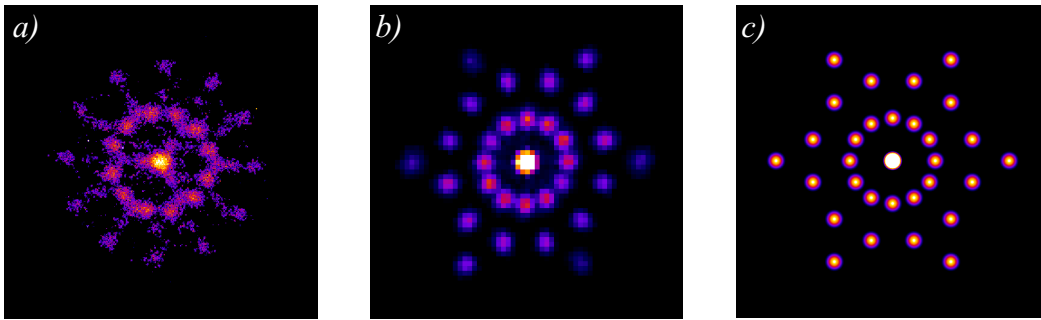


Figure 1.10: a) Experimental diffraction of H33 through the NRA (Fig. 1.9 (a)). Accumulation of 200 pulses. b) Fourier transform of (a). c) Simulation of the autocorrelation of NRA (Fig. 1.9 (a)) when the intensity and spatial coherence are uniform.

The spatial coherence of each pair of apertures was calculated using the amplitude of the peaks in the autocorrelation (Fig. 1.10 (b) and Eqs. 1.11). The result after normalization, as a function of the magnitude of the distance  $|d_{nm}|$ , is presented in Fig. 1.11 (black circles). This result was obtained by using aperture number 1 of the NRA as reference aperture.

The measured spatial coherence were fitted by a Gaussian distribution of radius  $w_c = 4.7 \pm 0.2 \mu\text{m}$  (red line). The dispersion in the calculation of the spatial coherence is larger than the one presented in the simulation of the precedent section (Fig. 1.8). The maximum standard deviation (std) is 0.08 which corresponds to an error of 14% in the calculation of the degree of coherence. The dispersion is an effect of the signal accumulation, which is highly dependent of the pulse to pulse intensity variation at each aperture.



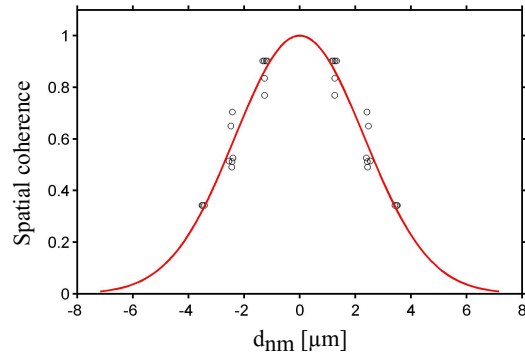


Figure 1.11: Calculation of the spatial coherence of H33 from the experimental data using the NRA with 6 apertures (Fig.1.9 (a)) using the aperture 1 as the reference (black circles). Gaussian fit of the calculation (red line).

We can see clearly this effect in the simulation presented in Fig. 1.12 (a). For this simulation the NRA of 6 apertures (Fig. 1.9 (a)) was used with the supposition of a Gaussian degree of coherence ( $w_c = 7.07 \mu\text{m}$ ) and an elliptical intensity distribution of radius  $w_x = 5 \mu\text{m}$  and  $w_y = 7.07 \mu\text{m}$ . An accumulation of 200 pulses with a random pointing variation was considered (the maximum variation corresponds to  $5 \mu\text{m}$ ). Two different cases were simulated, the elliptical intensity (black squares) and the intensity distribution tilted  $45^\circ$  respect to the horizontal (blue circles). The same set of 200 random positions was used for the two cases.

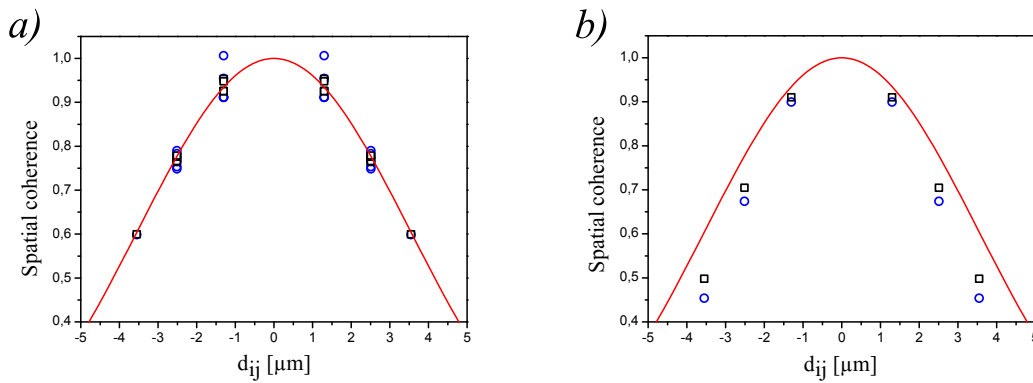


Figure 1.12: Simulation of the spatial coherence calculation using a) NRA method. b) Young interference method, assuming the same intensity at each aperture. For the simulation a beam with a Gaussian coherence of radius  $w_c = 7.07 \mu\text{m}$  (red line) was used. The black squares correspond to the spatial coherence calculated assuming an elliptical beam profile of radius  $w_x = 5 \mu\text{m}$  and  $w_y = 7.07 \mu\text{m}$ . The blue circles are the result of the spatial coherence calculation when the intensity profile is tilted  $45^\circ$  respect to the horizontal. The simulation was made using the accumulation of 200 pulses with a maximum beam shift of  $5 \mu\text{m}$ .

We can see how a variation in the orientation of the intensity distribution on the array may induce a larger dispersion. The result with the NRA method (Fig. 1.12 (a)) shows that in the case of the non-tilted intensity profile, the maximum standard deviation is 0.01 which corresponds to a maximum error in the calculation of the degree of coherence of 1.3%. For the case of the tilted intensity profile the maximum standard deviation increases to 0.03, which corresponds to an error of 3.5%. A Gaussian fit of the degree of coherence for the non-tilted and the tilted case gives a radius of coherence  $w_c = 7.01 \pm 0.05 \mu\text{m}$  and  $w_c = 7.0 \pm 0.1 \mu\text{m}$ . The discrepancy with the radius of the degree of coherence used for the simulation is 1%.

The effect of a higher variation in the pulse to pulse intensity at each aperture can be seen also in the case of the Young interferometry. Fig. 1.12 (b) presents the simulation of the spatial coherence calculated with the method of Young interferogram assuming the same intensity at each aperture. The same conditions as for the simulation of the NRA method (Fig. 1.12 (a)) were considered. A Gaussian fit of both cases, non-tilted (black squares) and tilted (blue circles) gives a radius of  $6.01 \mu\text{m}$  and  $5.65 \mu\text{m}$  respectively. This corresponds to a discrepancy of 15% and 20% respectively.

We can take into account the experimental effect of the signal to noise ratio (SNR) and the pulse to pulse variations of the intensity distribution in a threshold factor that determines the minimum contrast of the interferogram that can be detected for each one of the pulses before calculation of the accumulation. The simulation of Fig. 1.13 was made with the same parameters as in Fig. 1.12 (a) with a threshold that corresponds to 8% of the maximum contrast.

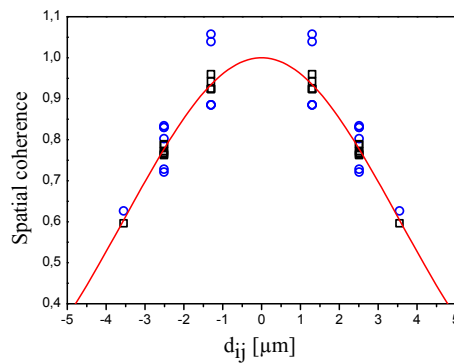


Figure 1.13: Effect of the SNR in the simulation of the spatial coherence calculation using the NRA method. The simulation was made using a threshold of 8% in the pulse to pulse signal. The same parameters as in the case of Fig. 1.12 were used. The black squares correspond to the spatial coherence calculated assuming the elliptical beam profile. The blue circles are the result of the spatial coherence calculation when the intensity profile is tilted  $45^\circ$  with respect to the horizontal. The red line presents the Gaussian spatial coherence used for the simulation.

The maximum standard deviation in the case of the non-tilted intensity profile is 0.01 and for the tilted intensity profile is 0.077, which correspond to an error of 1.5% and 8.2% respectively. A Gaussian fit of the results gives a radius of  $w_c = 7.0 \pm 0.1 \mu\text{m}$  for the non-tilted intensity profile and  $w_c = 7.3 \pm 0.4 \mu\text{m}$  for the tilted intensity profile, which corresponds to a discrepancy respectively of 1% and 3% with respect to the reference degree of coherence.

This result shows that higher variations in the pulse to pulse intensity at each aperture increase the dispersion and therefore the error of the degree of coherence calculated with the NRA technique increases. However, the discrepancy induced in the measurement is smaller than the one obtained when using the Young interferometer method.

As we have seen in Eq.1.11, we can calculate the spatial coherence in terms of the reference aperture intensity. For this NRA (Fig. 1.9 (a)) any of the apertures can work as the aperture reference. We have used the central apertures {1,2,3} as reference apertures because the Gaussian beam profile presents a higher intensity in this zone. Lower intensity references are more affected by errors generated with the signal to noise ratio. A comparison of the Gaussian fits using the reference apertures {1,2,3} is presented in Fig. 1.14. The radius of the Gaussian distributions with respect to the reference aperture 2 and 3 are  $w_c = 5.4 \pm 0.2 \mu\text{m}$  and  $w_c = 4.9 \pm 0.2 \mu\text{m}$  respectively. This corresponds to a mean radius of  $\bar{w}_c = 5 \mu\text{m}$  with a standard deviation of 6%.

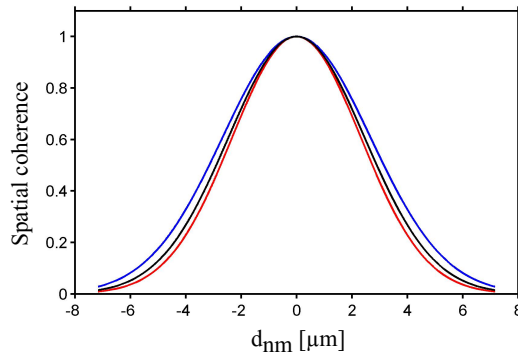


Figure 1.14: Gaussian fit of the spatial coherence of H33 using the NRA with 6 apertures (Fig.1.9 (a)) with respect to the aperture reference 1 red line, 2 black line and 3 blue line.

The NRA with 5 apertures (Fig. 1.9 (b)) was used to measure the degree of coherence of H33 with different parameters of generation. In this case the HH source was generated in a cell with a length of 6.5 cm, full of Neon at 5.50 mbar. The experimental diffraction pattern after the accumulation of 200 pulses is presented in Fig. 1.15 (a). We can see the agreement between the position of the different peaks of the experimental (Fig. 1.15 (b)) and the simulated autocorrelations (Fig. 1.15 (c)). Similar to the previous experimental result (Fig. 1.10), the experimental autocorrelation shows a modulation in amplitude of the peaks induced by the non-uniform intensity and coherence of the source.

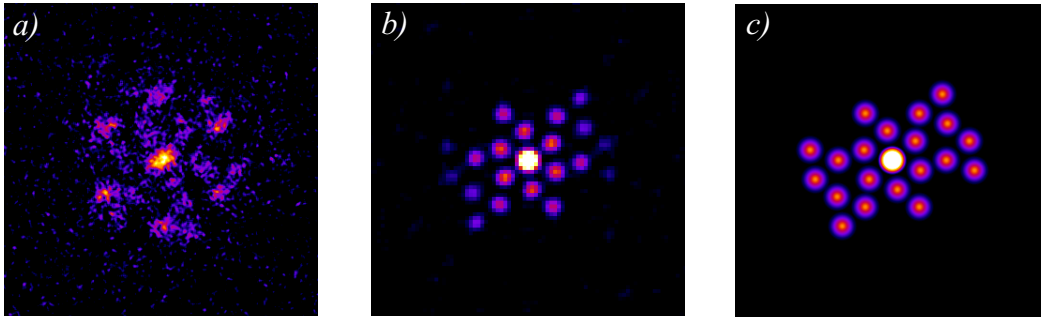


Figure 1.15: a) Experimental diffraction of H33 through the NRA (Fig. 1.9 (b)). Accumulation of 200 pulses. b) Fourier transform of (a). c) Simulation of the autocorrelation of NRA (Fig. 1.9 (b)) when the intensity and spatial coherence are uniform.

The calculation of the degree of coherence was made using the Fourier transform of the diffraction pattern (Fig. 1.15 (b) and Eqs. 1.12). The result of the calculated degree of coherence (black circles) and the Gaussian fit (red line) are presented in the Fig. 1.16. The Gaussian fit corresponds to a radius  $w_c = 4.0 \pm 0.2 \mu\text{m}$ . The maximum dispersion corresponds to a standard deviation of 0.11, which is 1.4 time larger than the maximum standard deviation of the spatial coherence measured with other parameters of generation (Fig. 1.11). As we have seen, a larger standard deviation can be explained by a larger pulse to pulse variation of the intensity profile. This variation can be generated by a pointing instability but also as a pulse to pulse change in the shape of the intensity profile. Indeed, the new generation parameters induce a larger instability in the intensity profile as well as a lower degree of coherence.

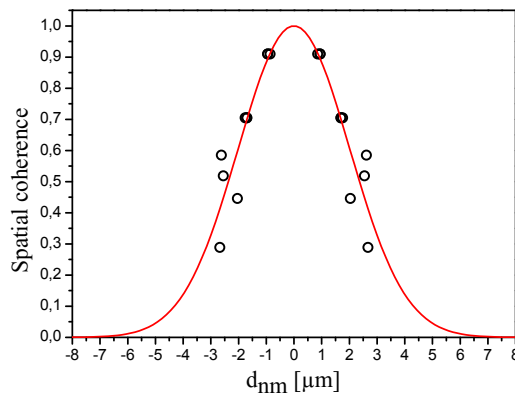


Figure 1.16: The black dots present the measurement of the spatial coherence with the technique proposed in this chapter using the diffraction of H33 through the NRA (Fig. 1.9 (b)). The red line is a Gaussian fit of the experimental data with a radius of  $w_c = 4.0 \pm 0.2 \mu\text{m}$

In conclusion, the technique was successfully validated using the diffraction of the 33rd harmonic of the femtosecond IR laser LUCA at CEA. Two different NRA were used to mea-

sure experimentally the spatial coherence. The measurements were made with two different parameters of harmonic generation, a gas cell of 5 cm length with a gas pressure of 6.0 mbar and 6.5 cm length with gas pressure of 5.5 mbar, the radius of the spatial coherence then changed from 4.7  $\mu\text{m}$  to 4.0  $\mu\text{m}$  respectively. These measurements present clearly the Gaussian behavior of the spatial coherence at the two different high harmonic generation conditions. The results show that it is possible to do a characterization of the spatial coherence in terms of the influence of the generation process. However, to avoid errors induced by the pointing fluctuations the flux of photons and the stability of the beam have to be improved, thus making single shot measurements highly reliable. In this way the effect of the spatial coherence can be isolated from the pointing fluctuations and the generation conditions.

---

### 1.3 Extension of single shot method to the Fresnel regime

It can be convenient to measure the coherence in the intermediate plane, like for example at XFEL facilities where access to the beam can be difficult (access to end stations is restricted). It also permits the implementation of a permanent diagnostic of the beam. This technique of characterization can be implemented in a XFEL facility like the LCLS at SLAC where it could be possible to do the characterization in real time using the interference in the intermediate Fresnel regime without any additional optics to focus the FEL beam. To build a station to characterize the beam with a focusing system is much more expensive than to use the interference of a part of the beam in the intermediate plane. In this section, a variation of the theoretical description of the method of multiple apertures [58] is presented. In this case it is possible to use an interferogram generated in the Fresnel regime and not necessarily at focus (far field approximation). The description is given in terms of the Fresnel diffraction. The main difference with the far field approximation is the quadratic term of phase that will modulate the autocorrelation of the mask.

Following the description of Mejía and González [58] the transmittance of an array of apertures is,

$$t(\vec{r}) = h(\vec{r}) \otimes \sum_{n=1}^N V(\vec{r}_n) \delta(\vec{r} - \vec{r}_n) . \quad (1.13)$$

According to the Fresnel diffraction equation, the field at the plane  $z$  is given by

$$V(\vec{\rho}, z) = \frac{-ie^{ikz}}{\lambda z} \iint t(x, y) e^{\frac{ik}{2z} [(\xi-x)^2 + (\eta-y)^2]} dx dy , \quad (1.14)$$

When the quadratic term in the integral of Eq. 1.14 is expanded, it is clear that the Fresnel diffraction can be written as a Fourier transform

$$V(\vec{\rho}, z) = \frac{-ie^{ikz} e^{\frac{ik}{2z}(\xi^2 + \eta^2)}}{\lambda z} \int \int t(x, y, z_0) e^{\frac{ik}{2z}[x^2 + y^2]} e^{-i2\pi[\vec{v} \cdot \vec{r}]} dx dy, \quad (1.15)$$

with  $\vec{v} = \vec{\rho}/\lambda z$ . Eq. 1.15 is then the Fourier transform of the transmittance function multiplied by a quadratic phase,

$$V(\vec{\rho}, z) = \frac{-ie^{ikz} e^{\frac{ik}{2z}(\xi^2 + \eta^2)}}{\lambda z} F \left\{ t(x, y, z_0) e^{\frac{ik}{2z}[x^2 + y^2]} \right\} \Bigg|_{\vec{v}=\vec{\rho}/\lambda z}. \quad (1.16)$$

Taking into account the convolution theorem, we can write Eq. 1.15 as

$$V(\vec{\rho}, z) = \frac{-ie^{ikz} e^{\frac{ik}{2z}(\xi^2 + \eta^2)}}{\lambda z} \left[ F \left\{ t(x, y, z_0) \right\} \Bigg|_{\vec{v}=\vec{\rho}/\lambda z} \otimes F \left\{ e^{\frac{ik}{2z}[x^2 + y^2]} \right\} \Bigg|_{\vec{v}=\vec{\rho}/\lambda z} \right]. \quad (1.17)$$

From Eq. 1.13 and the Fourier transform of the quadratic term in Eq. 1.17, the field at the plane  $z$  is given by

$$V(\vec{\rho}, z) = \frac{-ie^{ikz} e^{\frac{ik}{2z}(\xi^2 + \eta^2)}}{\lambda z} \left[ H \left( \frac{\vec{\rho}}{\lambda z} \right) \sum_{n=1}^N V(\vec{r}_n) e^{-i2\pi \left( \frac{\vec{\rho}}{\lambda z} \cdot \vec{r}_n \right)} \otimes i\lambda z e^{-i\pi \lambda z \left( \frac{\vec{\rho}}{\lambda z} \right)^2} \right], \quad (1.18)$$

where  $H(\vec{v}) = FT \{h(\vec{r})\}$  is the Fourier transform of the function that describes the geometrical shape of the apertures.

Now, to calculate the intensity of the diffraction pattern at the plane  $z$  we can use the fact that  $J(\vec{r}_1, \vec{r}_1) = I(\vec{r}_1)$ . Using the definition of the mutual intensity given at the beginning of Chapter 1,  $J(\vec{r}_1, \vec{r}_2) = \langle V^*(\vec{r}_1) V(\vec{r}_2) \rangle_T$  and the field given in Eq. 1.18 with  $\vec{\rho} = \vec{\rho}_1 = \vec{\rho}_2$ , the intensity can be written as

$$I(\vec{\rho}, z) = \frac{1}{(\lambda z)^2} \langle D(\vec{\rho}, z) D^*(\vec{\rho}, z) \rangle, \quad (1.19)$$

with,

$$D(\vec{\rho}, z) = \left[ H \left( \frac{\vec{\rho}}{\lambda z} \right) \sum_{n=1}^N V(\vec{r}_n) e^{-i2\pi \left( \frac{\vec{\rho}}{\lambda z} \cdot \vec{r}_n \right)} \otimes i\lambda z e^{-i\pi \lambda z \left( \frac{\vec{\rho}}{\lambda z} \right)^2} \right]. \quad (1.20)$$

Following the convolution theorem, the Fourier transform of the intensity  $\tilde{I}(\vec{r}, z)$  is then,

$$\tilde{I}(\vec{r}, z) = \frac{1}{(\lambda z)^2} \langle F \{ D(\vec{\rho}, z) \} \otimes F \{ D^*(\vec{\rho}, z) \} \rangle. \quad (1.21)$$

From Eq. 1.20 we find that the Fourier transforms  $\tilde{D}(\vec{r}, z)$  and  $\tilde{D}^*(\vec{r}, z)$  are given by

$$\tilde{D}(\vec{r}, z) = \left[ F \left\{ H \left( \frac{\vec{\rho}}{\lambda z} \right) \right\} \otimes \left( \sum_{n=1}^N V(\vec{r}_n) \lambda z \delta(\vec{r} + \vec{r}_n) \right) \right] \lambda z e^{\frac{i\pi}{\lambda z} (\vec{r})^2}, \quad (1.22)$$

$$\tilde{D}^*(\vec{r}, z) = \left[ F \left\{ H^* \left( \frac{\vec{\rho}}{\lambda z} \right) \right\} \otimes \left( \sum_{m=1}^N V^*(\vec{r}_m) \lambda z \delta(\vec{r} - \vec{r}_m) \right) \right] \lambda z e^{-\frac{i\pi}{\lambda z} (\vec{r})^2}. \quad (1.23)$$

After the substitution of Eqs. 1.22 - 1.23 in Eq. 1.21, we have that

$$\tilde{I}(\vec{r}, z) = (\lambda z)^2 \sum_{n=1}^N \sum_{m=1}^N \langle V(\vec{r}_n) V^*(\vec{r}_m) \rangle \left( [F\{H(\vec{v})\} \otimes \delta(\vec{r} + \vec{r}_n)] e^{\frac{i\pi}{\lambda z}(\vec{r})^2} \right) \otimes \left( [F\{H^*(\vec{v})\} \otimes \delta(\vec{r} - \vec{r}_m)] e^{-\frac{i\pi}{\lambda z}(\vec{r})^2} \right). \quad (1.24)$$

In terms of the degree of coherence (Eq. 1.2), and taking into account the property of the Fourier transform  $F\{F\{h(x)\}\} = h(-x)$ , we find the description of  $\tilde{I}$  in the Fresnel regime

$$\tilde{I}(\vec{r}, z) = (\lambda z)^2 \sum_{n=1}^N \sum_{m=1}^N \sqrt{I_n I_m} \mu_{mn} \left[ h(-(\vec{\rho} + \vec{\rho}_n)) e^{\frac{i\pi}{\lambda z}(\vec{r})^2} \right] \otimes \left[ h(\vec{\rho} - \vec{\rho}_m) e^{-\frac{i\pi}{\lambda z}(\vec{r})^2} \right]. \quad (1.25)$$

If the far field approximation is taken into account the term of phase is equal to 1 and then the same result used in the section 1.1.1 is found.

In Eq. 1.25 we can see that a quadratic term of phase now modulates the correlation of the geometric function that describes the apertures in the array. The effect of this quadratic phase has to be filtered out to measure the spatial coherence using the interference at the intermediate diffraction regime but otherwise the results presented before are still valid.

---

## 1.4 Partially coherent holographic imaging

As it has been presented in the introduction of this chapter, the spatial coherence of XUV sources is an important factor for lens-less imaging. CDI [27–29] and FTH [56] assume a total spatial coherence of the field used for object irradiation. However, it has been shown that the reconstruction depends critically on the spatial coherence [35, 87, 90, 91]. Therefore, the assumption of total coherence is not generally appropriate. Actually, XUV sources generated by FEL or HHG have a partial spatial coherence [50, 88].

We need to take into account the fact that the spatial coherence is a function of four variables  $\mu(x_1, y_1, x_2, y_2)$  (Eq. 1.2). As the diffraction is related to the spatial coherence, the intensity of the diffracted beam after propagation (Eq. 1.33) is also a function of four dimensional variables. This four-variable integral is not only difficult to solve in some cases, because the problem not always has an analytical solution and the numerical calculation can be not trivial, but also because it implies that a four dimensional characterization of the spatial coherence has to be done. Consequently, people usually use the Shell model beam approximation for the spatial coherence. For a Shell model beam the magnitude and phase of the spatial coherence is shift invariant, i.e. it is a function of the magnitude of the separation vector  $|\vec{d}_{12}| = \|(\vec{r}_1 - \vec{r}_2)\|$ . Thus, reducing the spatial coherence to a two-dimensional function.

This approximation is mainly valid for the magnitude of the spatial coherence, but the phase of the spatial coherence is not always shift invariant. The most common example is

the spatial coherence of an incoherent source after propagation [78]. From the Van Cittert-Zernike theorem we know that the spatial coherence of such a source is given by the Fourier transform of the intensity distribution [38]. In this case of a spatially incoherent source with a Gaussian distribution of intensity, the phase of the spatial coherence (after propagation) is a function of  $(\vec{r}_1^2 - \vec{r}_2^2)$  [78] which is a factor that depends on the magnitude and the direction of the separation distance  $\vec{d}_{12}$ .

Some questions then appear. How does the object reconstruction change in terms of the spatial coherence of the source? Do we need to perform a four-dimensional spatial coherence characterization of the source in the case where the phase term contains shift variations?

The compensation of the spatial coherence effect in CDI has been already studied. Phase curvature in the incident field can compensate (in some cases) the effect of the spatial coherence in the image reconstruction [91] but a small degree of partial spatial coherence may result in a failure to retrieve the phase. A modification of the CDI iterative algorithm has been proposed to improve the wave field reconstructions when a field with a known spatial coherence is used [90]. In both cases a Shell model beam approximation was used.

In this section, the theoretical description of Fourier transform holography with a partially coherent source without restrictions in the phase term of the spatial coherence is presented. An analytic result of the object reconstruction factor in terms of the spatial coherence was derived. We show that FTH does not need the four dimensional spatial coherence characterization even in the case where the phase of the coherence is shift variant. The two dimensional spatial coherence characterization of the source presented in this chapter is then enough to improve the object reconstruction.

### **FTH: Fourier Transform Holography with completely coherent sources**

FTH is a technique based on the interference of the object diffraction with a reference beam. Therefore, a certain degree of spatial coherence is needed to be able to generate the interference. The term associated with this interference in the total description of the diffraction pattern is called the holographic term. In the basic case of a fully spatially coherent source, the straightforward object reconstruction is given by an inverse Fourier transform of the holographic term, as we will present in the following mathematical description.

In the case of a fully spatially coherent and monochromatic field, the intensity of the far field diffraction ( $I(\vec{\rho}) = |V(\vec{\rho}, z)|^2$ ) can be calculated from Eq. 2

$$I(\vec{\rho}, z) = \frac{1}{\lambda^2 z^2} T^2(\vec{\rho}) \Big|_{\vec{\rho}/\lambda z} \quad (1.26)$$

The inverse Fourier transform of the holographic intensity is then proportional to  $FT^{-1}\{T^2(\vec{\rho})\} = t(\vec{r}) \otimes t(\vec{r})$ . Taking into account the spatial scale in terms of the wavelength in Eq. 1.26 and the property  $FT\{t(\vec{r}/a)\} = |a| T(a\vec{\rho})$  we have that



$$\begin{aligned}
 FT^{-1} \{I(\vec{\rho}, z)\} &= \frac{1}{\lambda^2 z^2} FT^{-1} \{T^2(a\vec{\rho})\} \\
 &= \frac{1}{|a|^2 \lambda^2 z^2} \left[ t\left(\frac{\vec{r}}{a}\right) \otimes t\left(\frac{\vec{r}}{a}\right) \right],
 \end{aligned} \tag{1.27}$$

with  $a = 1/\lambda z$ , we finally have that

$$FT^{-1} \{I(\vec{\rho}, z)\} = [t(\vec{r}) \otimes t(\vec{r})] \Big|_{\lambda z \vec{r}}, \tag{1.28}$$

If we add a reference to the transmittance function of the object, the total transmittance  $t(\vec{r})$  can be written as

$$t(\vec{r}) = o(\vec{r}) + r(\vec{r}), \tag{1.29}$$

where  $o(\vec{r})$  and  $r(\vec{r})$  are respectively the object and reference transmittance. Thus, the Fourier transform of the diffraction pattern detected in the holographic case can be calculated from Eqs. 1.28 and 1.29

$$FT^{-1} \{I(\vec{\rho}, z)\} = [o(\vec{r}) \otimes o(\vec{r}) + r(\vec{r}) \otimes r(\vec{r}) + o(\vec{r}) \otimes r(\vec{r} - \vec{r}_0) + r(\vec{r} + \vec{r}_0) \otimes o(\vec{r})] \Big|_{\lambda z \vec{r}}, \tag{1.30}$$

where  $\vec{r}_0$  is the vector distance between the object and reference centers. The two last correlation terms in Eq. 1.30 are called the holographic terms. For a point-like reference ( $r(\vec{r}) = \delta(\vec{r})$ ), the holographic term is equal to the object transmittance  $o(\vec{r})$  and we have two reconstructions of the object centered at ( $\vec{r}' = \pm \vec{r}_0$ ), with  $\vec{r}' = \lambda z \vec{r}$ . This result is usually presented as a function of the vector  $\vec{r}$  (i. e. ( $\vec{r} = \pm \vec{r}_0$ )) and the factor ( $\lambda z$ ) are taken into account in the relation between the physical parameters of the hologram recorded and its discrete representation (pixels) [31],

$$\Delta r = \frac{\lambda z}{N \Delta k}, \tag{1.31}$$

where  $\Delta r$  is the pixel size in the holographic reconstruction,  $N$  is the total number of pixels used to calculate the Fourier transform of the hologram and  $\Delta k$  is the pixel size of the CCD camera. In the discrete representation, the position of the reconstruction is given by

$$\vec{P} = \vec{r}_0 / \Delta r. \tag{1.32}$$

For an extended reference [32, 41] an additional derivative step is necessary to generate the reconstruction of the object.

As we have seen, this description is based on the diffraction pattern of a fully spatially coherent beam (Eq. 2). Therefore, any change in the spatial coherence of the beam will generate a degradation of the reconstruction [35]. The general case of a partially coherent field can be taken into account if we consider the diffraction equations given for a partially

coherent field, instead of the particular case of a fully coherent field. The general description of the Fourier transform holography in terms of the spatial coherence is developed in the next section.

### Fourier Transform Holography with partially coherent sources

To obtain an analytical description of FTH in terms of the spatial coherence of the illumination field we follow the description given by Goodman [38]. In that way, we can calculate the field intensity at a plane  $z > 0$  as the superposition of all the interference fringes generated by the different pairs of point-like sources present in the field at  $z = 0$  [38]. We can then relate the diffraction intensity at a plane  $z$  to the mutual intensity  $J_0(\vec{r}_1, \vec{r}_2)$  of the field at a plane  $z = 0$  by using the following equation [38],

$$I(\vec{\rho}, z) = \frac{1}{\lambda^2 z^2} \int \int \int \int J'_0(\vec{r}_1, \vec{r}_2) e^{\frac{i2\pi}{\lambda z} [\vec{\rho}_1 \cdot \vec{r}_1 - \vec{\rho}_2 \cdot \vec{r}_2]} d^2\vec{r}_1 d^2\vec{r}_2, \quad (1.33)$$

where  $J'_0(\vec{r}_1, \vec{r}_2)$  is the mutual intensity at the exit pupil of the system. In the case when the field is diffracted through an object of transmittance  $t(\vec{r})$ , the mutual intensity is given by [38]

$$J'_0(\vec{r}_1, \vec{r}_2) = t(\vec{r}_1) t^*(\vec{r}_2) J_0(\vec{r}_1, \vec{r}_2). \quad (1.34)$$

In FTH we are interested in the Fourier transform of the diffraction intensity [23, 56, 85]. By taking the Fourier transform of Eq. 1.33 we obtain [38]

$$\tilde{I}(\vec{v}, z) = \int \int J'_0(\vec{r}_1, \vec{r}_1 - \lambda z \vec{v}) d^2\vec{r}_1, \quad (1.35)$$

where  $\vec{v} = \Delta\vec{r}/\lambda z$ , with  $\Delta\vec{r}$  the distance between two points in the transmittance plane. In our case (FTH), the transmittance function is given by the superposition of the object and reference transmittance (Eq. 1.29). For a point-like reference, the transmittance can be written as

$$t(\vec{r}) = o(\vec{r}) + \delta(\vec{r} - \vec{r}_n), \quad (1.36)$$

with  $\delta(\vec{r} - \vec{r}_n)$  the Dirac delta function centered at the position  $\vec{r}_n$ . From Eq. 1.36 and Eq. 1.35 we find an analytical expression of the holographic term for the object reconstruction as a function of the spatial coherence of the illumination field.

$$\begin{aligned} \tilde{I}(\vec{v}, z) = & \int \int J_0(\vec{r}_1, \vec{r}_1 - \lambda z \vec{v}) [o(\vec{r}_1) o^*(\vec{r}_1 - \lambda z \vec{v})] d^2\vec{r}_1 + \\ & \int \int J_0(\vec{r}_1, \vec{r}_1 - \lambda z \vec{v}) [\delta(\vec{r}_1 - \vec{r}_n) \delta^*(\vec{r}_1 - (\lambda z \vec{v} + \vec{r}_n))] d^2\vec{r}_1 + \\ & \int \int J_0(\vec{r}_1, \vec{r}_1 - \lambda z \vec{v}) [o(\vec{r}_1) \delta^*(\vec{r}_1 - (\lambda z \vec{v} + \vec{r}_n))] d^2\vec{r}_1 + \\ & \int \int J_0(\vec{r}_1, \vec{r}_1 - \lambda z \vec{v}) [\delta(\vec{r}_1 - \vec{r}_n) o^*(\vec{r}_1 - \lambda z \vec{v})] d^2\vec{r}_1. \end{aligned} \quad (1.37)$$

The two first terms in Eq. 1.37 correspond to the object and reference autocorrelation, respectively. The last two terms determine the holographic factor with its complex conjugate as a function of the source mutual intensity  $J_0$ . After calculating the double integral in the third term of Eq. 1.37 we have an analytic expression that determines the object reconstruction  $O_R$  in terms of the mutual intensity of the source.

$$O_R = J_0(\vec{r}_n, \vec{r}_n + \lambda z \vec{v}) o(\vec{r}_n + \lambda z \vec{v}), \quad (1.38)$$

This means that the object reconstruction can be given directly as the object transmittance, modulated by the mutual intensity between the point-like reference and the object.

Taking into account the relation between the mutual intensity and the spatial coherence (Eq. 1.2), Eq. 1.38 can be written as,

$$O_R = \mu(\vec{r}_n, \vec{r}) \sqrt{I(\vec{r}_n)I(\vec{r})} o(\vec{r}). \quad (1.39)$$

In the particular case where the source is fully spatially coherent  $\mu(\vec{r}_n, \vec{r}) = 1$ , we obtain the same result as in FTH and the holographic term determines directly the object reconstruction. On the other hand, if the source is spatially incoherent  $\mu(\vec{r}_n, \vec{r}) = 0$ , we do not have any interference and the holographic term does not appear in the Fourier transform of the diffraction pattern ( $O_R = 0$ ).

In the case of a beam with partial coherence  $|\mu(\vec{r}_n, \vec{r})| < 1$ , we see from Eq. 1.39 that the object reconstruction is modulated by the spatial coherence between the reference and the object. As all the combinations of distances  $(\vec{r} - \vec{r}_n)$  between the object and a point-like reference are different, the reconstruction problem is non-redundant. This means that one separation point sampled in the Fourier transform of the diffraction corresponds to only one pair of points in the set of pairs generated between the point-like reference and the object (Fig. 1.17). This basic result means that the phase of the spatial coherence can be neglected in the calculation of the amplitude of the object reconstruction.

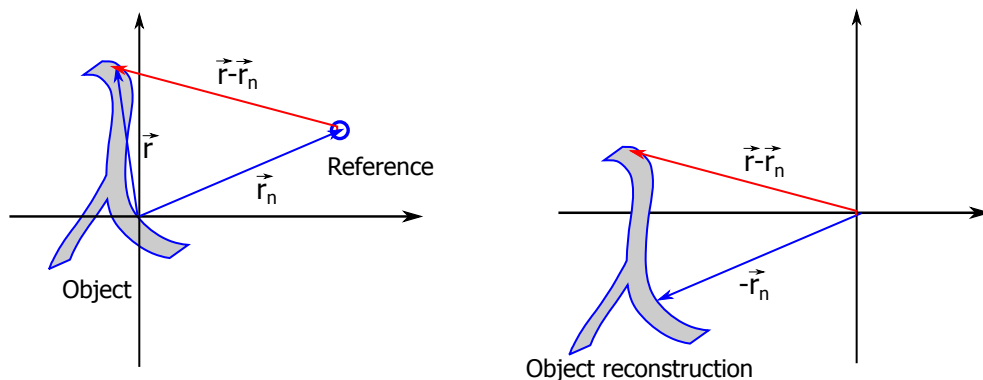


Figure 1.17: FTH reconstruction of the object

In case of an extended reference, different pair of points in the object-reference structure can have the same separation vector ( $\vec{r} - \vec{r}_n$ ), which is what we call the redundant case. The whole set of pair of points with a separation vector ( $\vec{r} - \vec{r}_n$ ) will be sampled with only one point on the Fourier transform of the diffraction. Therefore, the modulation of the object reconstruction at ( $\vec{r} - \vec{r}_n$ ) is given by the superposition of the modulation (Eq. 1.39) calculated for each pair of points with the same distance ( $\vec{r} - \vec{r}_n$ ). If the phase of the spatial coherence for the different pairs in such a set is different (shift variant phase), the total amplitude of the object reconstruction at that position ( $\vec{r} - \vec{r}_n$ ) will be modulated by the phase of the spatial coherence.

In conclusion, an analytical expression for the Fourier transform reconstruction with a partially coherent beam has been deduced. From this description we can see that any modulation in the object reconstruction induced by a shift invariant phase of the spatial coherence is avoided by using the FTH with a point-like reference. In the case of an extended reference, shift variations of the phase in the spatial coherence may generate a superposition out of phase in the object reconstruction. This can degrade the object reconstruction. As a perspective of this work we plan to study the effect of the derivative algorithms for FTH imaging with extended sources in terms of the spatial coherence.

---

## 1.5 Conclusions

The main goal of the work presented in this chapter was to develop a new technique for spatial coherence measurements that does not need the information on the source intensity distribution, thus allowing single shot characterization. The method I proposed uses a non-redundant array of apertures to sample the incoming beam. The multiple apertures technique was used to generate a system of equations that allows measuring the coherence in terms of the intensity of one aperture. This intensity factor is then normalized using the fact that the spatial coherence, as a function of the separation vector of 2 sources, is symmetric with respect to zero and should be 1 at zero. The method can be used when the spatial coherence of the source is invariant to translations.

The simulations presented in this chapter evidence the advantage of the single shot technique proposed compared to other techniques like Young interferometry (under the supposition of equal intensity at each aperture).

The numerical study on the effect of pointing instabilities on the spatial coherence measurements, under accumulation conditions, showed that the shot to shot variations of the intensity distribution induce an error in the measurement even if the intensity at each aperture is measured.

Up to now, only the information of the intensity variation from shot to shot could avoid this measurement error. The simulations demonstrated that the NRA technique

in single shot eliminates the error induced by pointing instabilities. On the other hand, in accumulation conditions the error from pointing instabilities can only be avoided by measuring the intensity variations. In any case, the error induced with the NRA technique is smaller than the one induced with the Young interferometry technique (under the supposition of equal intensity at each aperture).

The new method for the characterization of the spatial coherence proposed in this chapter was successfully implemented by measuring the spatial coherence of the 33rd harmonic of our Ti:Saph laser. We performed additional measurements with a different set of parameters of generation to show that it is possible to characterize the spatial coherence in terms of the generation parameters using this technique. A perspective of this work is to perform an experimental campaign to study the systematic variation of the spatial coherence in terms of the generation conditions. Such an experiment requires an improvement of the flux of photons to achieve single shot measurements. In this way, measurement of the spatial coherence can be isolated from any effect from intensity instability (shot to shot) that can be induced by a variation of the generation parameters.

The extension of the multiple apertures method to the interference in the intermediate diffraction approximation presented in this chapter, opens the possibility of using the method of single shot characterization not only in far field diffraction but also in the intermediate diffraction plane. In this case, it is necessary to correct the effect of the quadratic term of phase that will modulate the correlation of the apertures in the array.

The combination of the spatial coherence characterization presented in this chapter with the theoretical description of the intermediate plane diffraction developed in this section opens the option for a permanent diagnostic of the spatial coherence at large facilities such as XFEL.

At the end of this chapter we presented the deduction of an analytical expression for the Fourier transform reconstruction with a partially coherent beam. From this description we can see that any modulation in the object reconstruction induced by a shift invariant phase of the spatial coherence is avoided by using FTH with a point-like reference. In the case of an extended reference, shift variations of the phase in the spatial coherence may generate a superposition out of phase in the object reconstruction. This can degrade the object reconstruction.

---

# SOFT X-RAY WAVEFRONT CHARACTERIZATION AND APPLICATIONS

---

The spatial properties of a field determine its evolution under propagation [39]. Control of the spatial properties can be induced during the field generation process, the propagation through an optical system, or by changing the properties of the media of propagation. This basic process opens the possibilities of multiple applications of the spatial properties. In this chapter some original applications of wavefront characterization of soft X-ray pulses are presented. The wavefront was measured using a commercial Hartmann wavefront sensor. The problem of the wavefront reconstruction from a Hartmann pattern has been broadly studied in the visible range [53, 70] and successfully applied in the soft X-ray range using synchrotron, FEL and HHG sources [5, 34, 59]. An introduction to the Hartmann wavefront sensing technique is presented at the beginning of this chapter.

The first application presented is the optimization of soft and hard X-ray focusing systems. The minimization of the aberration induced by a misalignment in the focusing system is important in CDI [6, 73, 81] where the target object is supposed to be irradiated with a plane wavefront. Focusing systems are also used to increase the flux of photons on a target. Aberrations increase the focal spot size and therefore the flux of photons is deteriorated. The experiments were conducted at the HHG beamline, CEA Saclay, and FEL sources at AMO station, LCLS, and DiProI beamline, FERMI.

The second application is related to the FEL generation process. Direct beam measurements on the FEL beam shows the capability to follow the different generation modes by characterizing the X-ray wavefront. The experiment was performed at FERMI, ELETTRA in Trieste, Italy.

A final application consisted in using wavefront measurements to follow the optical properties variation of solid density plasma created by a X-ray FEL and probed with a soft X-ray HH source. This experiment was conducted at LCLS, Stanford, USA.

## 2.1 Wavefront characterization with a Hartmann sensor

The wavefront characterization presented in this chapter has been performed using a commercial Hartmann wavefront sensor "soft X-ray HASO" (developed and produced by Imagine Optic). The principle of a Hartmann sensor is to measure the variation of the wavefront with respect to a reference wave (usually spherical), sampling locally the field with an array of apertures Fig. 2.1 (a). The spot position of the "beamlets" diffracted at each aperture in the Hartmann grid depends on the incident wavefront (Fig. 2.1 (c)-(d)). The variation between the spot position of the "beamlets" generated by the unknown wavefront  $W(x,y)$  with respect to a reference wavefront ( $\Delta x, \Delta y$ ) presents a direct relation with the wavefront slopes (Fig. 2.1 (b)) [53],

$$\frac{\partial}{\partial x} W(x,y) = -\frac{\Delta x}{r} \quad \frac{\partial}{\partial y} W(x,y) = -\frac{\Delta y}{r} , \quad (2.1)$$

where  $r$  is the distance between the observation plane and the center of the ideal wavefront (Fig. 2.1 (b)).

The wavefront slopes are then determined from the distortions of the Hartmann pattern. The problem of the wavefront reconstruction from a Hartmann pattern has been broadly studied [53, 70]. The wave aberrations are described by a weighted sum of Zernike polynomials (for a circular pupil) or Legendre polynomials (for a square pupil), where each coefficient corresponds to the RMS contribution of each mode. Therefore, a fit of the wavefront retrieved in terms of Zernike or Legendre polynomials provides a direct measurement of the aberrations presented in the optical system. The wavefront sensor "Soft X-ray HASO" comes with a software that uses either a Zernike or Legendre polynomial set to retrieve the wavefront. The aberration terms are directly calculated and can be given.

Not only the position but also the beam intensity in a Hartmann pattern is recorded by a CCD placed at a distance  $z$  from the Hartmann grid. Using the intensity measured and the retrieved wavefront, the HASO software uses back-propagation functions (in a paraxial approximation) to calculate the beam profile at different planes  $z$  on the propagation direction. In this way, we can improve the focusing system in real time by following the evolution of the focal spot (as we will see in the following sections).

In the case of a direct beam measurement of the wavefront of a soft X-ray source we are then able to retrieve the beam and phase profiles in terms of the generation parameters. In this chapter we have focused on high harmonic generation and free electron laser soft X-ray sources.

Our HASO soft X-ray wavefront sensor has been designed to work with a photon energy of 30 eV - 300 eV (4 nm - 40 nm) (Fig. 2.2). The soft X-ray CCD camera used to detect the Hartmann pattern has  $1024 \times 1024$  pixels of  $13 \mu\text{m} \times 13 \mu\text{m}$ . The calibration has been

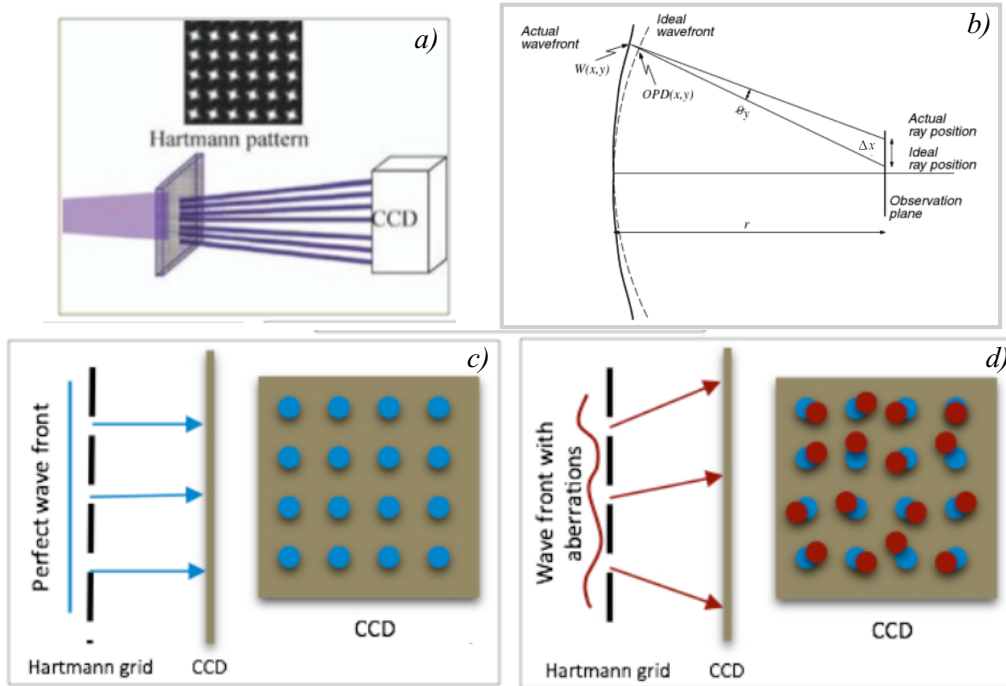


Figure 2.1: Principle of a Hartmann wavefront sensor. a) The incoming beam is sampled by a Hartmann grid, which is a regular array of holes. The projection of the beam that goes through the Hartmann pattern is captured by a soft X-ray camera. b) Relation between the variation of the ray position on the observation plane ( $\Delta x$ ) with the local variation of the wavefront  $W(x,y)$  with respect to a reference wavefront [53]. c) The reference position of the Hartmann pattern projection is generated by a perfect wavefront (wavefront sensor calibration). d) The local shift of each beamlet (red points) generated with the real wavefront with respect to the reference (blue points) is then used to do the reconstruction of the local wavefront variations. [33]

made following the standard calibration method presented in [59], where a pinhole is used to spatially filter the source generating a pure spherical reference wavefront. In our case, harmonic 25<sup>th</sup> of an IR source (32 nm) was used.

The wavefront measurement accuracy is  $\sim \lambda/75$  (rms) (root mean square). At a wavelength  $\lambda = 32$  nm, this corresponds to an accuracy of 0.42 nm (rms). From Eq. 2.1 we can see that strong variations in the wavefront produce larger spot position variations in the Hartmann pattern. A discontinuity or strong aberration (larger than  $2\pi$ ) could lead to wrong reconstructions of the wavefront. In our case, the HASO has been used in conditions without wavefront discontinuities or strong aberrations.



	$\lambda$ EUV
Aperture dimension	13 x 13 mm <sup>2</sup>
Number of sub-apertures dedicated for analysis	72 x 72
Curvature dynamic range	0.5 m to $\infty$ (diverging)
Repeatability (rms)	$\sim \lambda/200$
Wavefront measurement accuracy in absolute mode (rms)	$\sim \lambda/75$
Wavefront measurement accuracy in relative mode (rms)	$\sim \lambda/100$
Tilt measurement sensitivity (rms)	0.05 $\mu$ rad
Focus measurement sensitivity (rms)	$< 1.10^{-5} \text{ m}^{-1}$
Spatial beam sampling step	$\sim 180 \mu\text{m}$
Minimum readout time	$\sim 600 \text{ ms}$ (@2 MHz digitization)
Working photon energy (wavelength) <sup>1</sup>	30 eV - 300 eV (4 nm - 40 nm)
Compliant vacuum (hydrocarbon free, compatible with clean vacuum)	$10^{-7} \text{ mbar}$

Figure 2.2: HASO™ EUV wavefront sensor. Technical specifications

## 2.2 Optimization of soft and hard X-ray focusing systems

The Hartmann wavefront sensor technique has been successfully applied in the soft X-ray range using synchrotron, FEL and HHG sources [5, 34, 59].

Previous results at the HH imaging beamline at CEA-Saclay, have successfully demonstrated the use of a HASO wavefront sensor (designed to work with soft X-ray sources) as a real time technique to improve the focusing of an off axis parabola [34]. In this case (imaging beamline Fig. 3.2 at CEA-Saclay) the beam path from the harmonic source (output of the gas cell) to the sample in the imaging chamber (Fig.3.3) is formed by an IR-antireflective mirror, 2 thin aluminum filters and an off axis parabola with a multilayer coating designed to select one harmonic component. A scheme of the wavefront sensing of either the direct HHG beam or the beam reflected by our focusing optics for coherent diffractive imaging experiment is shown in Fig. 2.3.

Several HHG parameters have been explored to optimize the harmonic flux and the beam wavefront RMS value. The wavefront RMS value describes how the measured wavefront is distorted compared to a plane wave. According to the Maréchal's criterion, a beam is diffraction-limited at a given wavelength  $\lambda$  when the aberrant wavefront amplitude is lower than  $\lambda/14$  rms. As we assume a plane wave illumination in CDI, if the beam is far away from a plane wave, then the reconstruction will not correctly represent the sample transmittance but the ensemble exit wave (sample transmittance + incident wave). However, we can still extract the sample transmittance if we know the incident wave, a priori, which requires a measurement of the incident wavefront.

Practically, if the beam is not stable (aberrations change from shot to shot), simultaneous measurements of the incident wave and the sample diffraction pattern will be required. If

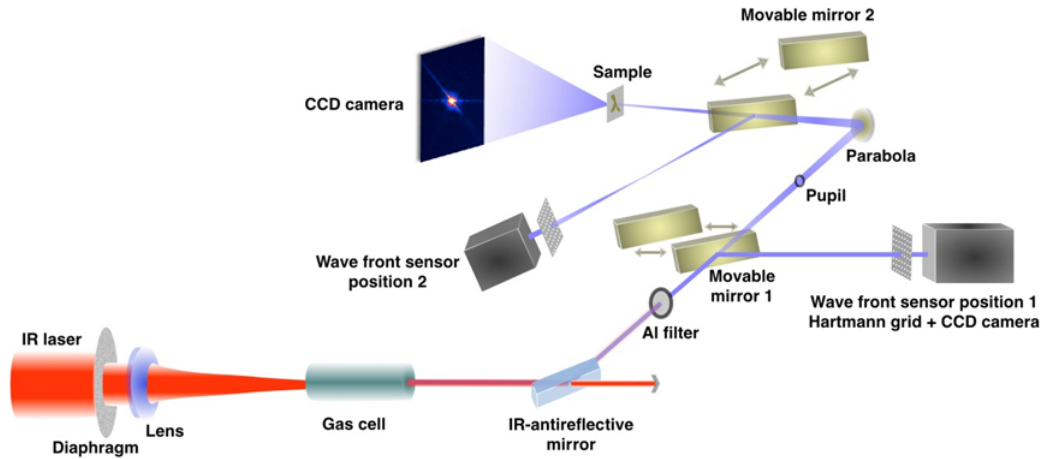


Figure 2.3: Scheme of the wavefront optimization experiment setup. 1) HHG optimization configuration: Movable mirror 1 (multilayer plane mirror) is in and the wavefront sensor is located at position 1 to measure the direct harmonics beam. 2) Focusing optimization configuration: Movable mirror 1 is out and mirror 2 is in; the wavefront sensor is located at position 2 to measure the harmonic beam focused by the parabola. 3) Diffraction configuration: Two movable mirrors are out and no wavefront sensor. The sample is located at the focus of the parabola and the XUV camera detects the diffraction pattern (far field interference of the slits exit waves).[33]

the beam is stable these measurements can be achieved in different shots, the relative position of the beam when hitting the sample should be known for extracting correctly the sample transmittance information. The wavefront has been optimized down to the RMS error  $\lambda/6$  which gives also a maximized harmonic flux reaching 250 nanojoule per shot for H25 at the exit of the source. These conditions are used for the single shot coherence measurement and stereo-imaging experiments. Here we will focus more on the optimization of the beam transport and focus. Indeed, high aberrations can be induced in the incoming soft X-ray beam by a misalignment of the off axis parabola. The parabola position is motorized by a translation stage, rotation stages and goniometers (Fig. 3.3) allowing an accurate adjustment to optimize the alignment. A first alignment is made using the IR beam as reference. Then, the wavefront sensor was used to improve the off axis parabola alignment directly on the harmonic beam (H25) [33]. The HASO wavefront sensor was located behind the focus of the parabolic mirror to characterize the harmonic focal spot as a function of the off axis parabola position.

The HASO software uses the measurements to reconstruct and visualize the wavefront in real time. The measurement of the RMS error with respect to a spherical wavefront of reference was used as a parameter to improve the alignment of the off axis parabola. The results show a reduction of the RMS error from  $0.326\lambda$  ( $\sim \lambda/3$ ) up to  $0.154\lambda$  ( $\sim \lambda/6$ ) Fig.(2.4)

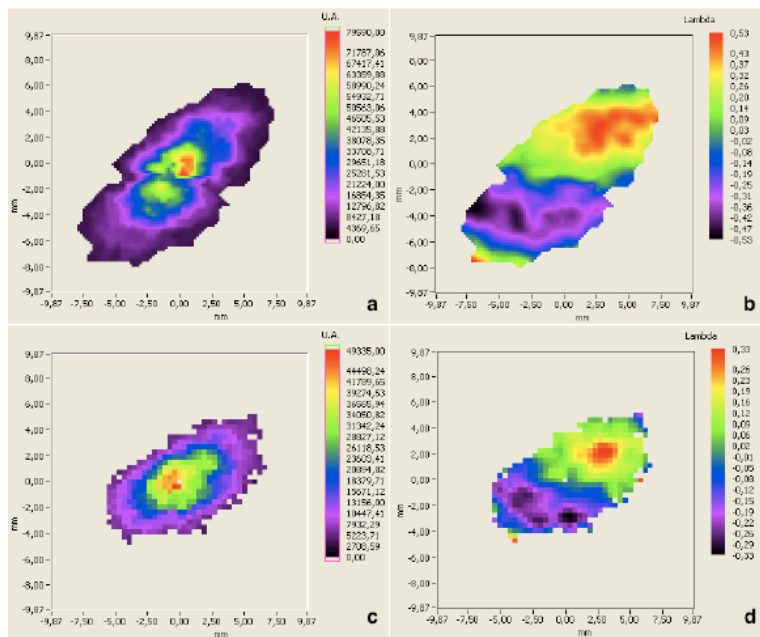


Figure 2.4: HASO measurements of H25 focal spot after the focusing system. After initial alignment with the IR beam (a) intensity (b) phase, and with finely tuned parabola by following the HASO measurements (c) intensity and (d) phase. Figure taken from [33].

[33]. The coma aberration present in the wavefront (Fig. 2.4 (b)) was reduced but not completely removed. However the reconstruction of the intensity spot at the focal plane shows an important improvement before and after the RMS error reduction (Fig. 2.5). The focal size (at  $1/e^2$ ) was optimized from  $7.8 \mu\text{m}$  to  $5 \mu\text{m}$ . A smaller focal spot generates an increase in the flux of photons on the sample, an important factor for lensless imaging.

The evolution of the focal spot through the beam propagation direction ( $z$ ) shows a slower change around the focal plane, with respect to the one presented without the final alignment. In this way, the optimized circular spot size is preserved in a zone of  $\pm 0.5 \text{ mm}$  around the focal plane. Once the alignment of the off axis parabola has been improved, the IR beam can be used as a reference for the daily alignment, considering that the parabola position is fixed now in a position that corresponds to a low aberration configuration.

Thanks to the expertise acquired in wavefront characterization of soft X-ray sources we decided to explore different applications of wavefront sensing with FEL sources. For this, a new wavefront sensor HASO soft X-ray was designed (by Imagine Optic). The specifications were defined projecting the use of the WFS with a broad soft X-ray spectrum. The determination of the characteristics needed was the result of a collaboration of our group with Jacek Krzywinski and John Bozek from the Atomic, Molecular and Optical science beamline (AMO) station at LCLS and Philippe Zeitoun at LOA (Laboratoire d'Optique Appliquée-ENSTA) (France). The specifications demanded from Imagine Optic included a broad spectral range (30 eV - 400 eV) and a small wavefront measurement accuracy (rms)

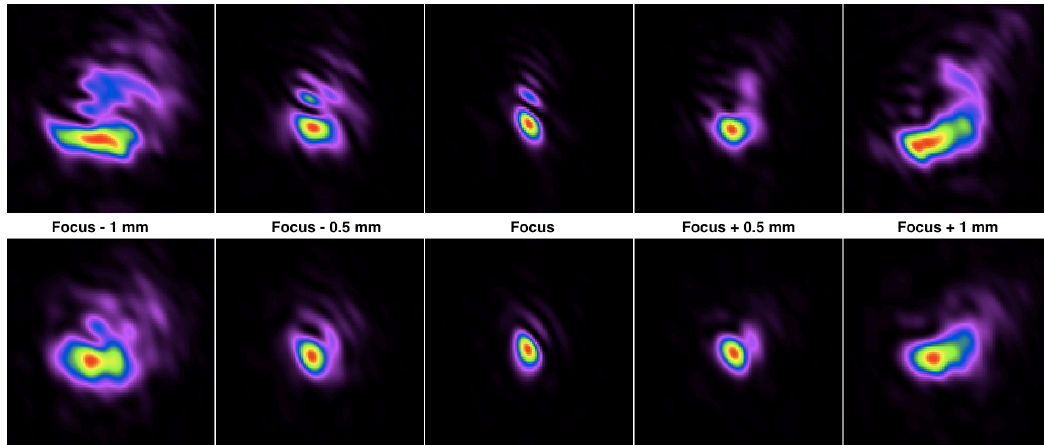


Figure 2.5: Evolution of H25 spatial profile around the focus of the parabola. Top line, before fine alignment. Bottom line, after fine alignment using HASO. The spatial profile was calculated by back propagating the intensity and phase HASO measurements. Figure taken from [33].

of  $\lambda/17$  at 1 nm (needed for the short wavelengths at LCLS). These two parameters determined the main constraints for the design of the WFS. To achieve the characteristics needed, a compromise was made in the design and only diverging wavefronts can be measured with HASO soft X-ray (the previous version HASO works in converging and diverging regime).

### 2.2.1 Experimental results at AMO-LCLS

This experiment was designed to improve the K-B focusing system at the AMO end-station using the wavefront sensor technique. The K-B focusing system is made of two hard X-ray elliptical mirrors (Fig. 2.6). The mirrors configuration can be controlled by bending each one of the mirrors or by rotating the whole K-B system and changing the horizontal with respect to the beam direction. High aberrations can be induced by a misalignment between the two mirrors. The alignment is usually made monitoring the beam size calculated from a set of spot sizes on a polymethyl methacrylate PMMA membrane due to ablation resulting from the interaction with the X-ray at different positions and energies [10]. This method is time consuming and does not allow a diagnostic in real time. The HASO soft X-ray wavefront sensor was used as a real time technique of alignment. The wavefront sensor was placed in the SXR hutch at  $\sim 6.5$  m from the K-B system (Fig. 2.7). The X-ray photon energy was set at 380 eV, corresponding to a wavelength of  $\lambda = 3.26$  nm, with an electron bunch charge of 150 pC under-compression.

After an initial alignment of the K-B system using the imprints technique, the X-ray beam presented a remaining coma aberration (Fig. 2.8 (a)). The goal then was to reduce the aberration using the HASO soft X-ray wavefront sensor. For this, the aberration coeffi-

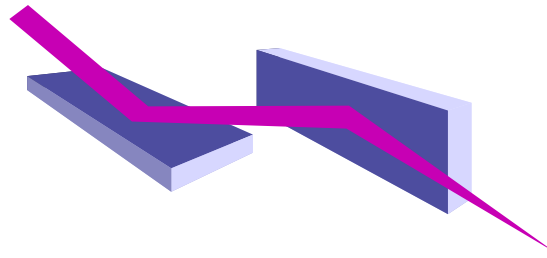


Figure 2.6: Sketch of a K-B focusing system. It is composed of two mirrors. Each mirror focuses separately the beam in the vertical and horizontal directions.

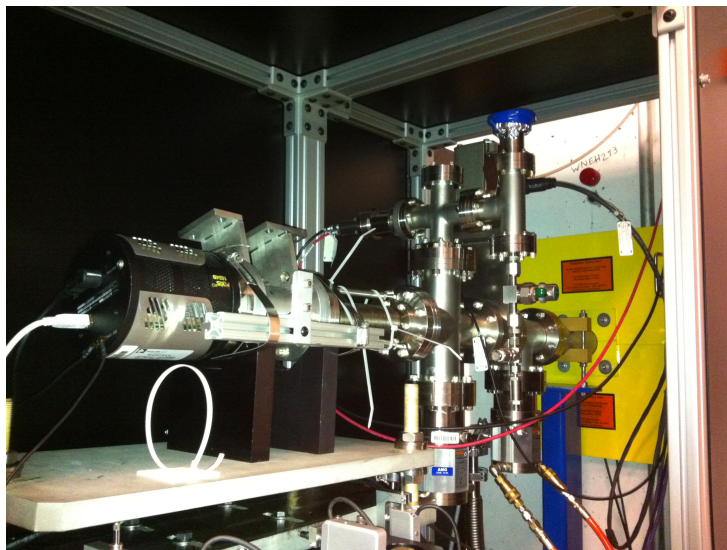


Figure 2.7: Experimental setup during the wavefront sensing campaign at the AMO end-station. The sensor was mounted at the SXR hutch at  $\sim 6.5\text{m}$  from the K-B system.

coefficients were followed in real time in terms of the K-B mirrors position. The coefficients were calculated by the HASO software using a modal reconstruction via Legendre polynomials. The acquisitions were made using an accumulation of the signal during 1s. We should notice that the beam was not completely captured by the sensor (Fig. 2.9). It means that the aberration coefficients calculated corresponds to the aberration of the part of the beam captured. As this may induce errors in the beam spot calculation by retro-propagation, only the aberration coefficients were used to follow the changes induced by the different K-B mirrors positions.

The wavefront at the initial position (after the alignment with the ablation technique) presented clearly a third order aberration (Fig. 2.10 (a)) and an astigmatism at  $45^\circ$  (Fig. 2.10 (b)). To improve the coma we changed the bending position of the mirrors. The astigmatism was changed by rotating the whole K-B system. After optimization of the K-B mirror positions, following in real time the values of the aberration coefficients, the coma and

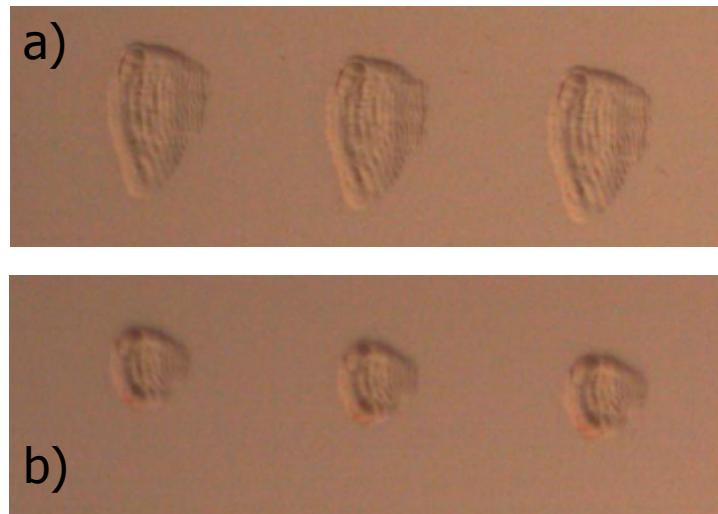


Figure 2.8: Imprints on the PMMA membrane a) After aligning the K-B system using the ablation technique b) After a final alignment with the HASO.

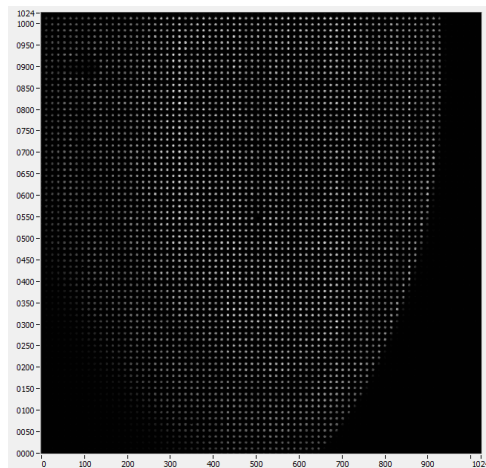


Figure 2.9: CCD signal captured by the HASO after 1s of acquisition of the FEL beam focused by the K-B system in the initial configuration.



astigmatism coefficients were reduced. In this way, the total RMS was improved from  $5.4\lambda$  down to  $4.8\lambda$ . The reduction in the aberration coefficients improves the focal spot. This improvement was also evident in the PMMA imprints taken after the final alignment (Fig. 2.8 (b)). A remaining aberration was always present, which is due to a carbon deposition on the K-B mirrors.

In conclusion, the soft X-ray wavefront sensor has been used to optimize the focusing of the LCLS FEL beam at the AMO end station. Using the wavefront measurement of the FEL beam after the focus, the KB system has been adjusted in real time to correct the focal spot of the soft X-ray beam. The HASO wavefront sensor has been a very useful tool. The software was able to back propagate the beam for a direct visualization of the focal spot. The instrument has shown to be very versatile and easy to implement.

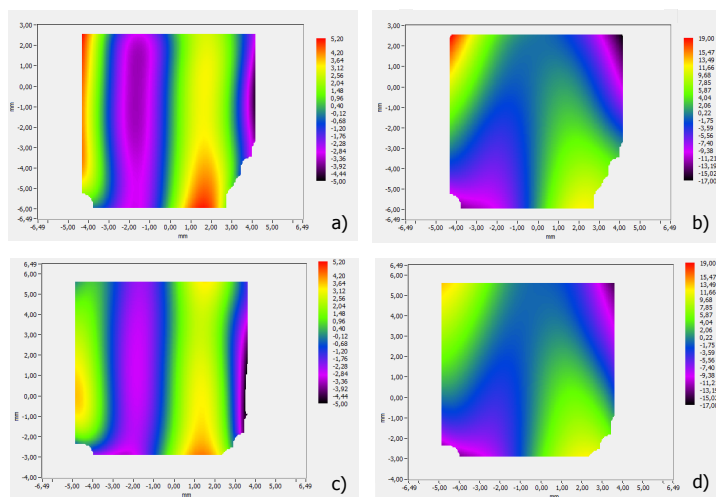


Figure 2.10: Wavefront measured by the HASO wavefront sensor and calculated via Legendre polynomials fit. At the initial position a) The effect of the astigmatism at  $45^\circ$  has been filtered out, a coma aberration is present b) The whole aberration (astigmatism and coma not removed). After the final alignment c) without astigmatism factor. d) The whole aberration.

## 2.2.2 Experimental results at FERMI ELETTRA

The wavefront sensing experimental campaign at FERMI@ELETTRA had two main objectives. To characterize the FEL wavefront arriving to the different beamlines and to improve the K-B focusing system at the imaging beamline DiProl. FERMI@ELETTRA is the first seeded EUV-SXR FEL source. The use of external laser seeding together with a harmonic upshift scheme to obtain short wavelengths gives FERMI@Elettra the capability of producing high-quality, transversely and longitudinally coherent photon pulses in the soft X-ray region with short pulses ( $\tau \sim 10 - 100$  fs). This capability, together with the possibility of temporal synchronization to external lasers and control of the output photon polariza-

tion, opens new experimental opportunities that are not achievable with currently available FELs. The characterization of the FEL wavefront allows studying its relation with the different generation parameters. That is why the first part of the experimental campaign was focused on the X-ray wavefront characterization.

The wavefront sensor was placed at the main line of the FEL, before arriving to the different beamlines (Fig. 2.11). At that position, the X-ray beam has been reflected only by one mirror. The FEL beam was generated with a seed beam of  $\lambda = 261.1$  nm with circular polarization. The results of the wavefront measurements with the FEL emission centered at 20 nm (H13) for two different undulator tuning conditions are presented in Fig. 2.12. It can be clearly seen in the intensity reconstruction of the beam (Fig. 2.12 (a) and (c)) that two different modes were generated. The first mode (Fig. 2.12 (a)-(b)) presents a Gaussian transverse mode in amplitude, corresponding to a conventional FEL emission mode. On the other hand, the second mode generated (Fig. 2.12 (c)-(d)) represents a particular emission mode. The transverse mode in amplitude is composed by an annular region which is attributed to an emission composed by two main modes, a nearly-Gaussian and an annular one. This annular FEL emission is related to a mismatch of the undulator tuning. In the undulator, the full resonant condition is [4].

$$\lambda_R = \frac{\lambda_0}{2\gamma^2} \left( 1 + \frac{K^2}{2} + \gamma^2 \theta^2 \right), \quad (2.2)$$

where  $\lambda_R$  is the resonance wavelength,  $K$  is the undulator deflection parameter,  $\lambda_0$  is the magnetic field periodicity,  $\gamma$  the electrons energy and  $\theta$  the radiation angle emission. From Eq. 2.2 we can see that if  $K$  is not well tuned, the emission will be done off-axis with respect to the resonance condition. The effect in the phase of the FEL emission (Fig. 2.12 (b)) is given by a phase jump in the area of the annular emission. By optimizing the FEL emission it was possible to remove the annular mode improving the RMS of the overall wavefront from  $\lambda/6$  down up to  $\lambda/7$ .

This result shows how the wavefront analysis on the direct FEL radiation is useful to study the generation conditions. A perspective from the results presented here is to study the FEL wavefront as a function of the seed. The relevance of such a study is to understand the effect of the seed on the spectra-temporal properties on the electron bunch and thus on the FEL emission. However, the experimental result showed no conclusive results because the signal was strongly affected by the filters quality. Indeed, the filter exhibits an irregular thickness which induces phase jumps. Even taking this as a reference was not enough to get slight changes of the FEL wavefront. Not only the FEL signal but also the multiple harmonics were detected. After few attempts, it has been finally impossible to isolate and follow clearly the FEL signal. Another experimental campaign with more homogeneous aluminum filter is scheduled at FERMI.



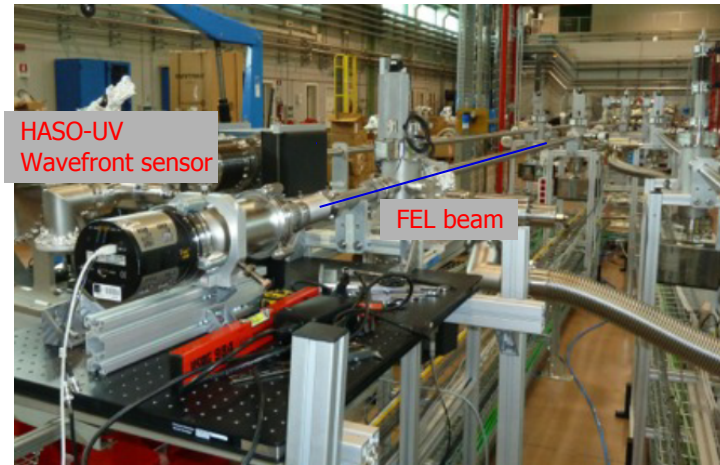


Figure 2.11: Wavefront measurement setup at the main beam line of the seeded FEL at FERMI@Elettra. [71]

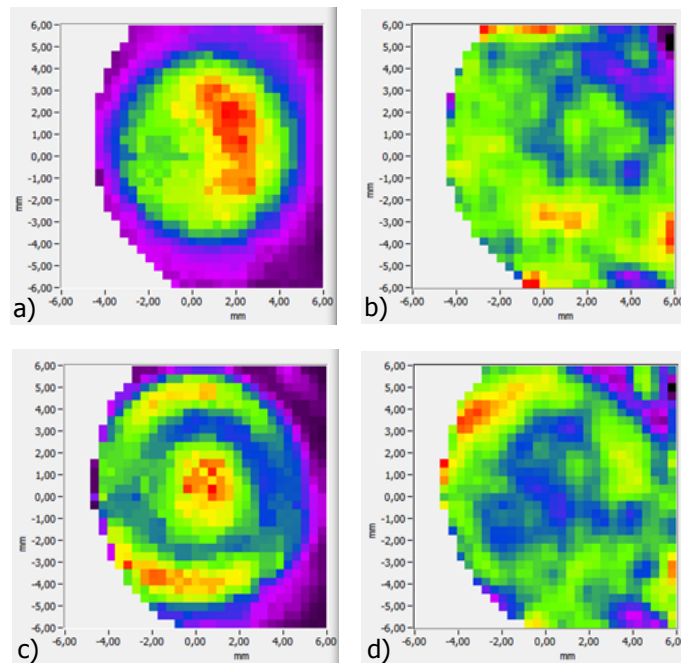


Figure 2.12: Measurement of FEL emission centered at  $\lambda = 20$  nm by using the HASO-UV wavefront sensor in a conventional mode of FEL emission a) Intensity profile, b) wavefront, and a particular two modes FEL emission c) Intensity profile, d) wavefront.

The second goal of this experimental campaign was to improve the K-B focusing system at the imaging beamline DiProI. In this case, the wavefront sensor was placed outside of the DiProI chamber, at 1.25 m from the focusing plane (Fig. 2.13). The FEL was tuned at  $\lambda = 32$ nm.

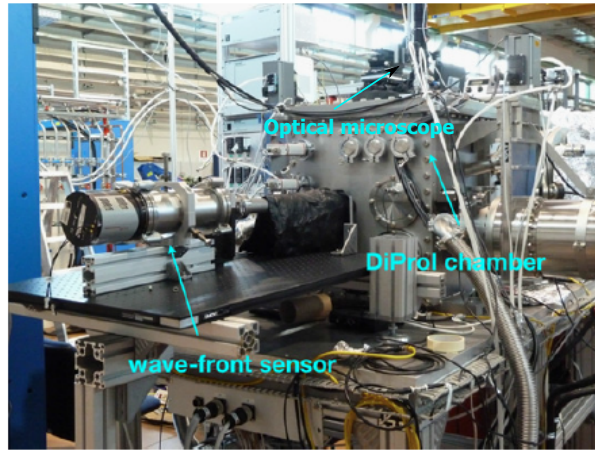


Figure 2.13: Experimental wavefront measurement setup to improve the K-B focusing system at DiProI beamline at FERMI@Elettra [71]

Three different techniques to monitor the focal spot were used to perform the alignment of the K-B system. An initial alignment was made following the focal spot size measured on a Phosphorus screen ( $25\ \mu\text{m}$  Manganese activated Zinc Silicate Phosphor, commercially referred to as P1). For this measurement an integration time of 2s (20 pulses) was used. A parallel diagnostic was made using the imprints generated on a PMMA membrane in single shot configuration. A final alignment was achieved using the HASO wavefront sensor.

To reduce the time used for the diagnostic using the Phosphorus screen and the imprints techniques, an optical microscope was installed on top of the DiProI chamber. It allows scanning the Phosphorus screen or the PMMA membrane directly into the chamber. The smallest focal spot achieved after the initial alignment presented a mismatch between the two techniques of scan (PMMA imprints and Phosphorus screen). The focal spot size measured from the Phosphorus screen is  $40\ \mu\text{m} \times 42\ \mu\text{m}$  (Fig. 2.14) and the one measured from the PMMA imprints is  $26\ \mu\text{m} \times 15\ \mu\text{m}$  (Fig. 2.15). In fact, the spot size measured with the PMMA technique represents an estimate because the measurements do not take into account the FEL beam energy effect [10]. On the other hand, the focus spot size measured with the Phosphorus screen can be affected by saturation effects.

A final alignment was made using the Hartmann wavefront sensor. The intensity (Fig. 2.16 (a)) presented a rectangular shape induced by the FEL generation conditions. The wavefront, calculated using a Zernike polynomial fit, presents clearly a third order aberration (coma) in the horizontal direction (Fig. 2.16 (b)). The initial RMS wavefront error was  $0.81\lambda$ . Using the intensity and wavefront calculated for the whole beam, the focal spot was calculated by retro propagation with the HASO software (Fig. 2.17). The effect of the coma aberration is also found in the horizontal profile of the focal spot reconstruction (Fig. 2.16 (b)).

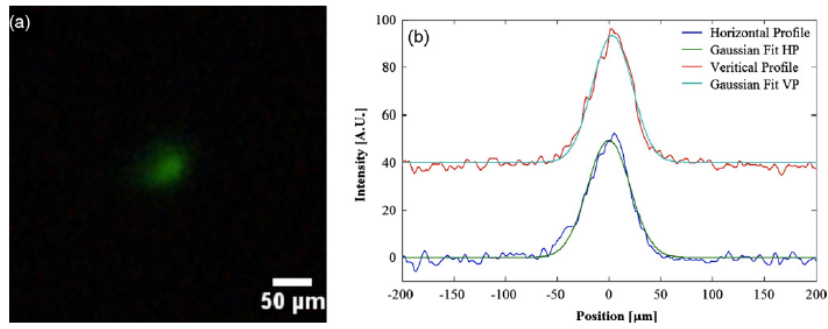


Figure 2.14: Focal spot on the Phosphorus-screen after the initial alignment, using an accumulation of 2 seconds (20 shots). a) Image on the Phosphorus-screen. b) horizontal (blue) and vertical (red) profile with . The spot size, calculated from the Gaussian fit, is  $40 \mu\text{m} \times 42 \mu\text{m}$  [71].

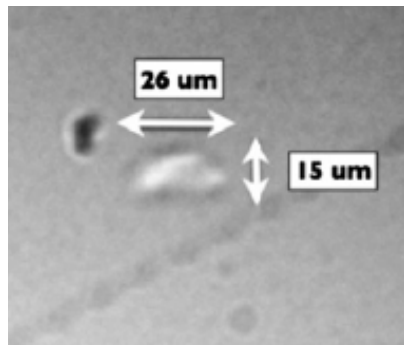


Figure 2.15: Imprints of the FEL on a PMMA membrane in single shot. The spot size estimated from this imprint is  $26 \mu\text{m} \times 15 \mu\text{m}$  [71].

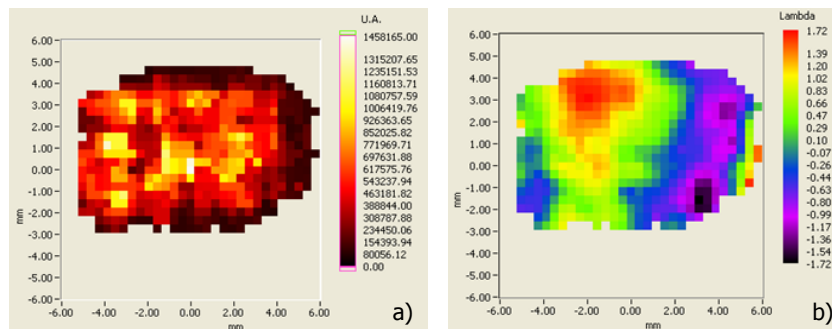


Figure 2.16: Wavefront measurement using the HASO after the initial alignment. a) Intensity distribution of the beam at the plane of the wavefront sensor. b) Wavefront calculated using a Zernike polynomial fit.

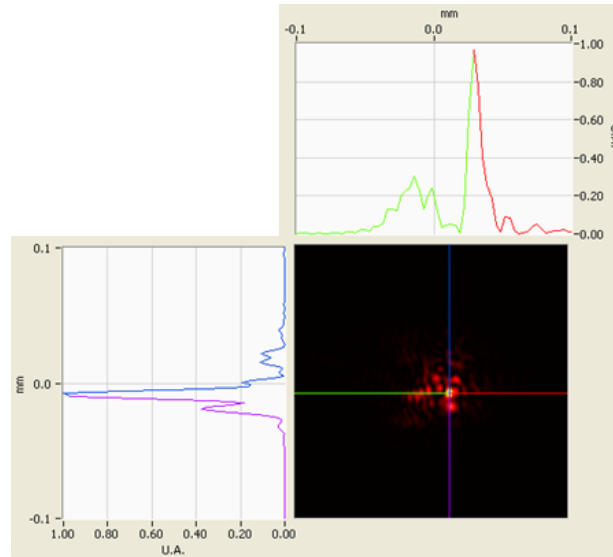


Figure 2.17: Focal spot after the initial alignment calculated by retro-propagation from intensity and wavefront calculated in Fig. 2.16.

By following the aberration coefficients, the third order aberration was reduced changing the bending condition of the mirrors. The total wavefront RMS error was reduced from  $0.81\lambda$  down to  $0.34\lambda$ . The final wavefront and focal spot reconstruction are presented in Fig. 2.18. The aberration corrections reached thanks to the Hartmann wavefront sensor technique, allowed a final focal spot size of  $5\ \mu\text{m} \times 8\ \mu\text{m}$ . This size is very close to the limit of the mechanical system calculated with the WISE code for ideal mirrors (based on the physical optics approach) and measured during the mirror characterization with the Long Trace Profiler (LTP) (Fig. 2.19) [71].

In conclusion, this result proved the advantages of the Hartmann wavefront sensing technique against the traditional methods of alignment (imprints and Phosphorus-screen). Usually the technique of PMMA imprints is used. It is a time consuming technique. Its sensitivity to aberrations is moreover reduced because of a low resolution due to the ablation processes. Using the HASO and its beam back propagation software we were able to monitor the system aberrations in real time. The results evidenced remaining aberrations after focusing with the "Imprints" method. With the HASO, we have obtained a significant improvement of the wavefront error down to  $0.34\lambda$ . As a consequence the focal spot size of K-B focusing system at DiProI beamline has reached the limitation given by the instrument and the beam properties.

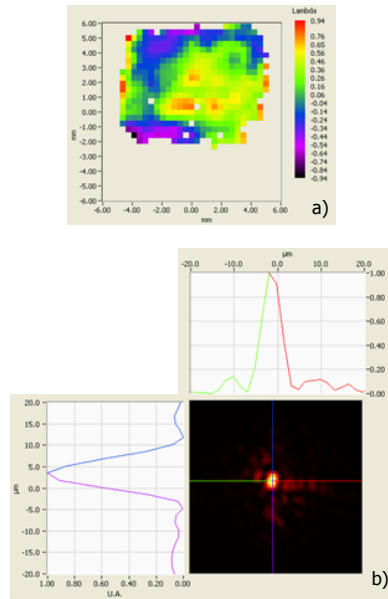


Figure 2.18: Hartmann wavefront sensing of the beam after the final alignment. a) wavefront with a RMS error of  $0.34\lambda$ . b) Focus beam spot calculated by retro-propagation. The beam size is  $5 \mu\text{m} \times 8 \mu\text{m}$ .

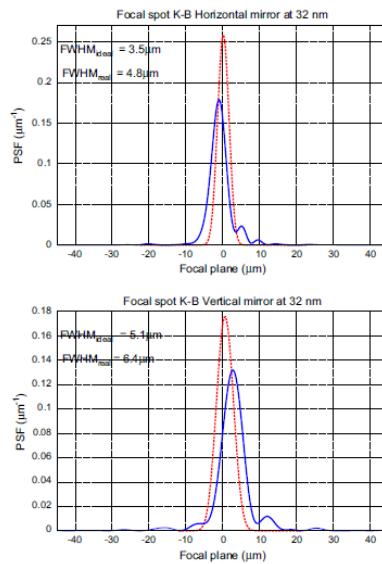


Figure 2.19: Focal spot simulations calculated with the WISE code of ideal mirrors (red dotted lines) and of the best profiles obtained with the LTP characterization (blue line) of the two K-B mirrors. In the best focus, the vertical mirror generates a spot size of  $5.1 \mu\text{m}$  for the ideal case (WISE code) and  $6.4 \mu\text{m}$  in the real case (LTP characterization); the horizontal mirror generates  $3.5 \mu\text{m}$  in the ideal case and  $4.8 \mu\text{m}$  in the real case. [71]

### 2.3 Sensing FEL plasma dynamics via wavefront measurements

The solid density photo-ionized plasma created by the X-ray FEL at LCLS is highly significant in Inertial Fusion, astrophysics and "probing-before-destroying" as used in coherent diffractive imaging of biological systems at XFELs. However, the mechanisms behind the formation of plasmas created by X-ray-solid interaction is not completely understood. Recent results [89] highlighted the importance of electron ion collisions in the creation of such plasmas, yet the timescale on which the XFEL laser energy is transferred to the ion system from solid state is still not well known.

The main objective of this experimental campaign was to understand the mechanisms behind the formation of plasmas created by X-ray laser-solid interaction. The material state is inherently different from that of optical laser generated plasma, in that the energy deposition has a high uniformity in the direction of propagation, and the process of photon absorption occurs in a distinct manner, i.e., by photo-ionization of the inner shell electrons. The transfer of the X-ray photon energy to the solid sample is first made via a photo-absorption process. The predominant process will be K-shell photo-ionization for Al and Ti creating a hole, or a double K shell hole state [25]. The holes are filled via the dual mechanisms of Auger (non-radiative), and radiative (fluorescent) decay. The initial decay occurs on the order of a fs and the Auger cascade will then transfer energy to the outer electrons on a timescale of  $\sim 100$  fs. The ions are heated throughout the process, but minimal hydrodynamic motion is thought to occur within the first 1 ps.

To date, the methods proposed to characterize X-ray laser-produced plasma are not temporally resolved within the duration of the electron-ion heating process. One of the most widely used diagnostics is K-shell emission spectroscopy, which reveals fluorescence signatures that, since the diagnostic is time-integrated, can only give insight into the evolution of the processes through deconvolution of several spectra taken at different pulse durations. Other passive diagnostics include XUV emission after the pulse has sufficiently heated the plasma, which are also integrated over the entire heating process. To have the temporal resolution, the use of the IR laser as a probe provides sufficient spatial resolution but only of the expanding reflecting surfaces, with indirect insight into the atomic physics processes. Transmission probing of a close to solid density plasma requires wavelengths in the soft X-ray range or below. In our case, we probed the X-ray produced plasma with a coherent soft X-ray source generated by the high harmonic generation process. In this way, we used a XFEL pump and soft X-ray probe configuration to follow the plasma dynamics. This is the first time that such an experiment is realized. Short pulse durations of HH beams (attosecond) make the new HH source a promising tool for probing dense plasmas produced at the LCLS with unprecedented temporal resolution, and open the door for future attosecond metrology with the LCLS.

The measurement of the optical properties as a function of time allows studying the evo-

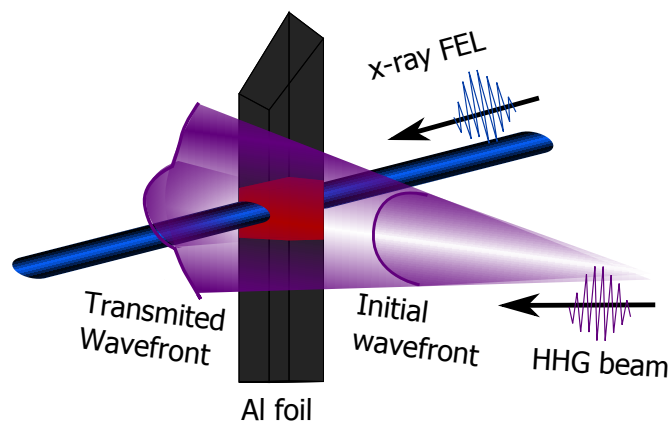


Figure 2.20: Sketch of soft X-ray HH wavefront changes induced by the refractive index variations generated with the irradiation of the Al foil with the X-ray FEL

lution of the state of the electrons. In this way, the plasma formation by the X-ray solid interaction can be followed in time by recording the soft X-ray wavefront modulations through solid-density plasmas of known energy density. The part of the soft X-ray radiation that propagates through the sample is either absorbed or scattered in the forward direction, undergoing a change in the wavefront (Fig. 2.20). This phase variation of the soft X-ray field is generated by a change in the complex refractive index ( $n$ ). The refractive index is determined by the density, temperature and electronic structure of the material. In this way, with the measurement of  $n$  as a function of the time delays between the XFEL pump and the soft X-ray probe, we can access to the time evolution of the state of the electrons. This gives a unique insight into the timescales and nature of the heating process.

In this section we present the preliminary results on soft X-ray wavefront variations at the  $ps$  scale taken during the experimental campaign at the Matter in Extreme Conditions (MEC) beamline at LCLS. Parallel measurements of the plasma emission using an emission spectrometer and the soft X-ray transmission were done during the experimental campaign. The transmission measurements allow following the temporal changes on the refractive index that can be compared with the temporal variations detected by wavefront sensing.

This campaign was made in collaboration with the group for lasers and plasmas GoLP from the Instituto de Plasmas e Fusão Nuclear-Laboratório Associado at the Instituto Superior Técnico, Lisboa, Portugal and the group of Philippe Zeitoun at LOA-ENSTA.

The sketch of the XFEL pump and the soft X-ray probe setup used during the experimental campaign is presented in Fig. 2.21. Simple point projection geometry, and multiple-shot integration were considered, allowing to follow plasma hydrodynamic evolution in a  $ps$  regime. The temporal range of the evolution expected from simulations is over 10ps. This makes suitable the soft X-ray shot accumulation even with 250 fs jitter.



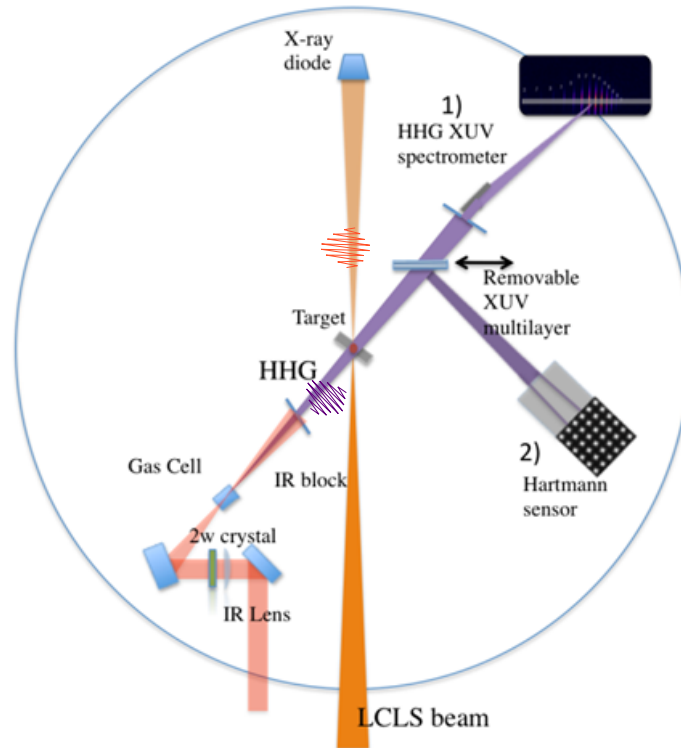


Figure 2.21: Sketch of X-ray FEL pump - soft X-ray HHG probe. Soft X-ray wavefront variations are measured with the HASO wavefront sensor. Parallel measurements of transmission and plasma emission are made with an XUV spectrometer and X-ray diode respectively. [48]

The LCLS beam is focused onto thin foils of Al and Ti with focal spots from 10 to 20  $\mu\text{m}$ . The targets thicknesses are chosen so that XUV transmission is detected even for cold material. We produce a soft X-ray probe beam, measure its transmitted spectrum through the dense plasma, and measure its refraction at a selected wavelength using a HASO wavefront sensor (WFS).

As this was the first time that such an experiment (XFEL pump and soft X-ray probe) was done, a preliminary optimization of the soft X-ray generation via HH process was made in collaboration with the MEC beamline scientists and the laser group at LCLS [48]. HHG have been optimized off-line at the MEC end station using moderate intensity ( $\sim 10^{14} \text{ Wcm}^{-2}$ ) laser-gas interaction. HHG photon energies up to  $\sim 45 \text{ eV}$  for Ar have been used. Optimal conditions for emission (varying IR lens position, aperture and gas density) have been found during that first campaign. 1 nJ/HHG/pulse from 42 eV has been estimated, for which HHG emission is 3 – 4 orders of magnitude above plasma self-emission due to the low divergence of the HHG beam. The wavefront of the HHG emission was monitored with



HASO wavefront sensor, as an additional parameter of HHG optimization, by insertion of a XUV multilayer that selects H25.

During the plasma dynamics experimental campaign the HHG source was generated by the IR laser beam (40 fs,  $\leq 5$  mJ, @800 nm ) focused ( $f = 75$  cm) on a gas cell (1.4 cm length) filled with Argon at 32mbar. After filtering out the IR beam that propagates with the HH beam, the H25 ( $\lambda = 32$  nm) was focused with an off axis parabolic mirror that has a multilayer coating designed to do the spectral selection of H25. The soft X-ray HH wavefront of the transmitted field through the target was measured with the HASO soft X-ray wavefront sensor. Thanks to the temporal synchronization of the HHG process with the IR beam used for the generation, the temporal delay between the pump X-ray FEL (55 fs, 2.5 mJ @3 keV) and H25 is controlled by changing the XFEL/IR delay.

For each target a reference phase was taken with the wavefront measurements without X-ray FEL radiation (cold target). A second shot with the X-ray FEL pump was taken to measure the wavefront variation with respect to the cold target. A third shot, after the target destruction due to the X-ray FEL irradiation, was used to determine the zone where the plasma has been generated. This zone can be recognized by the diffraction generated through the hole on the target produced by the X-ray FEL beam. The results of the wavefront measurements with the cold target wavefront as reference are shown in Fig. 2.22. The phase variations were calculated taking the average phase over the zone where the plasma was created. Fig. 2.23 presents the preliminary results using an Al target of 300 nm thickness. Those preliminary results (experimental error induced by noise in wavefront measurements) present a variation in time of the phase change of the ps order (0 – 15 ps). The temporal scale of the refraction variation are consistent with the results found via transmission measurements (Fig. 2.24). The analysis of the data is still undergoing so that final conclusion cannot be given while writing this manuscript.

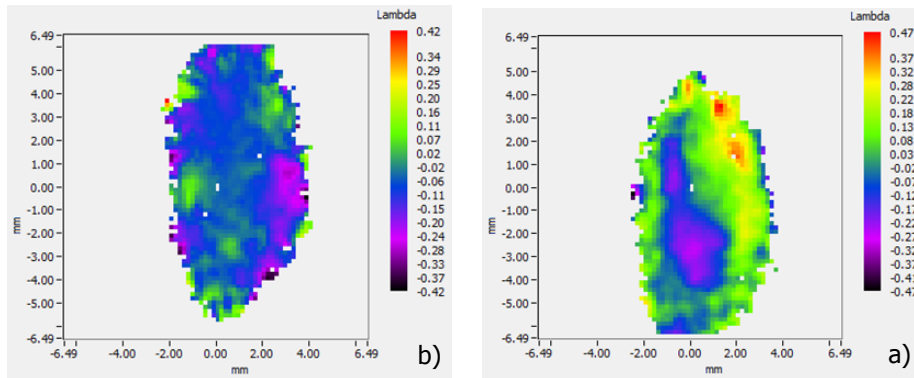


Figure 2.22: Wavefront reconstruction of the soft X-ray that goes through the Al (300 nm) target after being irradiated with the XFEL beam. a) Cold target. b) Temporal delay  $\tau = 5\text{ps}$ .

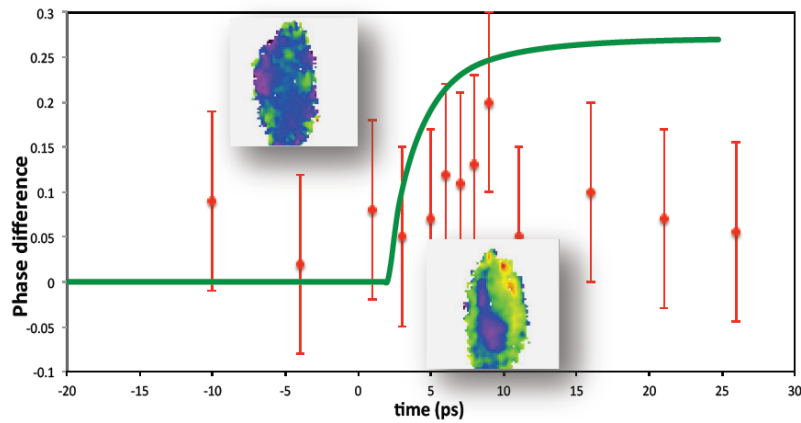


Figure 2.23: Phase variation on the soft X-ray HH beam induced by the changes on the refractive index of the solid density plasma creates by the X-ray FEL in a 300 nm thick Al foil (red points). Simulation of the phase variation averaged over  $2\ \mu\text{m}$  area (green line) calculated using the TTM solutions + RPA. Wavefront reconstruction with cold target as reference (inset). Preliminary results

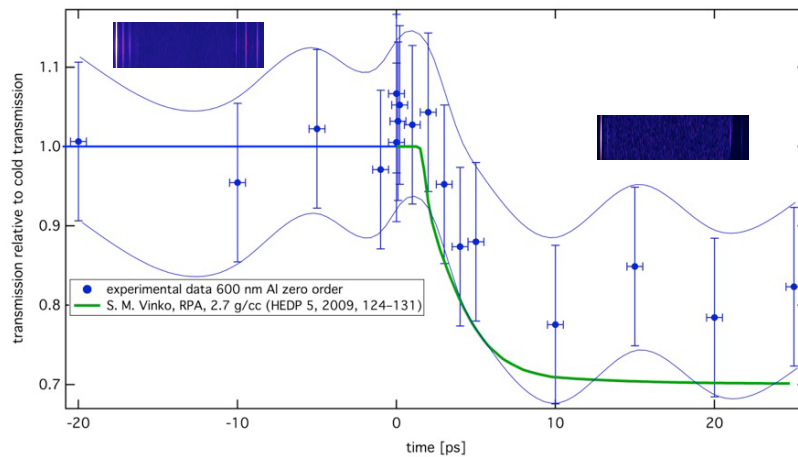


Figure 2.24: Soft X-ray transmission measurements relative to cold solid with an Al (600 nm) target (blue points). Simulations with S. M. Vinko. RPA model, 2.7 g/cc (HEPD 5, 2009, 124 – 131) (green line). Image taken from G. Williams, et. al. paper in preparation.

## 2.4 Conclusions

In this chapter, experimental results of the wavefront sensing in the soft X-ray range have been presented. Using a commercial Hartmann wavefront sensor the property of the HHG beam and its focus were studied. A sub- $\mu\text{J}$  harmonic source (few  $10^{10}$  photons per shot for the 25<sup>th</sup> harmonic,  $\lambda = 32$  nm) is generated at the output of the gas cell, with a wavefront RMS of  $\lambda/9$  before parabola and  $\lambda/6$  after focusing, which is close to two times the diffraction-limited ( $\lambda/14$ ). Indeed, the aberrations induced by our focusing system were reduced from an RMS error of  $\sim \lambda/3$  up to  $\sim \lambda/6$ .

The combination of intense harmonic flux and good wavefront quality promises high-quality diffraction patterns for coherent imaging. The campaign of harmonic wavefront measurements resulting in an optimized HHG and focusing allows daily reproducible conditions. Different generating parameters have been studied in this campaign. The HHG focal spot was reduced, improving in this way the flux of photons in an area of  $5 \mu\text{m}^2$  that is the used to perform coherent imaging experiments.

This technique of focal spot optimization was then successfully applied to FEL facilities. After the use of the usual focusing technique via PMMA imprints, we reduced the remaining aberrations induced by the K-B focusing system. By following the wavefront measured with the soft X-ray Hartmann sensor as a feedback, the K-B mirrors were bended to reduce the aberrations. At DiProI beamline at FERMI@Elettra the focal spot at  $\lambda = 32$  nm was optimized from  $26 \mu\text{m} \times 15 \mu\text{m}$  down to  $5 \mu\text{m} \times 8 \mu\text{m}$  which is very close to the limit of the mechanical system.

Direct beam X-ray FEL wavefront sensing at FERMI@Elettra evidenced the generation of a particular X-ray mode composed by two main modes, a nearly-Gaussian central peak and an annular one. The generation process of such a mode is well known [49] but there are different mechanisms to generate it. This result opens the perspective of studying the different generation mechanisms by following the wavefront.

At the AMO-LCLS end-station a visible reduction of the coma aberration was detected after the alignment with the wavefront sensor. The total RMS wavefront error was reduced from  $5.4\lambda$  down to  $4.8\lambda$  with  $\lambda = 2.26$  nm. The remaining aberration was induced by a carbon deposition on the K-B system.

At LCLS, we have demonstrated, that combining powerful XFEL laser pulses with HHG from an optical laser, enables a flexible pump-probe scheme which can be used as an ultra-fast diagnostic of the optical and structural properties of a dense plasma. The possibility of following plasma dynamics via wavefront sensing allows studying the plasma dynamics generated by XFEL pulses. The use of a short (60 fs) XFEL pulse to heat a solid target (aluminum, titanium) allows to the heating of the electrons and ions to be naturally separated in time, which are individually complex processes. Additionally to these measurements, absorption measurements of the harmonics were performed. The results show the effect of the heated electron distribution and crystal lattice order over the relevant timescales (up to 25 ps), and that the increase in opacity in the wavelength range used in this study is nearly entirely due to loss of crystal order causing increased absorption up to a few picoseconds, and that the heated electron distribution has a relatively minor effect.



---

## 3D STEREO SETUP IMAGING WITH HARMONIC SOURCES

---

In nature, most materials are three dimensional objects. At a nanometer scale, the ability to visualize the 3D organization and the properties of artificial or biological systems is of high impact in science, medicine and technology. The field of coherent X-ray diffractive imaging is expected to realize high-resolution three-dimensional imaging thanks to the fact that this technique does not requires any optics. Additionnaly, using ultrashort soft X-ray pulses, lensless imaging opens the possibility to study 3D ultrafast dynamics at a nanometer scale. The typical way to make 3D reconstruction of the object is the tomography method in which the object is scanned angle by angle. It requires multiple acquisitions at different observation angles of the object. For dynamic studies in pump probe experiment, if the object will irreversibly be transformed or be destroyed after being pumped, one should prepare enough quantity of identical samples, which could be a problem for unique objects or processes that are not reproducible. To overcome this problem, retrieving 3D information from single acquisition is necessary. To explore this perspective it is necessary to develop 3D single shot imaging techniques. Otherwise only reversible systems could be analyzed with a time resolution given by the short pulse duration. The first 3D CDI experiment were performed using and assembling a set of 2D views of a sample at different angles [62, 66, 86]. However, the need of different views increases the time of acquisition and prevents time resolved studies of irreversible phenomena. Single shot methods for 3D imaging have already been developed. A solution has been given by a novel imaging concept proposed by the research group of J. Miao, called ankylography, which “under certain circumstances enables complete 3D structure determination from a single exposure using a monochromatic incident beam” [72]. Ankylography is a coherent imaging technique based on the oversampling method. It shares a similar experimental arrangement as CDI. However, this method introduces additional constrains that may not always be satisfied [72].

In this chapter, we extend our actual 2D ultrafast nanoscale imaging techniques to ob-

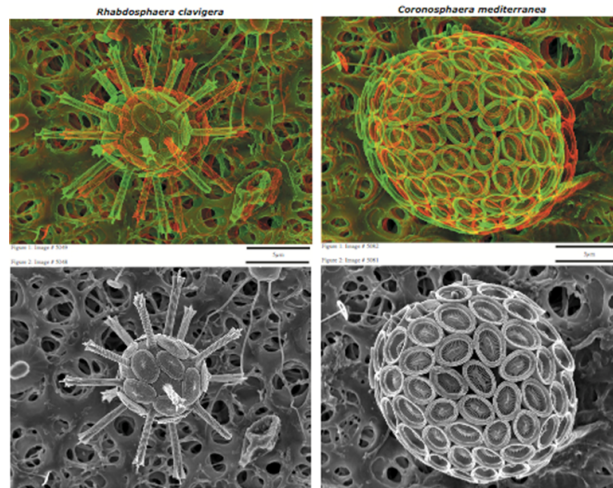


Figure 3.1: Stereo image (red-green photos) of plankton samples made by digital combination of SEM images (gray scale) taken at different observation angles. Picture extracted from Ref. 1.

tain 3D images. It is based on the stereo viewing of our sample. Ultrafast *Single shot 3D stereo* would allow lowering the impact of X-ray exposure in image reconstruction. Stereo imaging is based on human vision. Our right and left eyes take two 2D images at different observation angles of the object and the brain combines these images to give the 3D perception. In artificial stereo imaging, each image is associated to the other with a spacing (given by the parallax) and a different color or polarization (this encoding is called an anaglyph). The use of filters in front of the eyes to observe the anaglyph allows the brain to separate each lateral projection related to each eye's image. It is not a real 3D imaging but already provides much more interesting information about the object than 2D imaging.

Fig. 3.1 presents stereo imaging examples of nanoplankton samples realized by a scanning electron microscope [3]. After taking an image (photos in gray scale), the biological samples are tilted about 5 degrees to take the second image.

These two images are then turned into red and green, and combined by the red-green anaglyph method. With red-green glasses, one can see 3D planktons from the combined image. In principle, stereo imaging is compatible with coherent diffractive imaging technique: two CDI or holographic reconstructions taken at different observation angles are recombined a posteriori.

In our case, the multiple projections of the object can be generated using 2 basic configurations,

- (i) 1 beam and multiple orientations of the object
- (ii) 2 beams illuminating the object at 2 angles

Option ii) is a direct solution for the generation of the 2 views in a single shot with two synchronized pulses. We present here a new ultrafast 3D stereo lensless imaging technique with two XUV pulses. Two different setups were developed and tested experimentally with a soft X-ray source generated by a high harmonic generation process. In the first part of this chapter a description of the beamline used to generate the high harmonic source is presented. Then, the two experimental setups are explained. Finally a comparison of the experimental results with the two configurations is made.

---

### 3.1 High harmonic beamline

The 3D stereo lensless technique has been developed at the high harmonic beamline at CEA-Saclay, France, presented in Fig. 3.2. We use the infrared femtosecond laser facility LUCA (Laser Ultra Court Accordable). The harmonic beamline works with up to 50mJ of energy of the Ti:sapphire laser that delivers pulses of 60 fs at  $\lambda = 795$  nm and a repetition rate of 20Hz. For imaging applications a high flux of photons is needed. This is reached by using a loose focusing configuration with a long focal length lens and a variable length cell. The experimental results presented in this thesis have been generated with a focal lens of  $f = 5.65$  m. Different parameters can be controlled to improve the high harmonic generation. In a first phase, the position of the focusing lens with respect to the gas cell can be adjusted using a motorized translation stage for the focussing lens. The IR beam size is adjusted with an iris placed in front of the focusing lens to improve phase matching. The gas cell, located in the "HHG chamber" (Fig. 3.2), has an adjustable length up to 12 cm. Two pinholes of 1 mm of diameter are fixed at the input and output of the cell. An initial alignment of the cell is made with a motorized system that allows the control of the vertical and horizontal pinhole position with respect to the fixed output pinhole. The horizontal position of the whole cell system is controlled by a motorized translation stage. This allows an initial alignment of the beamline without the cell. The gas pressure is monitored and controlled. After the high harmonic generation, the IR beam propagates in the same direction as the harmonic beam. To avoid damages on the optical devices, samples and detection systems, the IR must be filtered. A large part of the IR beam (90%) is removed in the "Optics chamber" (Fig. 3.2) using an IR anti-reflective mirror in grazing incidence. This mirror allows to send the HH beam (90% HH reflectivity at grazing incidence) to the "Imaging chamber" (Fig. 3.2). The remaining IR beam is filtered out using 2 Al filters (LUXEL filters with 5 nm Carbon - 100 nm Al - 5 nm Carbon). In the basic configuration, the "Diffraction chamber" (Fig. 3.2) is composed by an off axis parabola ( $f = 22$  cm) to focus the harmonic beam on the sample and a X-ray CCD camera to register the soft X-rays diffracted by the sample. The parabola has a multilayer coating to select a single harmonic. The position of the parabola is controlled by a horizontal motorized translation stage and a rotation stage that allows



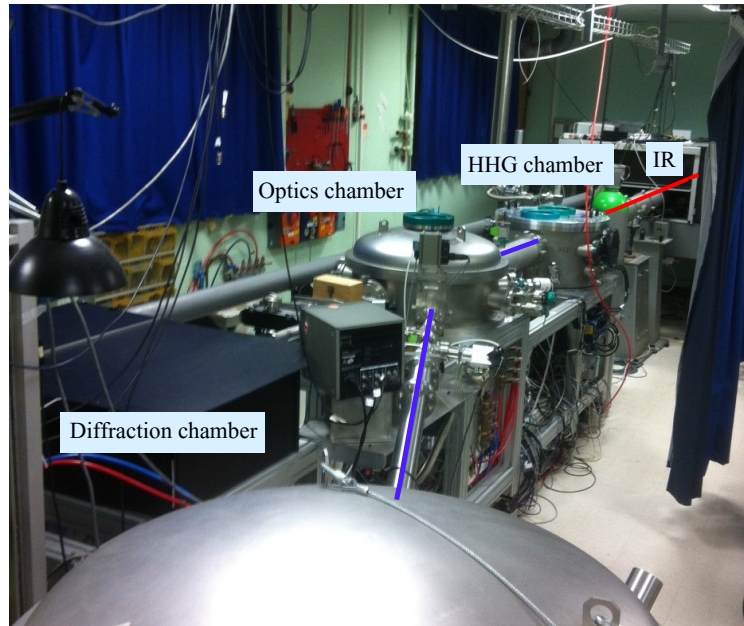


Figure 3.2: High harmonic beamline at CEA-Saclay.

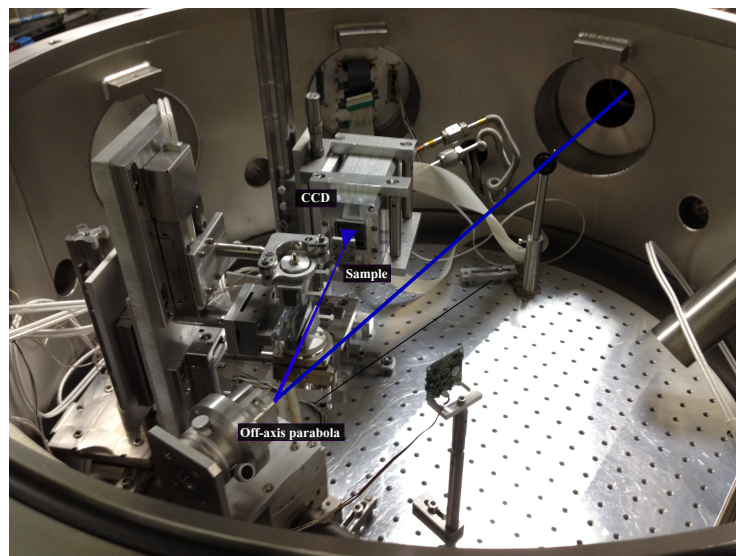


Figure 3.3: High harmonic beamline at CEA-Saclay

aligning the parabola. The position of the sample is controlled by a motorized system with three translation stages and a rotation stage with a nanometer precision (SmarAct stage system). The far-field diffraction pattern are detected with an X-ray CCD camera (PI-MTE CCD from Princeton Instrument) of  $2048 \times 2048$  pixels with a pixel size  $p = 13.5 \mu\text{m}$ .

## 3.2 Two sources stereo lensless setup

Using the laboratory-scale HH facility at CEA-Saclay our group demonstrated that it is possible to perform single-shot imaging at nanometer scale [32, 34, 73]. Our 3D stereo lensless imaging technique is based on merging 2D views (anaglyph) obtained either using CDI or holographic lensless imaging techniques. Two HH beams are focused with two view angles on the sample to generate at the same time two diffraction patterns that are recorded simultaneously with the X-ray CCD camera. Post analysis of each one of the diffraction pattern gives us the reconstruction of the two projections at two different angles. Such a experimental setup carries two main challenges, the first one is to generate the two HH beams, the second one it is to be able to focus them simultaneously with a different angle of incidence on the sample. We have taken into account different constraints such as the focal length of the off axis parabola used to focus the beam on the sample and the size of the CCD camera to detect both diffraction patterns. Two different solutions have been explored during this thesis and are based on different setups. Both are based on the use of two half beams after splitting the direct HH beam. The description of the different 3D lensless imaging setups developed are presented in the next two subsections.

### 3.2.1 Two parallel plates setup

The first solution proposed is based on a two parallel plates setup to split the direct HH beam before the off axis parabola (Fig. 3.4). Using the sharp edge of the first silicon plate, the harmonic beam is separated in two half beams, a direct half beam that continues in the same direction as the incident beam and a reflected half beam. The second silicon plate deflects the reflected beam to be parallel to the incident beam. The off axis parabola filters out (thanks to a multilayer coating) one harmonic wavelength and focuses the beams onto the same spot but with a different angle of incidence. The maximum angle that can be achieved is simply given by the numerical aperture of the off axis parabola. Practically, the angle of incidence can be controlled by the distance between the two beams on the parabola. For this, a motorized translation stage was used to change the lateral position between the two parallel plates. The angle between the beams is given by

$$\theta = 2 \arctan\left(\frac{d}{2f}\right), \quad (3.1)$$

where  $d$  is the distance between the two beams on the off axis parabola and  $f$  is the focal length. The simulation of the beam profile at the focus (Fourier transform of the incident beam) shows that the shape of the half beam at focus is regular, comparable to the one of the full Gaussian beam. The waist size at focus for the half Gaussian beam is larger by a factor  $\sim 2$  than the Gaussian beam (Fig. 3.5).

The far field image of the two half Gaussian beams (autocorrelation of each beam) generated with this setup is presented in Fig. 3.6. The right beam corresponds to the beam

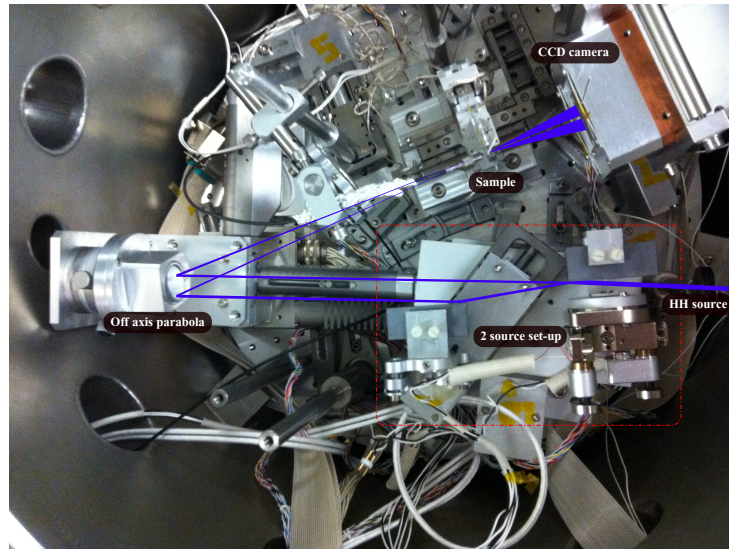


Figure 3.4: Stereo lensless imaging setup developed at the CEA-Saclay. The two source setup (marked with the red square) is based on a two parallel plates to split in two the incident harmonic beam.

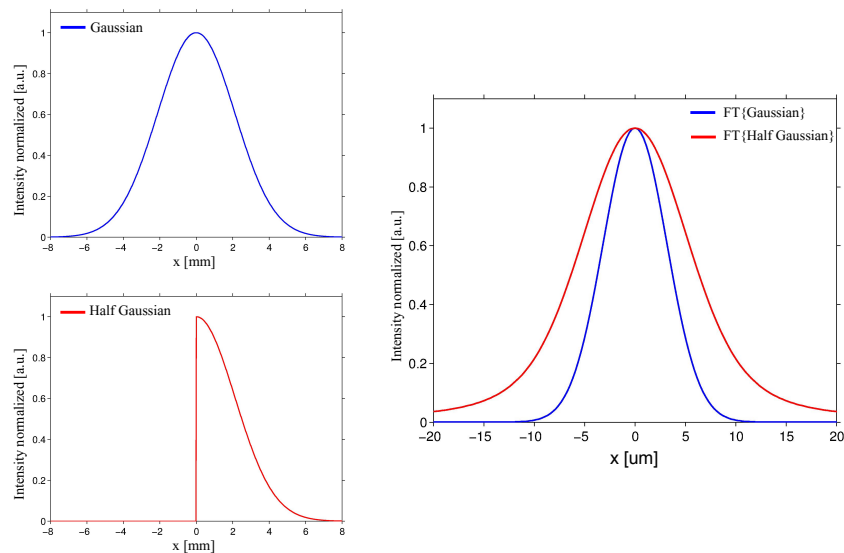


Figure 3.5: Left, Gaussian (up) and half Gaussian (down) beam profile before focusing. Right, simulation of the beam profile at focus with a Gaussian (blue) and a half Gaussian (red) beam.

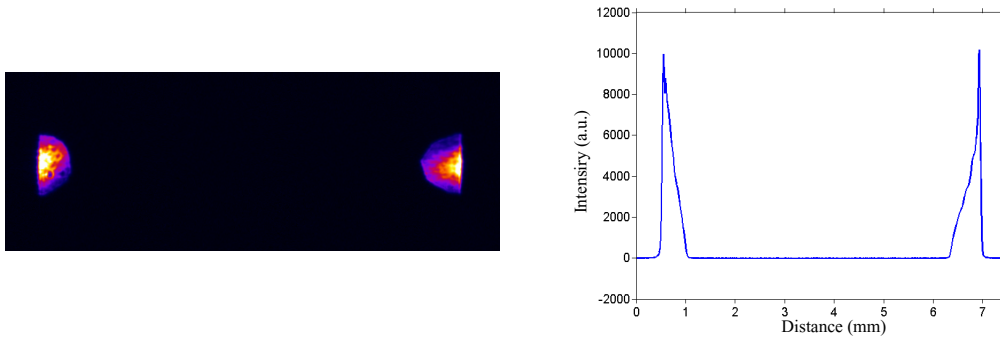


Figure 3.6: Left, experimental image of the two half beams generated with the two mirror setup. Right, two beam horizontal profiles.

reflected twice on the silicon plates, and the left beam to the half direct beam. The reflection of the right beam on the silicon plates decreases the flux of photons making it weaker with respect to the half direct beam. To compensate for the difference in the flux of photons the criteria that we have used to split the beam is the total flux of photons instead of an equal area. The horizontal profile of the two beams is shown in Fig. 3.6. We can see that the total intensity is similar but the size of the right beam is slightly larger than the left one. The total flux of photons in each beam is  $5 \times 10^5$  photons/shot.

The two beams were focused on a 3D nanometer object and their far field diffraction patterns were registered simultaneously with the X-ray CCD camera. The samples were drilled on a Si<sub>3</sub>N<sub>4</sub> membrane using a focused ion beam (FIB). The membrane has a layer of 100nm of gold to make it opaque to the harmonic signal. The 3D objects consist of a pattern drilled in an open window. The window is bent by different angles with respect to the membrane plane (Fig. 3.7 (d)). The technique I developed to drill the 3D objects contains two steps. First, a 2D pattern of the object is drilled on the membrane (Fig. 3.7 (a)-(b)). To bend the window with respect to the membrane we remove a nanometric layer of gold on the bottom line of the window (line on the region marked with the red dots in Fig. 3.7 (c)-(d)). Locally, the surface constraints are changed so that the window starts to open when removing more and more material. By adjusting the time of irradiation and the dose used for the final line of the square we can control the angle of the window deviation.

### Experimental results using the two parallel plates setup

For the experimental campaign, an off axis parabola with a diameter of 1.5 inches and a focal length  $f = 22$  cm was used. The off axis parabola has a multilayer coating that selects the 25<sup>th</sup> harmonic of the IR laser. The coating covers a surface with a diameter of 3.4 cm. The HH beam was generated with an IR laser (800 nm, 35.8 mJ, 50 fs) focused into a 6 cm gas cell filled with Argon. Two diffraction pattern generated with two beams at  $5.2^\circ$  were registered simultaneously with a single CCD camera. The 3D object used is tilted by

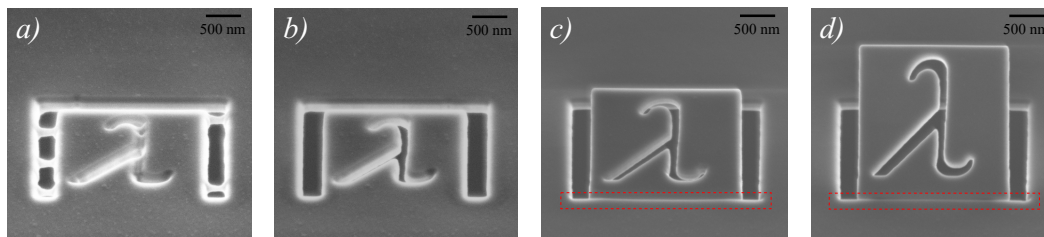


Figure 3.7: Different steps for the milling of a 3D object using a focused ion beam (FIB). (a)-(b) 2D object milling. (c)-(d) 2D window bent at different angles with respect to the membrane after the irradiation on a line inside the red dashed lines. The pictures were taken with the membrane tilted vertically  $60^\circ$  with respect to the electron beam of a SEM

an angle of  $24^\circ$  with respect to the membrane plane (Fig. 3.8). The object has two slits (horizontal and vertical) that are used as holographic extended references [32, 41].

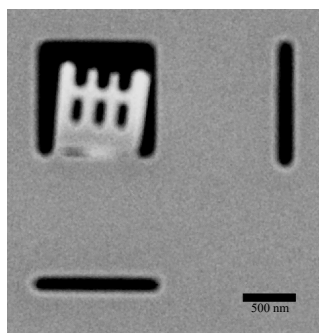


Figure 3.8: SEM image of the 3D object used for the diffraction presented in Fig. 3.9. The object is tilted by an angle of  $24^\circ$  with respect to the membrane plane. Two references (vertical line at right and horizontal line on bottom) are used to do a holographic reconstruction.

Fig. 3.9 presents the experimental far field diffraction pattern, from the accumulation of 400 pulses. We clearly see that two diffraction patterns from the two views are overlapping at the central part. To compensate for this problem we can make use of the centro-symmetry properties of the diffraction pattern. Indeed, the far field diffraction generated by the object is the Fourier transform of the transmittance function and the Fourier transform of a real function has a central-symmetry (quadrants 1st = 3rd and 2nd = 4th). The full far field diffraction of each beam through our amplitude object can be reconstructed using only one half of the diffraction of each beam. This technique may be used in the case where the two diffraction patterns are overlapping over a region smaller or equal to one half of a single view diffraction. The centro-symmetry correction was done using the right half of the diffraction corresponding to the right view and the left one for the left view. The result is presented in Fig. 3.10.

Each diffraction pattern (or hologram) associated to the left and right view, Fig. 3.10



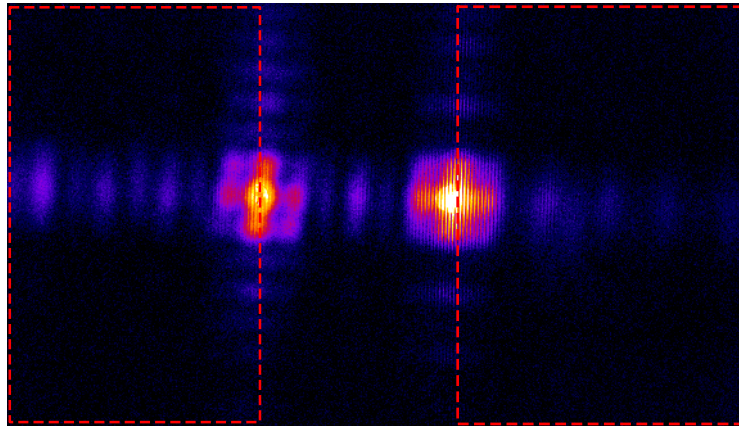


Figure 3.9: Far field diffraction of the 3D object presented in Fig. 3.8 using the two parallel plates 3D stereo setup. The diffraction corresponds to an accumulation of 400 pulses. A binning of 3 is used to increase the signal to noise ratio. Each pixel of Fig. 3.9 corresponds to the total signal in a corresponding zone of 3x3 pixels on the CCD.

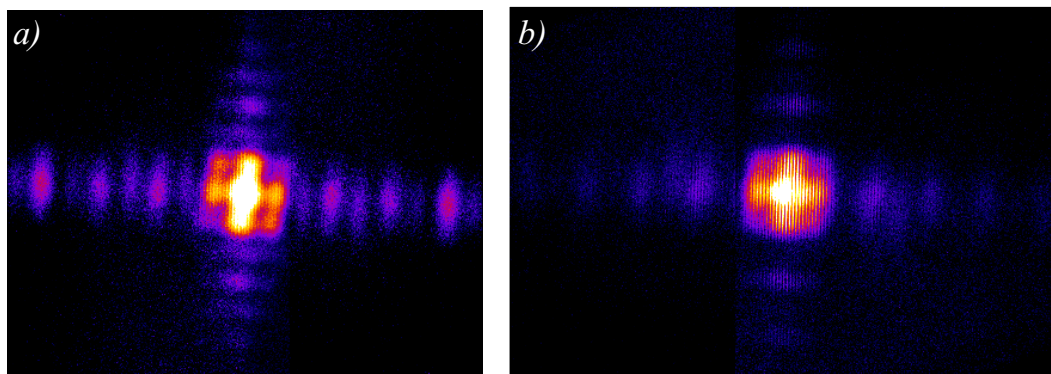


Figure 3.10: Centro-symmetrisation of the two diffraction patterns associated to the two stereo views shown in Fig. 3.9. The symmetrisation is done using the non overlapping part of the diffraction pattern. We finally get the stereo holograms associated to a) left view and b) right view

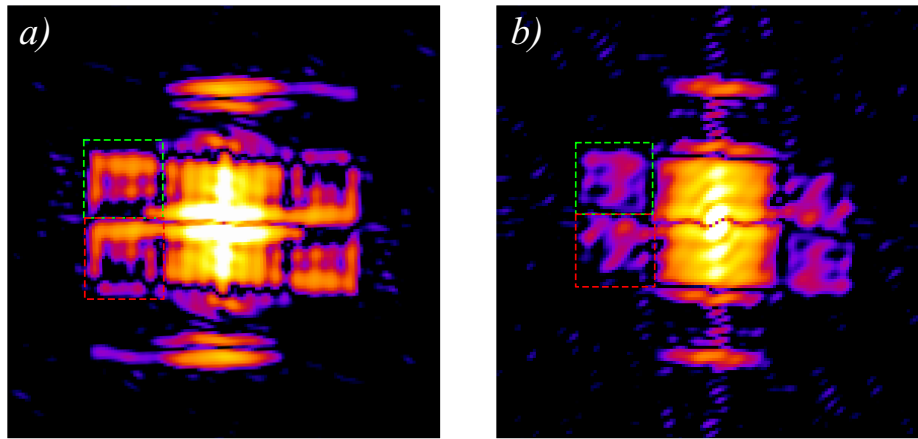


Figure 3.11: Holographic reconstruction of the *a*) left and *b*) right views of the object (Fig. 3.8). The reconstructions were realized using the diffraction patterns of Fig. 3.10.

(a) and (b) respectively, are then computed to perform a holographic reconstruction. The holographic technique uses extended references and is well described in [32, 41]. Basically, this lensless imaging technique is based on the application of linear differential operators to the field autocorrelation, i.e., the inverse Fourier transform of the hologram. In our case, we used vertical and horizontal slits as holographic references (Fig. 3.8). The result of the reconstruction using the vertical extended reference is presented in Fig. 3.11 (a) - (b) (left and right view). In lensless holography with a point-like reference, the Fourier transform of the hologram is composed by three factors, the autocorrelation of the object plus the autocorrelation of the reference (term of order zero), the correlation of the object and the reference, which is called the holographic term and the complex conjugate of this last factor. An ideal point-like source works like a Dirac delta. Its correlation with the object generates in the holographic term the image reconstruction of the object. Practically, the resolution is limited by the real size of the point-like source. In the case of an extended reference, the holographic term is the image of the object blurred by the correlation with the extended reference. The application of a directional derivation in the direction of the slit produces the correlation of the object with the derivation of the slit. For an ideal slit, the derivation is given by two Dirac deltas located at each edge of the slit. This generates two reconstructions of the object, each one associated to one edge of the slit [32, 41]. In Fig. 3.11 we have the two reconstructions plus the complex conjugate of each reconstruction. In Fig. 3.11 (a) we can see how the reconstruction associated to the upper edge of the reference (selected with a green square) presents a better resolution than the one generated with the bottom edge (red square). It can be explained as an effect of an imperfect illumination of the slit. The reconstruction can also be affected by an imperfection at the edge of the reference. The reference will then deviate from a perfect Dirac delta function [41].

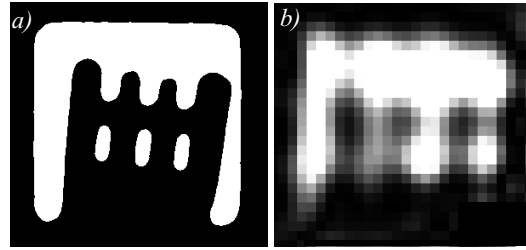


Figure 3.12: a) Binary image of 3D object (Fig. 3.8). b) Holographic reconstruction of the left view of object presented in a).

The comparison between the holographic reconstruction of the left view and the object (Fig. 3.12) shows that the resolution is not enough to see all the details of the object. In the case of the right view the resolution is worse (Fig. 3.11 (b)). There are different factors that deteriorate the resolution. The most important one is the overlap between the 2 diffraction patterns. As it has been said before, it is possible to use only one half of the diffraction to do the reconstruction of the object but it is necessary that the overlap does not extend over more than a half of one beam diffraction. In this case, the overlap affects more than a half of the diffraction of each beam in the horizontal direction (Fig. 3.9). The effect of the overlap is more important in the reconstruction of the right view because the level of signal in the diffraction is lower compared to the left beam. As a consequence the error induced by the left diffraction on the right diffraction is larger than in the opposite case.

On the other hand, the flux of photons of each beam limits the maximum resolution in the reconstruction of the image. The half period criteria defines the resolution as the half period of the maximum frequency of the diffraction pattern detected by the X-ray CCD camera, which is given by [31],

$$r = \frac{\lambda z}{N' \Delta_k}, \quad (3.2)$$

where  $N'$  is the total number of pixels that determines the extension of the diffraction pattern detected on the CCD. Therefore, the factor  $(N' \Delta_k)$  determines the size of the experimental diffraction pattern generated by a beam of wavelength  $\lambda$  and detected at a distance  $z$  from the object.

Additionally, if the photons flux is low, the diffraction signal will be lower and the higher frequencies will be more affected by the noise, deteriorating the final resolution of the reconstruction. The differences in the level of the left and right diffraction signal can be easily seen in the Fig. 3.10 (a) - (b). Even with the criteria used to split the beam (equal flux of photons instead of equal area). Experimentally, we can see a variation between the flux of photons of the left beam (which is stronger than the one of the right beam). This is due to a slight misalignment between the two beams and/or fluctuation of the beam pointing.



From the experimental diffraction pattern (Fig. 3.10) we found the maximum resolution that can be reached with this experimental setup. For this we used the maximum horizontal and vertical extension of the experimental diffraction pattern (Fig. 3.10), that is  $N = 397$  pixels and  $N = 309$  pixels respectively. From Eq. 3.2 we find a maximum resolution of  $r = 135$  nm for the horizontal direction and  $r = 174$  nm for the vertical direction. The size of the smaller details in the 3D object (Fig. 3.8) is 81 nm horizontally and 195 nm vertically, which is smaller than the maximum experimental resolution that can be reached. Taking this into account new 3D objects with details of a minimum size of 200 nm were designed.

The maximum angle between the two beams that can be reached with this setup is  $\theta = 7.4^\circ$ , corresponding to a distance of  $d = 2.6$  cm on the CCD plane. This angle is not enough to avoid the overlap between the two diffraction patterns. A solution to increase this angle is to use a parabola with a larger numerical aperture. We have explored this option with a 3 cm diameter off axis parabola and a focal length of  $f = 10$  cm (compared to 22 cm in the previous setup). Calculations show that the separation between the two stereo beams can reach optimal angles ranging from 10 to 15 degrees. The distance between the diffraction pattern on the CCD plane ensures that for the desired resolution no overlap occurs. In order to select a single harmonic, a multilayer coating was deposited on the off axis parabola (Zerodur substrate with Platinum 800 Å / Chrome 400 Å). The coating has been done at the Center for X-ray Optics at the Lawrence Berkeley National Laboratory's (USA). However the first test of the stereo imaging setup showed a very diffused scattering signal on the CCD (Fig. 3.13). This was due to a high degree of surface roughness of the parabola surface. We decided to design another setup to split the HH beam and increase the angle between the two beams. We will see below that this new setup will allow much more flexibility in angles but also to synchronize the two stereo beams which can be required in pump-probe stereo imaging experiments.

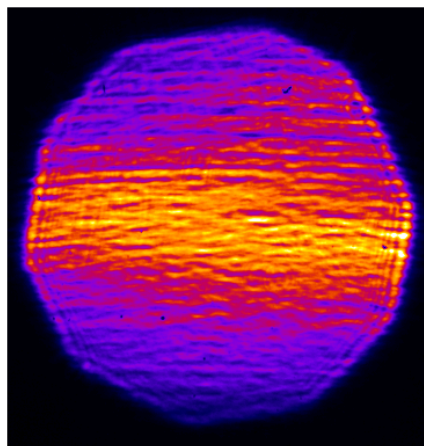


Figure 3.13: Far field diffraction of direct HH beam after being focused by the off axis parabola.

### 3.2.2 Prism setup

Taking into account the experimental restrictions of our setup we developed a new 3D stereo lensless setup (Fig. 3.14). Using the sharp edge of a prism, the HH beam is split in two half beams after the off axis parabola. Two silicon plates are used to control the angle and the recombination of the two beams.

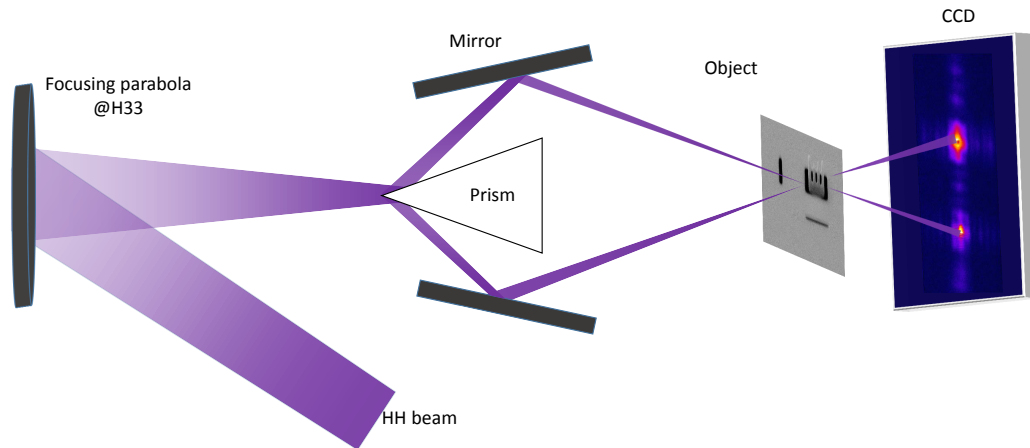


Figure 3.14: Prism setup used to split the HH beam in two half beams. This setup allows controlling the angle between the two beams.

The angle between the incident and the reflected beam on the off axis parabola ( $11.25^\circ$ ) restricts the horizontal dimension of the prism setup, i.e. the maximum distance between the silicon mirror and the prism. Therefore, the setup was installed in a vertical configuration. The distance between the two mirrors determines the position of the two beam overlap. This distance was controlled using motorized vacuum compatible translation stages (Newport MFA-CCV6) on each mirror. The angle between the two beams is controlled by the angle between the mirrors. An additional advantage of this setup is the possibility to control the temporal overlap with the distance between the mirrors and the prism. A first alignment with the IR beam was performed to fix the angle between the beams. The spatial and temporal overlap of the two IR beams was measured using the second harmonic generation in a BBO crystal (Beta Barium Borate). The final overlap at the focus of each beam was achieved by adjusting the distance between the mirrors to the prism and the angle of the bottom mirror. The angle of the mirror was controlled with a piezo actuator system (NewFocus picomotor mirror mount) that can tilt the mirror horizontally and vertically.

A first experimental campaign was performed using an off axis parabola with  $f = 20$  cm and a multilayer coating that selects H25 ( $\lambda = 32$  nm). A picture of the experimental setup

is presented in Fig. 3.15.

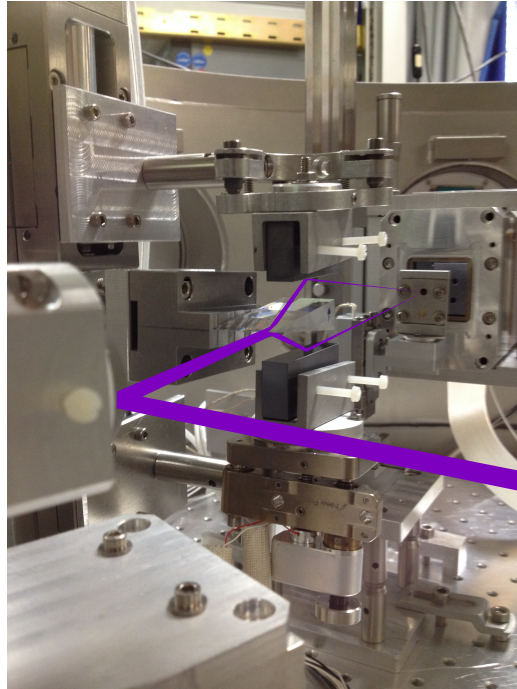


Figure 3.15: Experimental setup for 3D Stereo lensless imaging using the prism setup to split the beam.

A first test of holographic imaging with the direct HH beam was realized using a 3D object with  $2.6^\circ$  of deviation between the window that contains the 2D structure and the membrane (Fig. 3.16 (a)). Fig. 3.16 (b)-(c) present respectively the simulation of the diffraction pattern and the associated holographic reconstruction (with the horizontal slit as reference), at the same wavelength. The experimental results (Fig. 3.16 (d)-(e)) show a clear difference to the simulation. However, the simulation using a broadband spectrum (Fig. 3.16 (f)-(g) ) compound of the harmonics H21, H23, H25, H27 (with the same intensity for each harmonic order) presents the same behavior as the experimental case. This result allowed us to detect a default in the coating of the parabola. Parallel to the Stereo imaging we were working on the multi wavelength imaging project that is presented in the next chapter (Chap. 4). We then focused on the validation of the broadband FTH technique in two dimensions before we continue with the implementation of the 3D-broadband imaging technique.

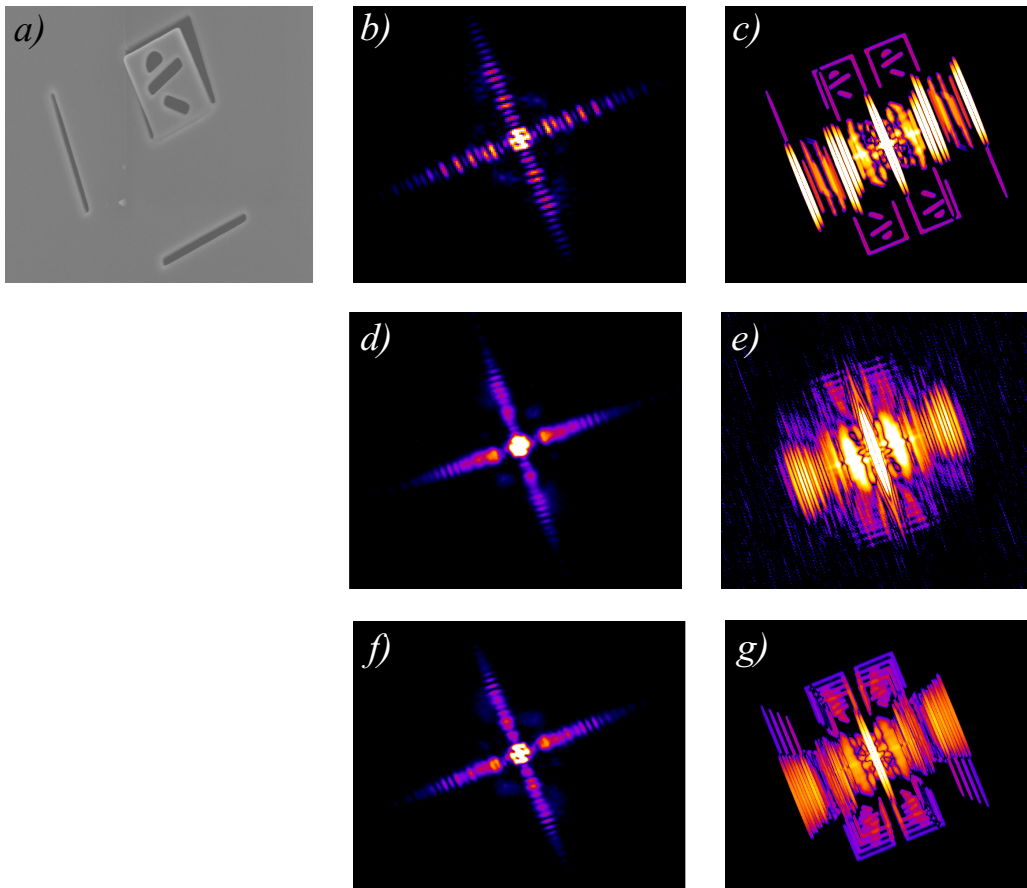


Figure 3.16: a) 3D nanometer object used with  $2.6^\circ$  of deviation between the window that contains the 2D structure and the membrane. b) Simulation of the diffraction pattern using H25. c) Simulation of the holographic reconstruction with the horizontal reference. d) Experimental diffraction pattern of the object a). e) Holographic reconstruction of the experimental diffraction using the horizontal reference. f) Simulation of the diffraction pattern using a broadband source ( $H_{21}, H_{23}, H_{25}, H_{27}$  same intensity). g) Simulation of the holographic reconstruction of f) with the horizontal reference

A new experimental campaign using a parabola with a multilayer coating that selects H33 (generated in Neon) has been implemented while writing this manuscript. In this case, the flux of photons is lower than when using H25. Consequently, reaching the desired image spatial resolution is not possible in a single shot.

It is then necessary to increase the flux of photons in the two beams configuration to improve the resolution in the reconstruction. As a perspective of this work, we propose a new solution to generate two beams by avoiding the large loss due to the prism. We can use a "double cell setup" for direct two beam generation. Two gas cells can be set in the harmonic generation chamber (Fig. 3.2). The use of the same IR laser beam for the generation enables the synchronization of the two HH beams. Therefore, splitting the IR

beam is necessary. A characterization of the flux of photons of the harmonic beam in terms of the intensity of generation has to be done to make sure that the new generation conditions can increase the flux of photons with respect to the split setup.

---

### 3.3 Conclusions

In this chapter, the development of a HH imaging beamline to extend our previous 2D ultrafast nanoscale imaging techniques to obtain 3D images is presented. The HH imaging beamline is introduced. Here, we presented a solution to retrieve 3D information from single shot acquisition that would allow following dynamics in pump probe experiments with objects that can be irreversibly transformed or be destroyed after being pumped. For this, a single shot 3D stereo technique was developed in our HH beamline.

Two different experimental solutions for the two sources stereo setup were studied. The first proposed solution generates the two beams by splitting the harmonic beam with a mirror. A second mirror deflects the reflected beam parallel to the incident beam. The two beams are then focused at the same spot by the off axis parabola. This first solution confirmed the possibility to capture two diffraction patterns with the CCD camera at the same time. However, a big constrain lies in the angle between the two incoming beam as this sets the distance between the two diffraction patterns on the detector. We showed that the spatial resolution in the image generated using this setup is restricted with our experimental parameters by the overlap between the two diffraction patterns. Additionally, the two mirrors setup destroys the natural temporal synchronization between the two beams.

A second stereo lensless imaging setup was proposed. This setup splits the beam after the off axis parabola using a prism. The angle between the two beams is controlled using two mirrors. The temporal synchronization of the two beams was obtained by compensating the optical beam path with the position of the mirrors. The synchronization was confirmed at the  $fs$  scale by using the second harmonic of the IR beam generated with a BBO crystal. The experimental results show that this setup allows controlling the distance between the two diffraction patterns on the CCD camera. This increases the effective diffraction area that can be used, improving the theoretical resolution that can be achieved.

The main challenge to improve the experimental resolution is the need to increase the flux of photons. As a perspective of this work we propose the use of a "double cell setup" for the two beam generation. Two gas cells can be set in the harmonic generation chamber (Fig. 3.2). This way we can avoid to split the harmonic flux of photons in two. However, because only half of the IR energy is available for each cell, each beam XUV photon flux will be reduced. A preliminary study of the IR intensity effect in the flux of harmonic photons generated has to be done.

---

# MULTI WAVELENGTH LENSLESS IMAGING

---

Ultrafast lensless imaging at nanometer scale with XUV sources has already been demonstrated with various sources namely laser plasma X-ray lasers, X-ray free electron lasers and high harmonic generation [6, 23, 32, 41, 73, 81]. However, applications have been restricted to single wavelength imaging and femtosecond pulse duration. Indeed, there are strong criteria on the spectral bandwidth and the temporal coherence of the pulses for image reconstruction. Ideally, a monochromatic fully coherent beam has to be used. These past decades have seen the emergence of attosecond Science ( $1\text{as} = 10^{-18}\text{ s}$ ) starting in the early 90s from the prediction of sources generating trains of attosecond pulses (1), followed by remarkable advances in attosecond source generation (2), attosecond metrology (3) and applications (4). Up to now, only high harmonic generation has demonstrated the capability to produce trains of attosecond pulses. HHG, resulting in short wavelengths (1 – 100 nm typically) emission, provides a unique opportunity to probe the most intimate components of matter with both unprecedented space and time resolutions. To take potentiality into reality, a novel optical system has to be developed with the aim of visualizing the structural evolution of matter at nanometer level and on attosecond time-scale. Additionally to this ultrashort pulse aspect, the broad discrete HHG spectrum can also be used as a multi-wavelength probe which could be element sensitive. Recently, several studies have demonstrated image reconstruction from such diffraction patterns using iterative reconstruction algorithms [1, 14, 21], or by using the scanning of two split and time delayed pulses [92]. These techniques are described for a broadband source with a known discrete spectrum.

Achieving attosecond coherent imaging requires being able to use the intrinsically large spectrum without inducing a blurring of the image reconstruction. Indeed, holography is in principle based on recording the fringe pattern resulting from the interference between a reference wave and the beam scattered by the sample. If the differential path between the two waves is larger than their temporal coherence lengths, then the fringe contrast may drop dramatically and would consequently damage the spatial resolution or would even prevent the object reconstruction. We will discuss those aspects in this chapter. We will also

consider the case of an isolated attosecond pulse where the broad spectrum is continuous. We will see that under given conditions, imaging at a nanometer scale is possible with a isolated attosecond pulse. This technique was developed in collaboration with the group for lasers and plasmas GoLP from the Institute for Plasma Research and Nuclear Fusion at the Technical University (Lisbon-Portugal) and the group of Philippe Zeitoun at LOA-ENSTA (France).

---

#### 4.1 Imaging with multiple harmonic orders

The intensity of the far field diffraction pattern generated by a multi wavelength source is given by the superposition of the intensity diffraction at each wavelength. Therefore, taking into account Eq. 1.26, we have that the intensity of the far field diffraction generated with a source that has a discrete spectrum made of  $N$  wavelengths, is given by

$$I(\vec{\rho}, z) = \sum_{n=1}^N \frac{1}{\lambda_n^2 z^2} T_n^2(\vec{\rho}) \Big|_{\vec{\rho}/\lambda_n z}, \quad (4.1)$$

where  $T_n(\vec{\rho})$  corresponds to the Fourier transform of the transmittance function of the object  $t(\vec{r}, \lambda_n)$  at the  $n$ -th wavelength  $\lambda_n$ . The normalized coordinates  $(\vec{\rho}/\lambda_n z)$ , spatially scales the Fourier transform in terms of each wavelength  $\lambda_n$ . It generates in the total intensity (4.1), a superposition of the Fourier transforms of the object transmittance scaled by each wavelength of the spectrum.

Following the description of the Fourier transform holography FTH with point-like sources (Sec.1.4), and taking into account the linearity of the Fourier transform, the inverse Fourier transform of the intensity distribution generated with the multi wavelength source (4.1) is given by

$$FT^{-1} \{I(\vec{\rho}, z)\} = \sum_{n=1}^N [o_n(\vec{r}) \otimes o_n(\vec{r}) + r_n(\vec{r}) \otimes r_n(\vec{r}) + o_n(\vec{r}) \otimes r_n(\vec{r} - \vec{r}_0) + r_n(\vec{r} + \vec{r}_0) \otimes o_n(\vec{r})] \Big|_{\lambda_n z \vec{r}}, \quad (4.2)$$

where the holographic reconstructions are given in terms of the vector position  $\vec{r}'_n = \lambda_n z \vec{r}$ . Thus, we have a superposition of reconstructions scaled at the different wavelengths ( $\lambda_n$ ). From Eq. 1.31 we see clearly that the reconstruction associated with each  $\lambda_n$  presents a different pixel size in the holographic reconstruction  $\Delta r_n$ , given by

$$\Delta r_n = \frac{\lambda_n z}{N \Delta k'}, \quad (4.3)$$

Taking into account the position of the reconstruction in the discrete representation (Eq. 1.32) and the pixel size (Eq. 4.3) we find that, the position of each reconstruction changes as a function of  $\lambda_n$

$$\vec{P}_n = \vec{r}_0 / \Delta r_n. \quad (4.4)$$

Therefore, the change of scale generates a separation of the different reconstructions in the discrete representation. This effect of separation in the discrete representation is useful for the spectrally resolved imaging technique that is presented in the following part of this chapter.

From Eq. 4.4 we see that the distance, in the discrete representation, between the reconstruction at two different wavelengths ( $\lambda_n, \lambda_m$ ) is

$$\vec{P}_{nm} = \vec{r}_0 \left( \frac{1}{\lambda_n} - \frac{1}{\lambda_m} \right), \quad (4.5)$$

where  $\vec{P}_{nm}$  has been normalized to the factor  $\Delta p = (N\Delta k/z)$ . This result can be written in physical units in terms of the pixel size of the central wavelength ( $\bar{\lambda}$ ) of a broadband spectrum as,

$$\begin{aligned} \vec{D}_{nm} &= \vec{P}_{nm} \Delta \bar{r} \\ &= \bar{\lambda} \vec{r}_0 \left( \frac{1}{\lambda_n} - \frac{1}{\lambda_m} \right). \end{aligned} \quad (4.6)$$

From Eq. 4.5 we can see that the reconstructions are spatially separated in the direction of the vector  $\vec{r}_0$ . Then, to generate a spectrally resolved image it is necessary to satisfy the relation

$$|\vec{P}_{nm}| > \frac{|\vec{a}_{max}|}{2} \left( \frac{1}{\lambda_n} + \frac{1}{\lambda_m} \right), \quad (4.7)$$

where  $\vec{a}_{max}$  is the maximum object size measured in the direction of  $\vec{r}_0$ . If we replace Eq. 4.5 into Eq. 4.7 we have the relation to calculate the minimum distance  $\vec{r}_0$  needed to generate the spectrally resolved image.

$$|\vec{r}_0| > \frac{|\vec{a}_{max}|}{2} \left( \frac{\lambda_n + \lambda_m}{\lambda_m - \lambda_n} \right). \quad (4.8)$$

For a given discrete spectrum, the minimum distance  $\vec{r}_0$  must be calculated in terms of the closest wavelengths ( $\lambda_n, \lambda_m$ ) in the spectrum. This result is also valid for the case of holographic imaging with extended references HERALDO [32, 41].

Fig. 4.1 presents the simulation of the multi wavelength holographic reconstruction using a source with a spectrum that contains three IR harmonics (H23, H25, H27) of equal intensities. Using the HERALDO imaging technique, the two edges of the vertical slit (Fig. 4.1 (a)) act as two point-like references. The two vectors ( $\vec{a}_1, \vec{a}_2$ ) determine the direction of the multi wavelength reconstruction. In this case  $|\vec{a}_{max1}| = |\vec{a}_{max2}| = 1 \mu\text{m}$ . The distance  $\vec{r}_0 = 27 \mu\text{m}$  was chosen to satisfy Eq. 4.8. The simulation of the hologram generated by the object (Fig. 4.1 (a)) is presented in Fig. 4.1 (b) with a logarithmic color scale. The application of the HERALDO procedure leads to a spectrally resolved image with respect to



two different references (Fig. 4.1 (c)). Fig. 4.1 presents the simulation of the multi wavelength holographic reconstruction using a source with a spectrum that contains three IR harmonics (H23, H25, H27) of equal intensities. Using the HERALDO imaging technique, the two edges of the vertical slit (Fig. 4.1 (a)) act as two point-like references. The two vectors  $(\vec{a}_1, \vec{a}_2)$  determine the direction of the multi wavelength reconstruction. In this case  $|\vec{a}_{max1}| = |\vec{a}_{max2}| = 1 \mu\text{m}$ . The distance  $\vec{r}_0 = 27 \mu\text{m}$  was chosen to satisfy Eq. 4.8. The simulation of the hologram generated by the object (Fig. 4.1 (a)) is presented in Fig. 4.1 (b) with a logarithmic color scale. The application of the HERALDO procedure leads to a spectrally resolved image with respect to two different references (Fig. 4.1 (c)).

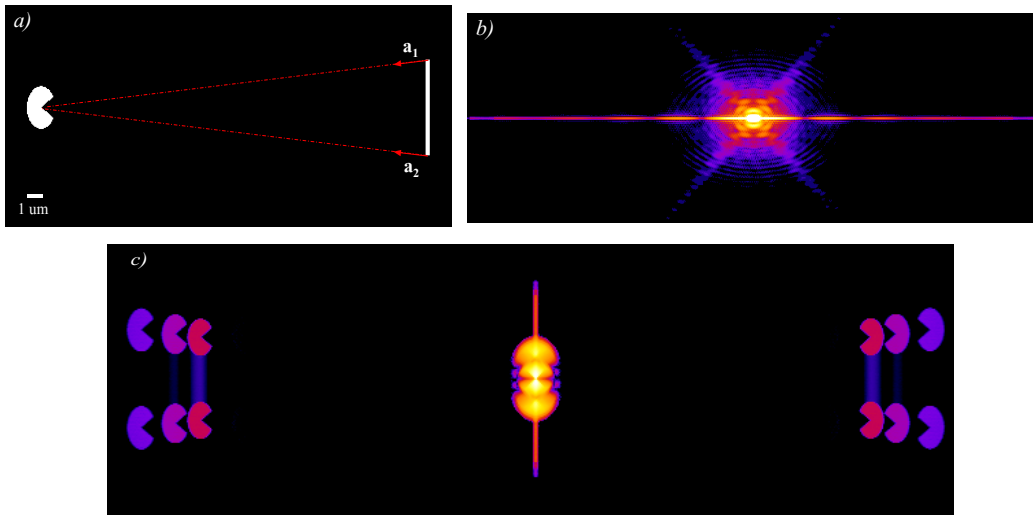


Figure 4.1: Simulation of the spectrally resolved image reconstruction. *a*) Holographic object. *b*) Far field diffraction pattern generated by the object *a*) irradiated with a harmonic source that has a flat spectrum composed by H23, H25 and H27. The color scale corresponds to  $\log$  of the diffraction intensity. *c*) Spectrally resolved holographic image reconstruction of object *a*) (Logarithmic color scale).

If the distance object-reference  $\vec{r}_0$  does not satisfy the spectral separation (Eq. 4.8) the spectral reconstructions are overlapped. This can be seen in the result of the simulation made in the same conditions as in Fig. 4.1 but using a smaller distance ( $|\vec{r}_0| = 10 \mu\text{m}$ ) (Fig. 4.2).

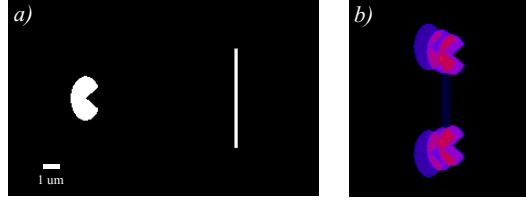


Figure 4.2: Holographic imaging simulation. a) Object with an extended reference (slit) at  $10 \mu\text{m}$  from the center of the object. b) Holographic reconstruction (logarithmic color scale) of the object (a) irradiated with the harmonics H23, H25 and H27.

The overlap effect can be used to generate an holographic reconstruction with a broadband source. As we know, the temporal pulse duration is inversely proportional to the spectral bandwidth. Therefore, the development of lensless imaging techniques with a broad spectrum opens the possibility to improve the temporal resolution of the imaging process.

Attosecond pulses require a broad spectrum spanning several eV's in the XUV [69]. The broad spectrum of the attosecond source can be discrete, leading to a train of attosecond pulses [69] or continuous if an isolated attosecond pulse is generated [43]. To achieve attosecond resolution in imaging it is necessary to have a source of isolated attosecond pulses, i.e. a continuous and broad spectrum.

In this section, an alternative solution for imaging with a continuous broadband source based on the Fourier transform holographic scheme is demonstrated. This method does not require prior knowledge of the source spectrum.

As it has been shown (Fig. 4.1–4.2), the overlap effect can be controlled by changing  $\vec{r}_0$  (Eq. 4.5). In the case of the spectral imaging superposition, a minimum  $\vec{P}_{nm}$  is needed. From Eq. 4.5 it is clear that a perfect superposition with  $\vec{P}_{nm} = 0$  (all the spectral reconstructions centered at the same point) is not possible in terms of the discrete representation. This, and the different size of each spectral reconstruction induce a blur effect that reduces the resolution of the final image. For a given spectrum, the maximum overlap (minimum distance  $\vec{P}_{nm}$ ) is then achieved when we minimize the object-reference distance  $\vec{r}_0$  (Eq. 4.5).

In the case of a monochromatic source, the minimum distance object-reference  $\vec{r}_0$  is given by the holographic condition

$$|\vec{r}_0| > \frac{3}{2} |\vec{a}_{max}|, \quad (4.9)$$

this relation avoids the superposition between the autocorrelation term  $[o(\vec{r}) \otimes o(\vec{r}) + r(\vec{r}) \otimes r(\vec{r})]$  centered in the Fourier transform of the hologram and the reconstruction  $[r(\vec{r} + \vec{r}_0) \otimes o(\vec{r})]$  (Eq.1.30).

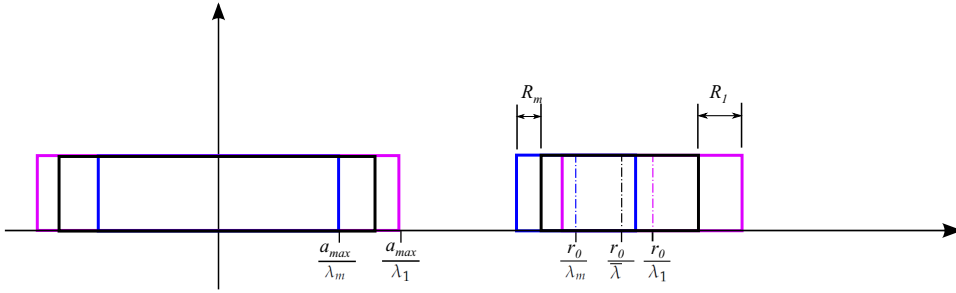


Figure 4.3: Broadband holographic reconstruction.  $R_1$  and  $R_m$  are the difference in size of the central wavelength reconstruction ( $\bar{\lambda}$ ) with respect to  $\lambda_m$  and  $\lambda_n$  respectively. Only one dimension effects are shown.

For a broadband source, the holographic condition has to take into account the superposition of the spatially scaled autocorrelations that form the spectrum  $\sum_{n=1}^N [o_n(\vec{r}) \otimes o_n(\vec{r}) + r_n(\vec{r}) \otimes r_n(\vec{r})]$  (Eq. 4.2).

Fig. 4.3 presents an example of the different terms in the holographic reconstruction using a broadband source with a spectral width  $\Delta\lambda = (\lambda_m - \lambda_1)$ . To simplify, in Fig. 4.3 only the minimum and maximum wavelengths are shown, the effect on the rest of the spectrum (discrete or continuous) is similar and is limited by the minimum and maximum wavelengths.

The holographic multi wavelength condition is then related to the maximum size of the autocorrelation term ( $2\bar{a}_{max}/\lambda_1$ ) (centered at zero) and the closest reconstruction, that corresponds to the maximum wavelength  $\lambda_m$  and has a total size ( $\bar{a}_{max}/\lambda_m$ ) centered at the position  $\vec{r}_0/\lambda_m$ . Therefore, the holographic multi wavelength condition can be written as

$$|\vec{r}_0| > |\bar{a}_{max}| \left( \frac{1}{2} + \frac{\lambda_m}{\lambda_1} \right). \quad (4.10)$$

The broadband reconstruction consists in the superposition of each spectrally scaled reconstruction of size ( $\bar{a}_{max}/\lambda_n$ ) (Eq. 4.2). The central position of each spectral reconstruction is given by ( $\vec{r}_0/\lambda_n$ ). The scale in the size and the shift of the central position as a function of  $\lambda_n$  generates an effect of blur in the broadband FTH. This effect is not symmetric with respect to the right and left side of the object reconstruction. The blur can be given in terms of reconstruction associated to the central wavelength  $\bar{\lambda}$ , i.e. as the distance  $R_m$  and  $R_1$  (Fig. 4.3) normalized respect to the central size ( $\bar{a}_{max}/\bar{\lambda}$ ).

$$\frac{R_m \bar{\lambda}}{|\bar{a}_{max}|} = \left( 1 - \frac{\bar{\lambda}}{\lambda_m} \right) \left( \frac{\vec{r}_0}{|\bar{a}_{max}|} - \frac{1}{2} \right). \quad (4.11)$$

$$\frac{R_1 \bar{\lambda}}{|\bar{a}_{max}|} = \left( \frac{\bar{\lambda}}{\lambda_1} - 1 \right) \left( \frac{\vec{r}_0}{|\bar{a}_{max}|} + \frac{1}{2} \right). \quad (4.12)$$

From Eq. 4.10 in Eq. 4.11 – 4.12 we can write the minimum blur as,

$$R_{mN} > \frac{\Delta\lambda}{2\lambda_1}. \quad (4.13)$$

$$R_{1N} > \frac{\Delta\lambda\bar{\lambda}}{\lambda_1^2}. \quad (4.14)$$

Where  $R_{mN} = R_m\bar{\lambda}/|\bar{a}_{max}|$  and  $R_{1N} = R_1\bar{\lambda}/|\bar{a}_{max}|$ . As  $\lambda_1 < \lambda_m$ , the resolution on the left side of the reconstruction will be better than the one on the right (Eqs. 4.13 – 4.14). For the case of an isolate attosecond pulse of 530 as with a spectral range of (86 – 94) eV that corresponds to  $\lambda_1 = 13.2$  nm and  $\lambda_m = 14.4$  nm [43], the minimum percentage of blur is  $R_{mN} = 4.5\%$  and  $R_{1N} = 9.5\%$  respect to the total size of the central reconstruction. For a maximum object size of  $|\bar{a}_{max}| = 1 \mu\text{m}$ , the blur corresponds to  $R_{mN} \approx 3\bar{\lambda}$  and  $R_{1N} \approx 7\bar{\lambda}$  (i.e.  $R_{mN} = 41$  nm et  $R_{1N} = 97$  nm), which sets the spatial resolution limit.

The final resolution of the image reconstruction depends also of the reference size and the maximum diffraction frequency captured by the CCD [31]. Eqs. 4.13 – 4.14 are additional factors to take into account to calculate the final experimental resolution.

In a more general way, we can define the total blurring in terms of the distance between the two edges of the broadband reconstruction, i.e. the edge of the reconstruction associated to  $\lambda_m$  and the edge corresponding to  $\lambda_1$  (Fig. 4.4).

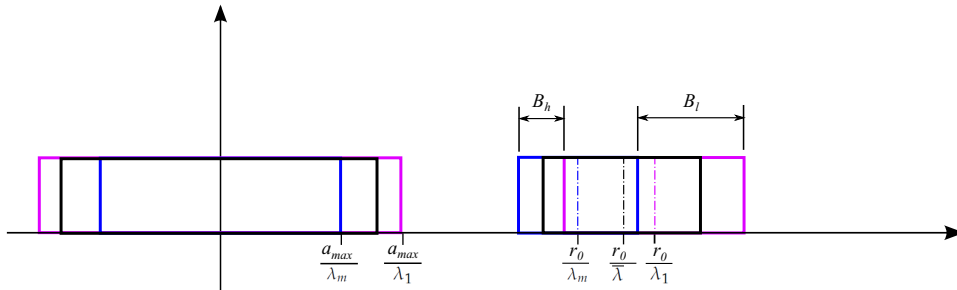


Figure 4.4: One dimension effect of the holographic reconstruction.  $B_h$  and  $B_l$  are the distance of the edge reconstruction associated to  $\lambda_m$  (blue) and  $\lambda_1$  (violet) on the high and low frequency side, respectively. The black reconstruction corresponds to the central wavelength ( $\bar{\lambda}$ ).

Using this description, the total blurring factor can be given in terms of  $\Delta\lambda/\bar{\lambda}$ , as we will see in the following section.

The minimum and maximum blur ( $B_h$  and  $B_l$  respectively) are given at the minimum and maximum spatial frequency present in the reconstruction (Fig. 4.4). As we are interested in the limits of the resolution imposed by the broadband holographic reconstruction we will consider the factor  $B_l$  that is given by,

$$B_l = \left( r_0 + \frac{a_{max}}{2} \right) \left( \frac{1}{\lambda_1} - \frac{1}{\lambda_m} \right). \quad (4.15)$$

From Eq. 4.10 and 4.15 we can see that the minimum blur factor  $B_{lmin}$  is

$$B_{lmin} = a_{max} \left( \frac{2\bar{\lambda}}{\lambda_1} \right) \left( \frac{\Delta\lambda}{\lambda_m\lambda_1} \right). \quad (4.16)$$

Following the description of the previous section, the blur  $B_{lmin}$  normalized with respect to the size of the reconstruction associated to  $\bar{\lambda}$  (in pixel size) is given by

$$\begin{aligned} B_N &= \frac{B_{lmin}}{a_{max}/\bar{\lambda}} \\ &= \left( \frac{2\bar{\lambda}^2}{\lambda_1} \right) \left( \frac{\Delta\lambda}{\lambda_m\lambda_1} \right). \end{aligned} \quad (4.17)$$

Taking into account the relation between the energy  $E$  and the wavelength  $\lambda$ ,

$$E = \frac{hc}{\lambda}, \quad (4.18)$$

where  $c$  is the light speed, we find the normalized blur factor  $B_N$  (Eq. 4.17) in terms of  $\Delta E/\bar{E}$ .

$$B_N = 2 \frac{\Delta E}{\bar{E}} \left[ \frac{1}{\left(1 - \frac{\Delta E}{2\bar{E}}\right)^2 \left(1 + \frac{\Delta E}{2\bar{E}}\right)} \right], \quad (4.19)$$

with

$$\begin{aligned} \Delta E &= E_m - E_1 \\ \bar{E} &= \frac{E_m + E_1}{2}. \end{aligned} \quad (4.20)$$

In case of a linear phase relation between the different components of the broadband pulse, the temporal duration in terms of the Fourier transform limit is given by

$$\Delta E \Delta t \geq \hbar 4 \ln 2. \quad (4.21)$$

From Eq. 4.19 we see that the minimum resolution given by the blur  $B_N$  depends not only on  $\Delta E$  (and therefore on the pulse duration) but also on the central energy  $\bar{E}$ . In Fig. 4.5 some experimental characteristics of isolated attosecond pulses are marked with the triangles. In our case (attosecond pulse train generated with the harmonics H23, H25, H27 of an IR laser), the minimum normalized resolution induced by the blur is  $B_N = 0.34$  (showed with the black star in Fig. 4.5). As we can see in Fig 4.5, for imaging applications the factor  $\Delta E/\bar{E}$  is highly important to be able to retrieve the image. The current minimum blur induced by an isolated attosecond source is 50%. It corresponds to a source with  $\tau = 130$  as generated by polarization gating ([40, 77]). To reduce the blur effect (Fig. 4.5 (b)), and

keep the attosecond temporal resolution, new isolated attosecond sources with high  $\bar{E}$  are needed.

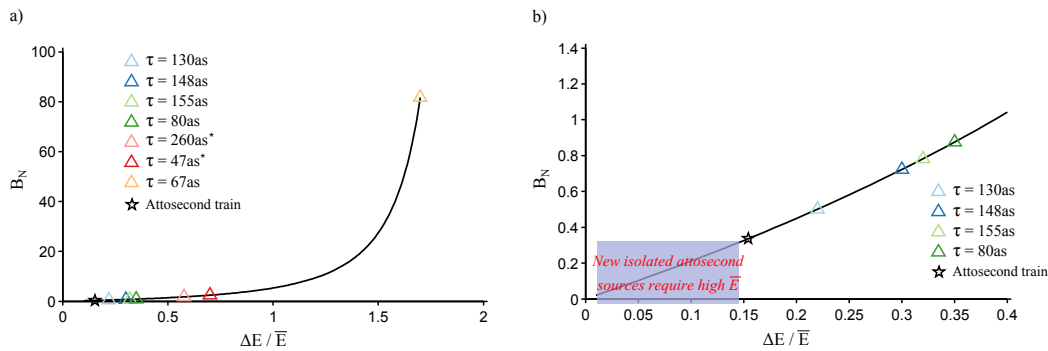


Figure 4.5: a) Minimum resolution induced by blur effect ( $B_N$ ) of a broadband source normalized respect to the object reconstruction at the central wavelength. The triangles corresponds to experimental parameters of attosecond isolated pulses generated currently [15]. The measured duration using different techniques of characterization is presented in the label of the plot. The temporal duration marked with the star corresponds to the theoretic Fourier transform limit value. b) Zoom of (a)

## 4.2 Experimental demonstration of multiple wavelengths holographic imaging

### 4.2.1 Experimental setup

The experimental results presented in this section were obtained at two different HH beamlines. The HH beamline at LOA-ENSTA and the imaging HH beamline at CEA-Saclay driven by the IR laser LUCA (parameters are given in Sec. 3.1).

The harmonic source at LOA was generated with a 2 mJ, 50 fs IR laser (centered at 800 nm) at a repetition rate of 1kHz. The IR source was focused with a  $f = 65$  cm lens inside a 2cm gas cell full of Argon at 25 mbar in a surrounding ambient pressure of  $25 \times 10^{-4}$  mbar. Due to the short focusing configuration for the harmonic generation, the flux of photons is two order of magnitude lower than the case of the imaging HH beamline at CEA. The IR beam that co-propagates with the XUV source is filtered out by a thin (150 nm) aluminium foil. The basic imaging experimental setup (Fig. 3.3) was used. The XUV source is focused with a broadband multilayer coated parabolic mirror. The beam diffracted by the object placed at focus was detected by an X-ray CCD camera ( $2048 \times 2048$  pixels of  $13.5 \times 13.5 \mu\text{m}$  pixel size). An on axis parabolic mirror tilted at  $\approx 10^\circ$  was used. The tilt induced an astigmatism on the beam that generated a spot with an aspect ratio of 1 : 4 on

the object plane. This effect was used to optimize the flux of photons on the sample. The samples used (object + reference) have an overall size of  $(3 \mu\text{m} \times 9 \mu\text{m})$ .

The spectrum of the source reflected by the parabolic mirror was characterized using a two slits interferometer. The far field diffraction pattern (Fig. 4.6 (a)) generated by the two slits of width  $s = 120 \text{ nm}$  separated at a distance  $d = 2.7 \mu\text{m}$ , was detected by the X-ray CCD placed at a distance  $z = 4.7 \text{ cm}$  from the slits. The Fourier transform of the interferogram presents a spectrum composed by a discrete superposition of the harmonics H23, H25 and H27 (Fig. 4.6 (b)). The intensity of H23 and H27 is similar while the harmonic H25 is stronger.

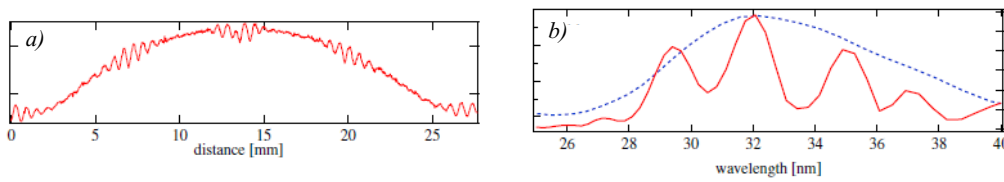


Figure 4.6: Broadband spectrum characterization. a) Two slits far field interferogram generated at the plane  $z = 4.7 \text{ cm}$  with a distance  $d = 2.7 \mu\text{m}$  between the slits centers. b) Spectrum of the source found after Fourier transform of the interferogram (a).

## 4.2.2 Spectrally resolved results

The experimental campaign to demonstrate spectrally resolved holographic imaging took place at the HH beam-line of LOA using the experimental setup described in the precedent section. The object and reference were drilled using a FIB on a  $\text{Si}_3\text{N}_4$  membrane (75 nm thickness) with a gold layer (100 nm). Fig. 4.7 presents a SEM (scanning electron microscope) picture of the object.

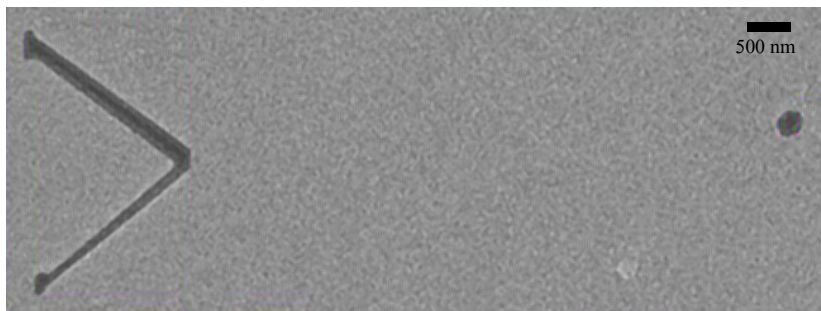


Figure 4.7: SEM image of the holographic sample. The sample is composed of the object  $\Lambda$  and a point-like reference.

The object has an overall size of  $(2.6 \times 1.7) \mu\text{m}^2$  with an asymmetric width. The point-like circular reference was designed to have a diameter ( $h = 120 \text{ nm}$ ), from the SEM picture

we can see that only the central part has been drilled completely, therefore the diameter is  $\sim 2$  times smaller. The distance object reference  $\vec{r}_0 = 5.9 \mu\text{m}$  obeys the spectrally resolved imaging condition, given in Eq. 4.8, taking into account the fact that the maximum object size in the direction of the reference is  $|\vec{a}_{max}| = 230 \text{ nm}$  and the discrete spectrum  $\lambda_1 = 29.6 \text{ nm}$ ,  $\lambda_2 = 32 \text{ nm}$  and  $\lambda_3 = 34.8 \text{ nm}$  (Fig. 4.6).

Fig. 4.8 presents the multi-wavelength hologram detected at  $z = 4.7 \text{ cm}$  from the sample. Because of the low harmonic photon flux, an acquisition of several minutes was necessary, despite the high laser repetition rate ( $1\text{kHz}$ ). The center of the diffraction pattern has been filtered out experimentally to avoid the saturation generated by the direct beam.

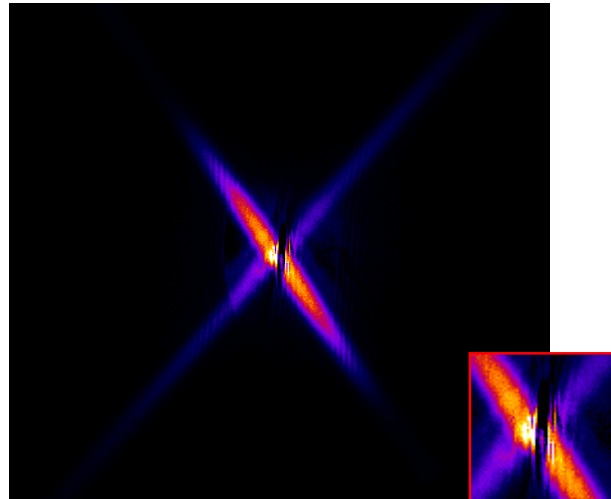


Figure 4.8: Multi-wavelength hologram of the object Fig. 4.7. The inset is a zoom on the central part of the hologram that has been filtered out experimentally to avoid direct beam saturation.

The holographic reconstruction of the diffraction pattern (Fig. 4.8) is presented in Fig. 4.9. The object transmittance is successfully retrieved for each wavelength that is present in the spectrum (Fig. 4.9. (b)) without overlap between the different reconstructions. This demonstrates the spectrally resolved imaging technique when the distance object-reference satisfies the condition presented in Eq. 4.8.



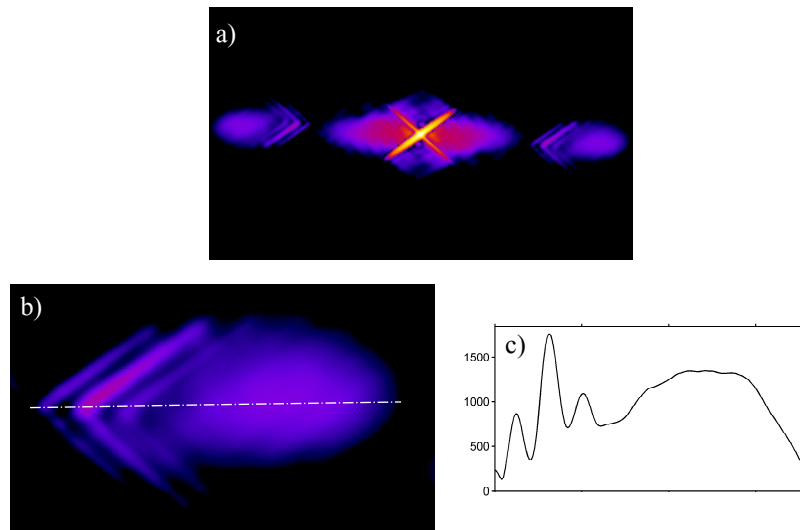


Figure 4.9: a) Holographic reconstruction of the diffraction pattern (Fig. 4.8). b) Zoom on the spectrally resolved image reconstruction which is overlapped with a noise generated by the default at the center of the diffraction pattern (Fig. 4.8). c) Profile through the dotted line of (b). The color scale is logarithmic.

The default induced at the center of the diffraction (inset in Fig. 4.8) generates a noise that is partially overlapping with the spectral reconstructions (Fig. 4.9. (b)). The profile of the reconstruction through the dotted line in Fig. 4.9 (b) is presented in Fig. 4.9 (c). We can see clearly in the profile that the contrast of the image reconstruction is affected by the noise.

The reconstruction can be seen as the correlation between the Fourier transform of the central part with the Fourier transform of the rest of the hologram. Fast variations in intensity between these two regions generates additional noise in the reconstruction. Taking this into account, the center of the diffraction pattern has been filled digitally using a smooth function. The processed hologram is presented in Fig. 4.10 (a). The inset shows in detail the central part. The profile of the spectrally resolved image, taken through the dotted line on the holographic reconstruction (Fig. 4.10 (b)), is represented by the black line in Fig. 4.10 (c). The comparison between the profile after the digital filtering (black line) and the profile before the filtering (red dotted line) shows a clear improvement of the SNR with the use of the digital filter.

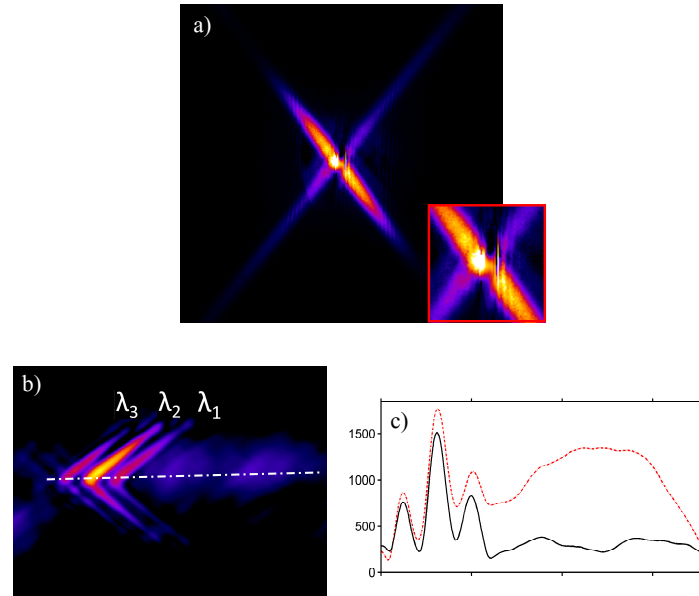


Figure 4.10: a) Hologram digitally filtered at the center. The inset shows in detail the filtered central part. b) Holographic reconstruction of the hologram (a). c) Profile through the white line on the reconstruction ((b)), black line. And profile of the reconstruction without the digital filtering on the center, red dotted line.

In this case, the object has a real transmittance that is equal to one inside the object and zero outside. Consequently, the value of the transmittance retrieved after the reconstruction process depends only on the intensity of the beam at the considered wavelength. This can be clearly seen in the good agreement between the profile of the spectrally resolved image reconstruction (Fig. 4.10 (c)) and the intensity relation between each wavelength given in the spectrum characterization (Fig. 4.6). The highest intensity reconstruction is obtained at  $\lambda_2 = 32$  nm while the reconstructions at  $\lambda_1 = 29.6$  nm and  $\lambda_3 = 34.8$  nm present almost the same intensity. The small intensity difference between  $\lambda_2$  and  $\lambda_3$  presented in the spectrum (Fig. 4.6) is also retrieved in the holographic reconstruction.

The asymmetrical width of the object shown in the SEM picture (Fig. 4.7) is perfectly retrieved in the spectrally resolved reconstruction (Fig. 4.10 (b)). The smaller width of the bottom half generates a lower flux of photons and then a lower intensity in the spectrally resolved image.

The spatial resolution of the spectral reconstruction ( $r_e$ ) was calculated using the pixel size corresponding to each wavelength (Eq. 4.3) with a pixel size of the CCD camera given by ( $\Delta k = 13.5 \mu\text{m}$ ). We adopted the Rayleigh criteria, i.e. the distance between 90% and 10% of the maximum signal on the object profile (Fig. 4.11 (b)). The resolution was measured for each one of the different reconstructions at three different positions (Table. 4.1). The dashed lines on Fig. 4.11 (a) show the positions ( $c_1, c_2, c_3$ ) on the reconstruction generated

Profile	$r_e(\lambda_1)$ [nm] $\pm 10$ nm	$r_e(\lambda_2)$ [nm] $\pm 10$ nm	$r_e(\lambda_3)$ [nm] $\pm 10$ nm
$c_1$	64	70	76
$c_2$	103	111	91
$c_3$	116	139	151
Average	94	107	106

Table 4.1: Resolution of the spectral reconstruction at three different positions on the object reconstruction ( $c_1, c_2, c_3$ ). The error of the measurement is given by the pixel size.

at  $\lambda_3$ .

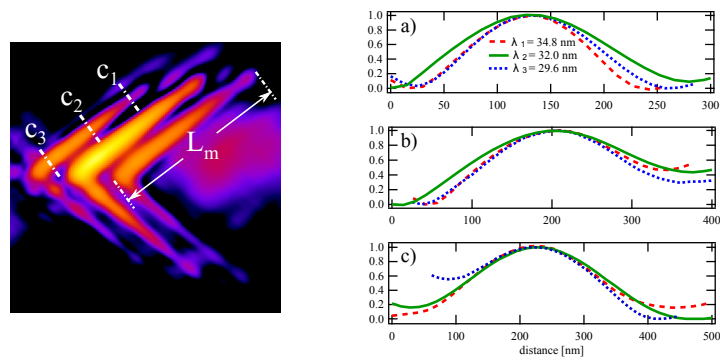


Figure 4.11: Left, spectrally resolved reconstruction. Right, Line-outs along the positions a)  $c_1$  b)  $c_2$  and c)  $c_3$ , along each spectral reconstruction,  $\lambda_1 = 34.8$  nm (dashed red line),  $\lambda_2 = 32.0$  nm (green line) and  $\lambda_3 = 29.6$  nm (blue line).

The best resolution was obtained at position  $c_1$  (Table. 4.1) which is the part where the three object reconstructions have a larger separation. The value of the resolution  $r_e$  increases at positions  $c_2$  and  $c_3$  as a consequence of a partial overlap between the signal of the different reconstructions (at these positions the object width is larger). This partial overlap generates a change of a resolution from  $\sim 2\lambda$  at the position  $c_1$  up to  $\sim 3\lambda$  for the average resolution.

The dimension of the object corresponding to each reconstruction (Fig. 4.11 (a)) was calculated using Eq. 1.31. The length of the upper half object (Fig. 4.11 (a)) has an extension of  $L_{m1} = 1.90 \pm 0.1 \mu\text{m}$ ,  $L_{m2} = 1.89 \pm 0.1 \mu\text{m}$  and  $L_{m3} = 1.88 \pm 0.1 \mu\text{m}$  respectively for each wavelength  $\lambda_1$ ,  $\lambda_2$  and  $\lambda_3$ . This is in perfect agreement with the size  $L_m$  measured from the SEM image (Fig. 4.7),  $L_m = 1.90 \pm 0.01 \mu\text{m}$ . The maximum discrepancy is 1%.

### 4.2.3 Broadband overlapped reconstruction

Following the description presented in Sec. 4.1, a small object - reference distance  $r_0$  was used to generate the broadband overlapped imaging reconstruction. In this case the broad-

band source is composed of a discrete spectrum (Fig. 4.6 (b)). The sample used to generate the overlapped reconstruction is presented in Fig. 4.12.

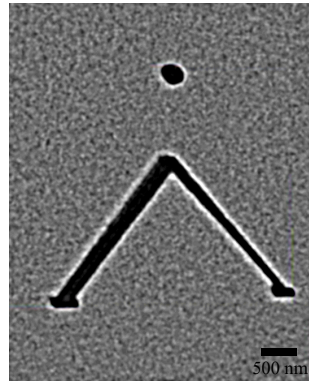


Figure 4.12: Sample used for broadband overlapped imaging. The sample is composed of the object  $\Lambda$  and a circular reference.

The sample has been made using a FIB in the same conditions as the sample of the previous section (fig. 4.7). The object presents an asymmetrical width and a maximum object size of  $|\vec{a}_{max}| = 410$  nm. The small distance object-reference  $|\vec{r}_0| = 1.28 \mu\text{m}$  respects the broadband holographic condition given in Eq. 4.10.

The broadband hologram has been detected in conditions similar to the one of the spectrally resolved hologram (Fig. 4.8). The distance object - CCD is  $z = 4.7$  cm and several minutes of exposition were necessary to capture the far field diffraction. The diffraction pattern (Fig. 4.13 (a)) presents a strong noise at the central part. The noise, that has been generated by parasitic signal scattered on the optical system (inset on Fig. 4.13 (a)), has a well defined circular edge. The Fourier transform of the diffraction pattern (Fig. 4.13 (b)) is then the correlation of the broadband holographic reconstruction with the Fourier transform of the noise. As the noise has a circular profile, we see clearly that the concentric ring structure on Fig. 4.13 (b) is produced by the noise in the diffraction.

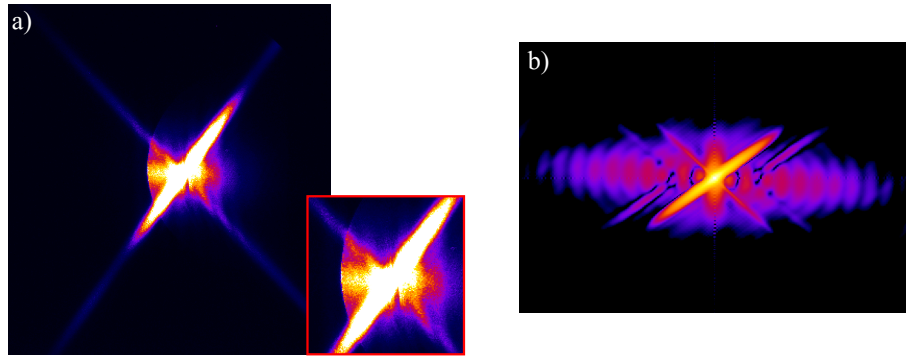


Figure 4.13: (a) Broadband hologram generated with a small object-reference distance (Fig. 4.12). The central part of the hologram (inset) presents a circular shape noise. (b) Broadband holographic reconstruction of (a) in logarithmic color scale.

To filter out the noise on the diffraction pattern we have used the technique of symmetrization. This technique is based on the fact that the Fourier transform of a real function has a center symmetry (Sec. 3.2.1). As the strongest effect of the noise on the diffraction pattern is localized on the left half of the diffraction (Fig. 4.13 (a)), we have used the central symmetry of the right half to correct the default induced by the noise. The result of the symmetrization is presented in Fig. 4.14 (a), the inset shows how the circular noise presented in the original diffraction pattern (Fig. 4.13 (a)) has been completely removed. Consequently, the concentric rings that modulate the broadband holographic reconstruction from the original data (Fig. 4.13 (b)) are not present in the holographic reconstruction of the filtered diffraction (Fig. 4.14 (b)). The improvement of the broadband holographic reconstruction permits to retrieve the whole object, including the bottom half that has a smaller width (Fig. 4.12).

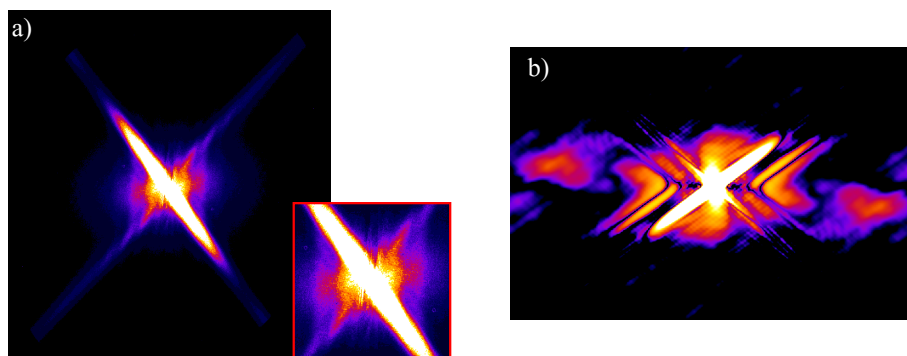


Figure 4.14: a) Central symmetrization of right half diffraction signal in Fig. 4.13 (a). The inset correspond to the central part of the filtered diffraction. b) Broadband holographic reconstruction of (a). The color scale in the reconstruction is in logarithmic scale.

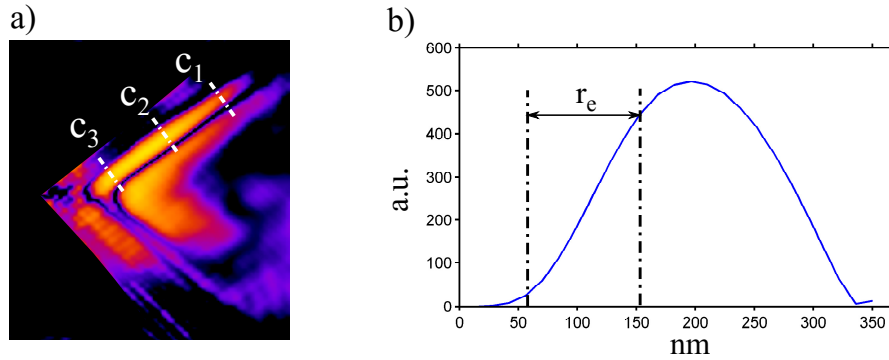


Figure 4.15: a) Broadband holographic reconstruction. The term of autocorrelation has been masked. b) Line out along dashed line  $c_1$  in (a)

Three different profiles at the positions  $c_1$ ,  $c_2$  and  $c_3$  (Fig. 4.15 (a)) were used to calculate the resolution (Table. 4.2). The central wavelength of the broadband source ( $\bar{\lambda} = 32.1$  nm) was used to calculate the pixel size in the holographic reconstruction (Eq. 1.31). The value of the resolution  $r_e$  increases towards the center of the reconstruction plane. This can be explained as a decrease of the SNR. The different sources of noise as the parasitic scattered signal and the direct beam correspond to low frequency noise and therefore are located on the central part of the reconstruction plane. Moreover, the autocorrelation term presents a higher amplitude at the center of the reconstruction plane. These two effects decrease the SNR through the zero in the reconstruction plane generating a change in the resolution from  $\sim 2.6\bar{\lambda}$  on  $c_1$  up to an average resolution  $\sim 5\bar{\lambda}$ .

	$c_1$	$c_2$	$c_3$	Average
$r_e$ [nm] $\pm 10$ nm	84	126	266	159

Table 4.2: Broadband overlapped image resolution at three different positions on the object reconstruction ( $c_1, c_2, c_3$ ).

Considering the spectrum of the broadband pulse (Fig. 4.6), and the superposition of the individual electric fields with an arbitrarily chosen phase relationship, we can expect an XUV pulse consisting of a train of 400 as pulses separated by 1.4 fs in a 25 fs Gaussian envelope. In this case (train of attosecond pulses), each spectral component has a temporal coherence  $\tau$  close to the Gaussian envelope, i.e.  $\tau \approx 25$  fs, and then, the interference needed for the imaging technique can be generated between the field of the first pulse or the last one of the attosecond train. Therefore, the temporal resolution to follow dynamics is given by the 25 fs Gaussian envelope. With a continuous spectrum this technique is still valid. In that case (isolated attosecond pulse) sub-fs resolution can be achieved.

### 4.3 Conclusions

In this chapter, we have presented the experimental demonstration of a new technique of spectrally resolved holographic imaging using a discrete broadband soft X-ray source. High-Harmonic generation sources emitting at short wavelengths (1-60 nm typically) provide a unique opportunity to probe the most intimate component of matter with both unprecedented space and time resolutions. To take potentiality into reality, a novel spectro-imaging system has been developed with the aim to visualize the structural evolution of matter at nanometer level on attosecond time-scale.

Holography is in principle based on recording the fringe pattern resulting from the interference between a reference wave and the beam scattered by the sample. If the differential path between the two waves is larger than their temporal coherence lengths, then the fringe contrast may drop dramatically and would consequently damage the spatial resolution or would even prevent the object reconstruction. Here, we have shown that the HHG source have all the spatial and spectral coherence properties suitable for multi-wavelength or attosecond coherent imaging.

We have described the steps from monochromatic to multi-wavelength coherent imaging. The monochromatic imaging can be constrained by a serious requirement, to keep the intrinsically large spectrum of such ultra-fast source throughout the imaging system. However, the multi-wavelength imaging allows to access the broadband dynamics of an object.

First, the spectral separation is controlled in the discrete reconstruction plane using the distance object - reference  $\bar{r}_0$ . This determines an important experimental constraint. To avoid spectral overlap between reconstructions, the separation  $\bar{r}_0$  has to increase proportionally to the total size of the object, and inverse proportionally to the spectral separation between the discrete wavelengths ( $\lambda_m - \lambda_n$ ). Therefore, the larger the distance  $\bar{r}_0$  is, the larger the focal spot needed to illuminate the sample is required. This generates a reduction of the flux of photons while the number of photons incident on the sample is a crucial parameter to ensure a good spatial resolution. A solution proposed is to use a two HHG beams configuration, one illuminating the sample and a second illuminating the holographic reference. The principle is similar to the one exposed as a perspectives of the stereo imaging in Chapter 3.

Second, the broadband overlapped reconstruction, presented in this chapter, describes the possibility to implement continuous broadband holographic imaging with an attosecond temporal resolution. For this, an isolated attosecond pulse is needed. CDI and holography usually require a monochromaticity factor that does not exceed  $10^{-2}$ . Note that a 100 as pulse requires a relative spectral width  $\Delta E/E$  of about 1/5 at 30 nm and 1/15 at 10 nm (these operating wavelengths are quite standard for attosecond sources), while  $\Delta E/E$  for one harmonic varies between  $10^{-3}$  to  $10^{-2}$ , depending on the driving laser spectral width. Then

two basic constraints have been demonstrated. The large spectrum generates an asymmetric blur effect around the central reconstruction (associated to  $\bar{\lambda}$ ). The minimization of this blur factor can be made using the minimum distance  $\vec{r}_0$  that is given by the broadband holographic condition. From the blur factors presented in this chapter we can see that the blur increases proportionally to the bandwidth  $\Delta\lambda$  but with the inverse of the minimum wavelength  $\lambda_1$ . Note that next generation attosecond sources operating around 1nm will have spectral width below  $10^{-2}$  that would directly allow working with standard lensless imaging techniques.





---

## PERSPECTIVES

---

### **Measurement of the coherence of the VUV emission assisted by nano-plasmonic field enhancement: HHG or plasma emission?**

The generation of high-harmonic radiation is one of the most exciting and promising areas of research in ultrafast optics and strong field laser physics. The ability to produce coherent radiation in the XUV (1 – 100 nm) as well as the possibility to generate attosecond light pulses have opened up new research areas. HHG relies mostly on Ti:Sapphire amplifier lasers as the generation process requires driving intensities in the  $10^{13} - 10^{14}$  W/cm<sup>2</sup> range. As a result, some major limitations exist for many academic and industrial applications, e.g., repetition rates limited to a few kHz and high acquisition and maintenance costs. In a completely different area of research, focused mainly on near-field imaging and Raman spectroscopy, scientists have been working for years on techniques using plasmonic resonances to achieve local enhancements of electric fields at the nanometer scale. In this context, the idea of using bowtie antennas made from gold has shown to hold a lot of potential. Such nanostructures have plasmonic resonances corresponding to an optical wavelength typically in the range 700 – 1000 nm and allow for field enhancement when resonantly excited. Until recently, there was no link between the strong field physics and this particular field of nanophysics. In 2008, Kim et al. combined these two scientific fields in a novel and stunning approach to generate high-harmonic radiation at a repetition rate of 75 MHz [46]. By focusing laser pulses from a standard femtosecond oscillator with pulse energy of 1.3 nJ onto a gold nanostructure (see inset in Fig. 5.1), they were able to achieve field enhancement by more than a 1000 factor. This enhancement is so efficient that even the moderate intensities achievable by a laser oscillator allow for the generation of XUV radiation in argon. The authors measured frequencies up to the 17<sup>th</sup> harmonic of the fundamental field, i.e., spectrum extending below 50nm which indicates a field enhanced intensity of  $\sim 5 \cdot 10^{13}$  W/cm<sup>2</sup> Fig.5.1 (a). This work was a first proof-of-principle experiment.

Recently, the group of Ropers [84], using nearly identical conditions as Kim et al., stud-

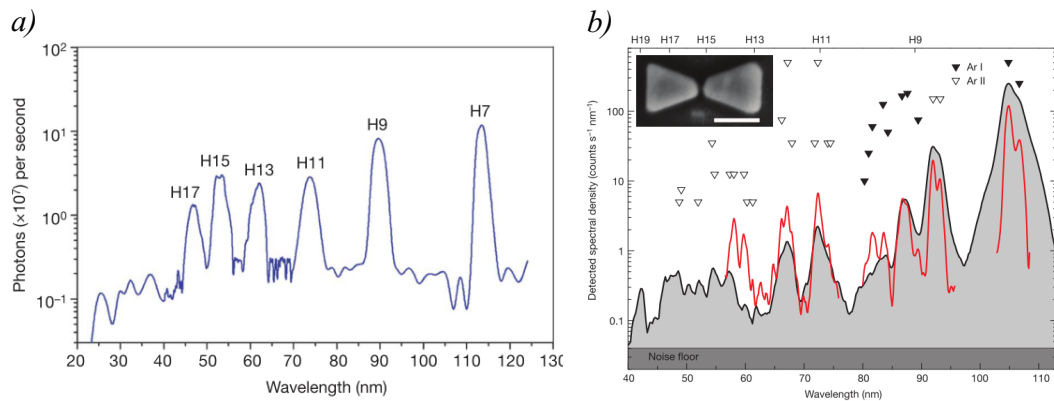


Figure 5.1: a) Measured spectrum by the group of Kim [46].  $H7, H9, H11, H13, H15, H17$  were identified. b) Results from Sivis et al. [84]. Detected spectral density (solid black line). Second grating diffraction order (solid red line). The emission corresponds to atomic line emission from neutral (Ar I; filled triangles) and singly ionized (Ar II; open triangles) argon. Wavelengths expected for HHG are shown in the upper x-axis.

ied the emission from atomic xenon confined in a plasmon-enhanced laser field. They observed EUV emission from the gas-exposed nanostructures, but came to the entirely different conclusion that harmonic generation was not the source of the emission. Instead, they attributed emission lines to radiative decay in neutral and ionized atoms (Fig. 5.1 (b)). Pushing their progresses, the Korean group developed a new funnel waveguide in 2011, which allows 3D coupling of the laser to the plasmonic field [68]. The funnel waveguide has been shown to allow for clear, stable and consistent generation of high harmonics up to  $43^{rd}$  order in xenon with reasonable optical and thermal damage.

The results of Sivis et al. [84] opened then the controversy, is it or not possible to have HHG using the field enhancement induced by resonant plasmons? One evidence of HHG can be given by the measurement the spatial properties of the radiation which has never been measured. This should indicate the coherent nature of the process, i.e. high harmonic generation. The interaction length along the laser propagation axis is restricted to a few nanometers so that each nanostructure acts as a point-like source to generate harmonics radiation. In the far field, the spatial profile is a coherent superposition of the individual EUV nano-sources: this gives an undisturbed view into the microscopic response and possibly measurement of "single-atom" harmonic spectrum.

Let us recall the fundamental aspects of the plasmonic nanostructures/laser light interaction. Briefly, in metal and non-metallic nanostructures, excitation by light at infrared to visible frequencies often produces coherent oscillations of surface charge density on the nanostructures called localized surface plasmon (LSP) resonances and generates an electric field as shown in Fig. 5.2. The plasmonic field adds to the light field, resulting in a stronger interaction between the field and the medium but in a small spatial region. Plas-

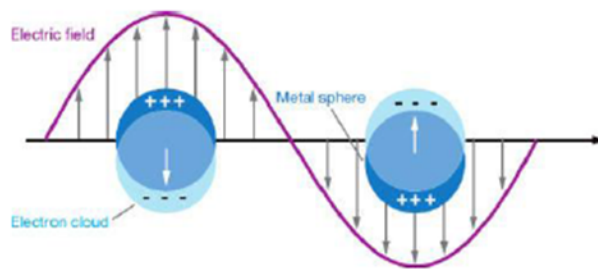


Figure 5.2: When submitted to an electric field the electric charges within a metallic nanostructure start to oscillate and generate an additional electric field.

monic nanoparticles are important in a broad variety of applications, including surface-enhanced Raman spectroscopy, solar energy production, biomedical and chemical sensing, and even tumor detection and treatment. These applications lie in the low intensity regime. However, LSP resonances can boost up the intensity level by more than 3 orders of magnitude. This enhancement offers the possibility of accessing the strong field regime, i.e., above  $10^{13}\text{W}/\text{cm}^2$  where atoms can be ionized, directly by using moderate femtosecond laser pulses emitted from an oscillator with intensities of  $0.1\text{--}1\text{ TW}/\text{cm}^2$ . Without the need for chirped pulse amplification, the plasmon driven strong field draws attention as a promising method to produce coherent soft X-rays by high order harmonic generation at a MHz repetition rate. Besides, the plasmonic field enhancement is narrowly localized in a sub-wavelength spot size which could be useful for innovative targeted nanoscale applications. Finally the dynamics of the plasmonic excitation takes place on attosecond time scales over distances of around 10 nm or less. Hence potentially a spatio-temporal resolution down to the single atom and attosecond range appears to be possible.

In a collaboration with the group of Milutin Kovacev at Hannover University in Germany we proposed to characterize the spatial coherence of the EUV radiation generated by field enhancement in similar conditions to the generation setup of Kim et al. [46]. I have been working on simulating the far emission of the radiation and setting up the experimental design for measuring the coherence from the measurement of the far field field emission. The techniques basically rely on the method of spatial coherence characterization presented in Chapter 1 to corroborate if the XUV radiation is coherent (HHG) or incoherent (line emissions). Due to the size of the individual EUV nano-sources, the divergence of the beam is extremely high, above  $120^\circ$ . The far field should exhibit similar feature as a coherent diffraction pattern or a hologram. Simulations are shown in Fig. 5.3 for a single harmonic ( $13^{\text{th}}$ ). The observation of interferometric modulation should give a clear signature of the coherence of the generation process. Furthermore, by using a coherent diffractive imaging or a holographic scheme, we will reconstruct the complete spatial amplitude and phase distri-

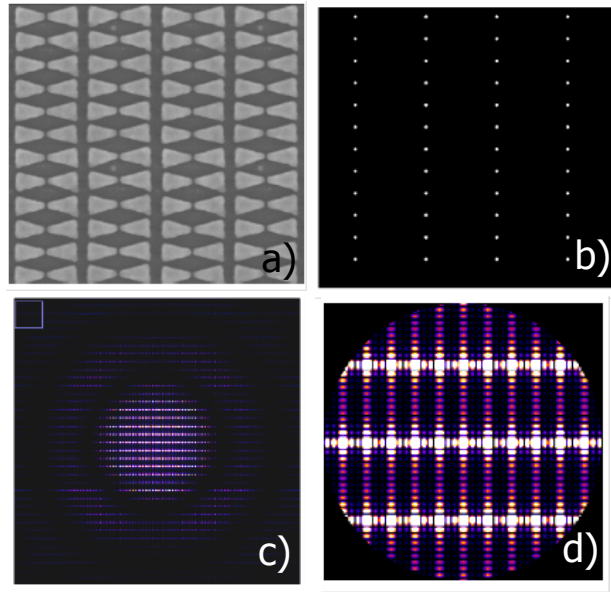


Figure 5.3: (a) SEM image of a typical bow tie array. (b) Distribution of 20nm size HHG sources calculated from (a). (c) Far field emission of the HHG sources array shown in (b). The calculations are performed for harmonic 13<sup>th</sup>. The CCD detector is located 2 cm after the bowtie array. (d) Zoom of the first Airy disk which shows modulation from the interferences of the mutually coherent HHG sources.

bution of the harmonic EUV nano-sources revealing the localization and strengths of the plasmonic fields.

However, the HHG spectrum is a comb of odd frequencies of the driving IR laser. We have also performed the simulation for the multi-wavelength case (using the simulation tools developed in Chapter 4). The results for harmonics 11<sup>th</sup> to 17<sup>th</sup> generated in xenon are presented in Fig. 5.4. We clearly see the interferometric modulations showing the spatial coherence related to the HHG process. Other features in Fig. 5.4 correspond to the frequency beating between harmonics. Interestingly, we can extract the spectrum from the diffraction pattern as the sample acts as a diffraction grating. The harmonic spectra can be extracted from several diffraction orders as shown in Fig. 5.4 (right image). Here, a multi-wavelength phase retrieval can be used to retrieve the nano-plasmonic HHG source distribution.

The Fourier transform of the multi-wavelength diffraction pattern (Fig. 5.5 (b)) represents the autocorrelation of a redundant array of point-like sources scaled at the different wavelengths of the spectrum. As we saw in Chapter 1, each pair of sources  $(n,m)$  will generate a peak in the Fourier transform. The amplitude of each peak  $C_{nm}$  is proportional to the intensity of each point-like source  $(n,m)$  and to the degree of coherence  $\mu_{nm}$ . Therefore, from the structures of peaks in the Fourier transform of the diffraction pattern (Fig. 5.5 (b)) it is possible to determine if the XUV field is coherent or not.

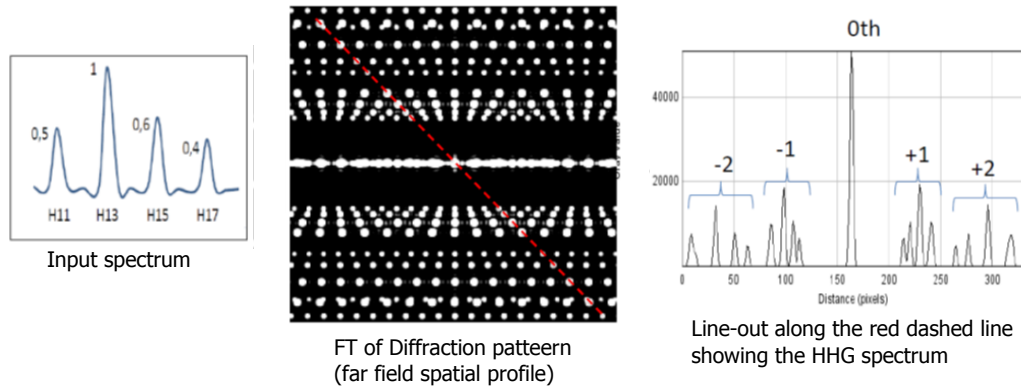


Figure 5.4: Simulation of the multiwavelength case. We consider here the HHG spectrum generated in xenon and transmitted through a 150 nm aluminum filter which cuts the lower harmonic orders. Left: spectral profile of the light going to the CCD detector. Middle: Spatial profile calculated 2 cm after the source. Right: plot profile along the red axis shown in the far field spatial profile. We see the first and second diffraction orders of the harmonic spectrum.

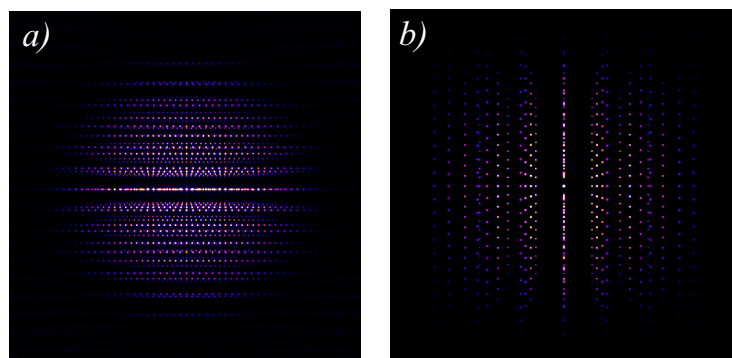


Figure 5.5: a) Simulation of the diffraction pattern generated with the spectrum of Fig. 5.4. b) Fourier transform of the diffraction pattern.

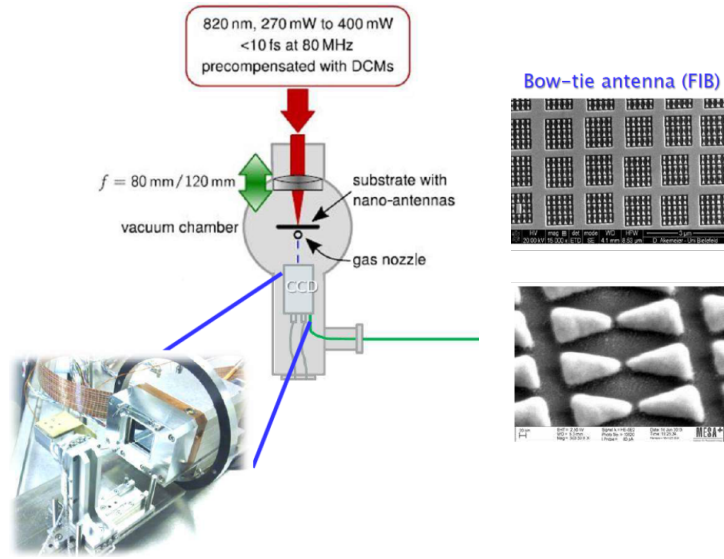


Figure 5.6: Left: experimental setup for the measurement of the far field emission of the HHG assisted by nanoplasmonic field amplification. Right-up: Array of bow-tie antenna produced using a focused ion beam (FIB). Right down: Zoom of 3 bow-tie antenna. The gap between two antenna is of 20 nanometers.

The very first results of the experiments have been obtained while writing this manuscript. We collect the light using a  $28 \times 28\text{ mm}^2$  CCD camera located as close as 20 to 30 mm from the source (Fig. 5.6).

Fig. 5.7 below shows the diffraction pattern measured with a Xenon gas target. Two aluminum filter of 160 nm thickness each (LUXEL company) are set before the CCD to filter out the infrared radiation. One issue in collecting the data has been the radiation damage of the sample so that we could not get signal accumulation over 5 minutes exposure time. The data taken over 60s accumulation time are shown in Fig. 5.7. The far field with gas shows a spot that could be attributed to VUV emission (HHG or plasma). We also see that this spot stands on a strong background emission. The Fourier transform (right image) shows vertical lines which could be attributed to interferometric modulation from a coherent source. To investigate the origin of these modulations we have taken data without gas. The far field emission does not show any spot but only the background signal (similar to the background with gas). The Fourier transform of the far field shows exactly similar vertical lines as the case with gas. Apparently those lines come from the infrared radiation that still goes through the aluminum. Indeed, even with a transmission of  $10^{-8}$  there is enough light emitted by the femtosecond laser oscillator to induce some background signal on the CCD.

In conclusion, we have obtained the very first indication of VUV emission assisted by plasmonic field enhancement using and array of bow tie antennas. We do not see any

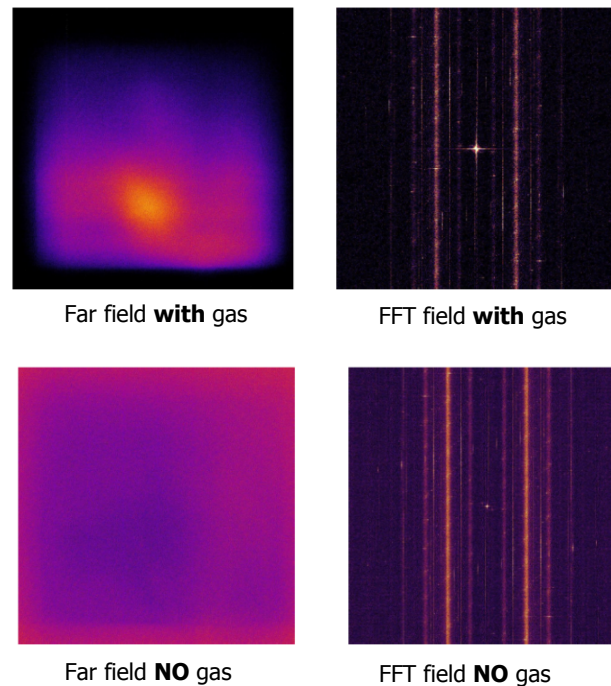


Figure 5.7: Far field emission measured by our soft X-ray CCD camera. Left up: with xenon gas. Right down: without gas. Right up and down: Fourier transform of the far field emission.

evidence of the coherence of the process as the signal is too weak. Infrared radiation is seen and exhibits structures that could be related to the far field interferences produced by the support of the array of bow tie antennas (and not the bow ties themselves as they are much smaller than 800nm radiation wavelength). The analysis is undergoing. The experiment continues in 2015 using thicker filters to remove totally the IR. Another progress will be to change the gas injection setup to increase the gas pressure by at least two orders of magnitude. Consequently, the number of HHG emitters should also increase. We will also use indium and tin filters that will select only two harmonics (instead of 4 – 5 with an aluminum filter) the 9<sup>th</sup> and 11<sup>th</sup> (indium) or 11<sup>th</sup> and 13<sup>th</sup>.

---

### Time resolved nanoscale imaging with multiple harmonic wavelengths

While intuitively one could think that a monochromatic illumination of the sample is needed for coherent diffractive experiments, we have shown that lensless imaging using a broad multi-wavelength spectrum on simple test objects is possible (see Chapter 4). Further experiments are however needed to improve the quality of the images. The goal is to use the technique in a pump-probe configuration. Indeed, large broadband probing of



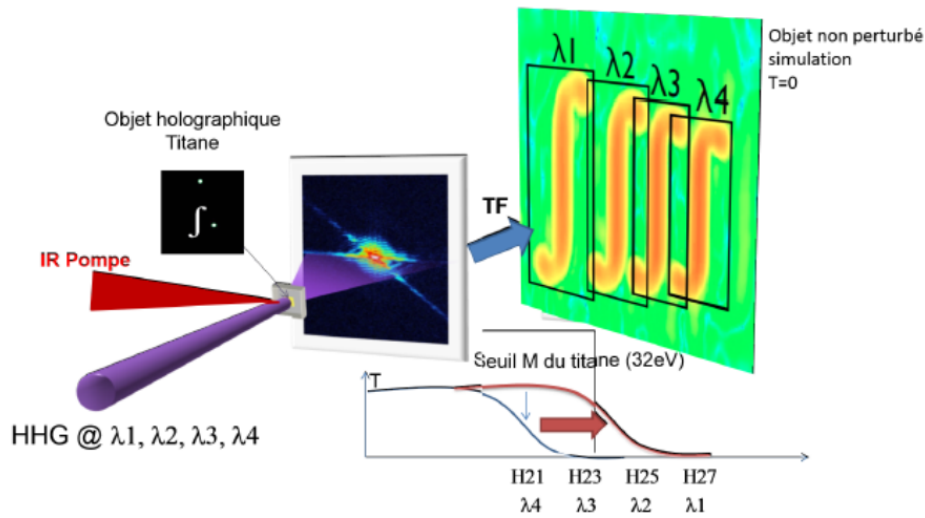


Figure 5.8: Sketch of the experimental setup for IR pump - soft X-ray probe plasma dynamics via multi wavelength imaging.

the soft-X-ray optical index of matter is of high potential for resolving concrete problems in various scientific areas from physics (magnetism, phase transition, plasma, ...) to biology (water window imaging, element selective spectro-imaging, ...). A multi-wavelength soft X-ray probe allows for example measuring the property of a material above and below a specific transition edge simultaneously within the same sample. Finally, let us mention as a potential application that such broadband spectrum would allow attosecond imaging.

As a perspective of the work presented in Chapter 4, the CEA group will conduct in spring 2015 a multiwavelength imaging experiment to probe the dynamics of a nanoplasma. At a nanometer scale, the properties and evolution of a plasma can be influenced by its confinement (field enhancement effect for example, absorption resonances, ...). Let us consider harmonics that lie above and below the titanium M-edge located at an energy of 32 eV (this corresponds to harmonic 21). The holographic sample is composed of a thin titanium foil with a nanoscale design and a reference (Figs. 5.10 - 5.11). The harmonic beam illuminates the sample and the diffraction is detected using a soft X-ray CCD camera. The Fourier transform of the diffraction pattern should reveal the image of the nanoscale design at each probing wavelength (Fig. 5.8). The separation of these reconstructions depends on the position of the holographic reference. We have calculated that if the nanoscale design is in a box of  $1 \mu\text{m} \times 1 \mu\text{m}$  then the reference should be at least at  $13 \mu\text{m}$  away from the box to avoid the overlap of the images reconstructions at each harmonic wavelength.

What happens if the titanium foil is heated using an infrared laser at an intensity of about  $10^{14} \text{ W/cm}^2$ ? The laser energy deposited into the foil will create a plasma. During the heating, the position of the M-edge will radically shift to higher energy. As a consequence

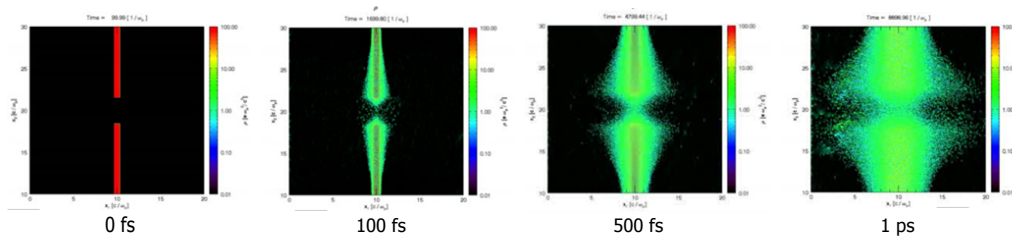


Figure 5.9: Simulations of the titanium expansion. The code allows tracing the proton density in free vacuum. Left: sample before laser heating. The two red rectangles are titanium wires of 200 nm width. The distance between them is of 1  $\mu\text{m}$ . left to right: proton density at 100 fs, 500 fs, 1 ps after laser heating.

the harmonics that are located above the M-edge will start to be transmitted by the sample. At the same time the plasma will expand. The clear image reconstruction obtained before heating should then be blurred as the time delay increases. The multi-wavelength nanoscale imaging should also show the nano-plasma collision that will occur in the vacuum inside the slits included in the sample design. The plasma expansion happens at a speed of 1 nm/fs. The design of the sample will consist in groove of 1  $\mu\text{m}$  width so that the collision should occur at a delay of about 500 fs. Let us mention that the temporal resolution that can be reached with our experimental design is of 20 fs (limited by the pulse duration of a single harmonic). This should allow observing the very early stage of the plasma heating together with the nano-plasma collision and plasmonic field enhancement effects.

The PIC simulations shown in Fig. 5.9 reveal the fast expansion of the plasma. The simulation was performed using two titanium wires separated by a distance of 1  $\mu\text{m}$ . Already, 100 fs after the laser heating we see that the wires expand. This expansion is extremely fast so that at a delay of 500 fs the fastest protons have been traveling almost 500 nm away from the target. This should be observable with our ultrafast holographic probe. 1 ps after the laser heating we observe that the expansion is mainly lateral and we do not see the plasma collision between the two wires. Further simulations are undergoing with another sample geometry in order to get a higher confinement of the plasma. This should facilitate the plasma collision. Additionally, we should observe a heating enhancement at the early stage of the process by the plasmonic resonance induced by the nanoscale confinement of the target. Fast protons should be ejected at this early stage (simulations not shown here).

One of the issues is to achieve single shot imaging. Indeed, it will be difficult to accumulate over many shots as fluctuation of the plasma dynamic might blur the holograms. The sample should be renewed for each shot and even if we can ensure a good reproducibility of the sample design, other parameters such as infrared laser or harmonic beam energies, pointings, shapes, wavefronts, etc... will vary. We have developed a new holographic scheme to enhance the signal to noise ratio. We will use multiple references. All the re-

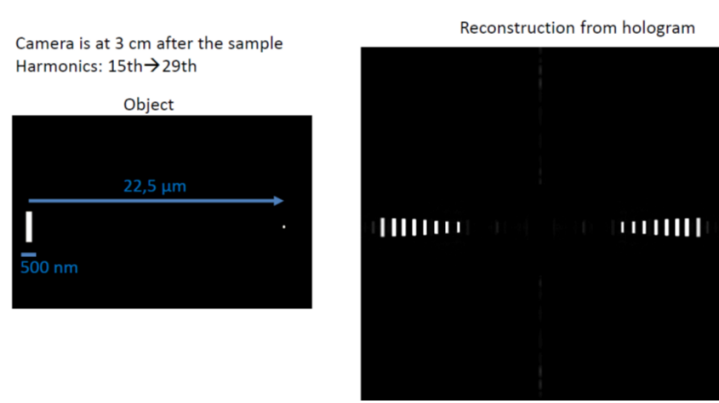


Figure 5.10: Simulation of the image reconstruction for a broad harmonic spectrum from H15 to H29. The holographic distance ( $22.5 \mu\text{m}$ ) is large enough to ensure a separation for the images obtained at each wavelength.

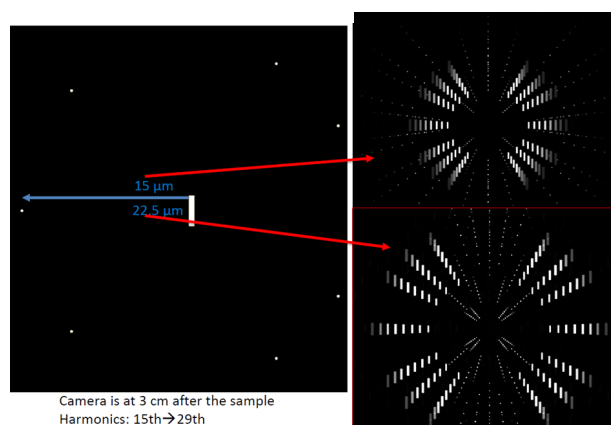


Figure 5.11: Simulation of the image reconstruction for a broad harmonic spectrum from H15 to H29 and 7 holographic references. The holographic distances are  $15 \mu\text{m}$  and  $22.5 \mu\text{m}$ .

construction can be added in amplitude and in phase, the phase being a very important parameter to enhance the image quality [32].

Figure 5.10 below shows the basic principle with one reference and figure 5.11 with 7 references. In Fig. 5.10, the reference is located at a distance of  $22.5 \mu\text{m}$ , the simulation shows a clear separation of the object images obtained for harmonics from  $15^{\text{th}}$  to  $29^{\text{th}}$ . Those harmonics have been chosen to simulate the HHG spectrum generated in argon and transmitted through an aluminum filter. The separation is large enough to observe a plasma expansion of twice the sample size.

Figure 5.11 shows simulation with the same HHG parameters but with a holographic design with 7 references and two holographic separations  $15 \mu\text{m}$  and  $22.5 \mu\text{m}$ . For a distance of  $15 \mu\text{m}$ , the sample image reconstructions are separated except for the one reference hole

(up, left) where the highest harmonic orders reconstructions start to overlap. This might be critical for a pump probe experiment where the plasma expansion will occur in a box that will be at least two times larger than the sample size. However this might not be enough as the plasma expansion shown in the simulation should be hold in a box of at least 5 times the sample size. This means a holographic separation of about  $100 \mu\text{m}$ . This would then generate experimental constraints as for example the homogeneous illumination of all the reference. A new setup with two HHG sources would be then more suitable.

In conclusion, we have shown a very original perspective of the multi-wavelength imaging technique presented in Chapter 4 . This powerful method should allow to spectrally resolved the plasma dynamics at a nanometer scale and with a femtosecond temporal resolution. Other application in magnetism and biological imaging are also envisaged.



# CONCLUSIONS

---

The objective of this thesis was to study new XUV imaging techniques in single shot, towards the development of new applications using HH and FEL sources. The work presented in this thesis was divided in two parts; the first is focused on the characterization of the sources and the second on the development of new imaging techniques. Some applications and perspectives of this work have also been presented.

In **Chapter I** a new single shot technique of spatial coherence characterization was proposed and validated using HH sources. This technique allows studying the spatial coherence without any intensity measurements. We have first presented the simulations which show the feasibility of single shot coherence measurement using a non-redundant array of apertures. These apertures can be set in such a way that they sample the coherence at various distances. This works only under the assumption of shift invariance which is quite reasonable and realistic. This is quite advantageous compared to other techniques such as Young two slits interferometry technique. Note that this later requires that the intensity on each slit is equal. This is not the case for the non-redundant array which does have any a priori requirements on the intensity distribution.

The error induced in terms of pointing stabilization was studied using simulations. The shot to shot variation of the intensity distribution induces an error in the measurement even if the intensity at each aperture is measured. Usually, in other methods, only the information of the intensity variation from shot to shot could avoid this measurement error. Here, the simulations demonstrate that the NRA technique in single shot eliminates the error induced by pointing stabilization. We have then studied the case where the signal is accumulated over many shots. Errors can be minimized by measuring the intensity variation as in all the techniques. However, without knowledge of the intensity, we have demonstrated that the NRA technique induces a smaller error than the Young interferometry technique.

We have validated these simulations by performing measurements of the spatial coherence of harmonic 33 of the LUCA laser facility operating at 800nm. The experiment is in good agreement with the simulations showing a Gaussian behavior for the two generating conditions used in the experiment. This opens perspectives for the coherence studies on HHG or FEL sources. However, as fluctuation from shot to shot may alter the results, single shot measurements are more suitable.

We presented the extent of the multiple apertures method from the far field case to the intermediate field. This can be useful for sources like FEL where the beam cannot always be accessible at end-station. A quadratic term of phase modulates the correlation between the different pair of apertures. This term has to be corrected to extract the spatial coherence measurement from the Fourier transform of the intermediate diffraction plane.

Finally, the relation between image reconstruction and spatial coherence of the source was studied in the case of Fourier transform holographic imaging. We presented the deduction of an analytical expression for the Fourier transform reconstruction with a partially coherent beam. From this description we can see that any modulation in the object reconstruction induced by a shift invariant phase of the spatial coherence is avoided by using the FTH with a point-like reference. In the case of an extended reference, shift variations of the phase in the spatial coherence may generate a superposition out of phase in the object reconstruction. This can degrade the object reconstruction. As a perspective of this work we plan to study the effect of the derivative algorithms for FTH imaging with extended sources in terms of the spatial coherence.

**Chapter II** presents experimental results of wavefront sensing in the XUV range. Using a commercial Hartmann wavefront sensor the focusing system of our harmonic beamline was optimized. The focal spot was reduced improving in this way the flux of photons in an area of  $5 \mu\text{m}^2$  which is now typical in our imaging experiments. The aberrations present in the phase of the source (and induced by our focusing system) were reduced from an RMS error of  $\sim \lambda/3$  up to  $\sim \lambda/6$ .

We have then applied this technique to characterize the wavefront and the focusing of the soft X-ray beam of different FEL facilities. An experimental campaign has been conducted at the AMO station at the LCLS free electron laser. The goal was to optimize in real time the focusing system. We have shown in this manuscript that the wavefront sensor allows getting high order aberrations terms which are not be easily corrected using the standard PMMA technique. In particular we see a visible reduction of the coma aberration after alignment with the wavefront sensor. The total RMS wavefront error was reduced from  $5.4\lambda$  down to  $4.8\lambda$  with  $\lambda = 2.26 \text{ nm}$ . The remaining aberration was induced by a carbon deposition on the K-B system.

At FERMI@Elettra, the K-B focusing system has been optimized to a value close to the limit of the mechanical system. By following the wavefront measured with the XUV Hartmann sensor as a feedback, the KB mirrors were bended to reduce the aberrations. The focal spot was optimized from  $26 \mu\text{m} \times 15 \mu\text{m}$  down to  $5 \mu\text{m} \times 8 \mu\text{m}$ . This is much better than what has been obtained using standard techniques of focusing via PMMA imprints. Additionally the FEL emission mode has been studied showing the generation of a particular X-ray beam composed by two main modes, a nearly-Gaussian central peak and an annular one. The generation process of such a mode is well known [49] but there are different mechanism to generate it. This result opens the perspective of studying the different generation

mechanism by following the wavefront measurements.

We have used the wavefront sensing technique in a pump probe experiment at the Matter under Extreme Condition End-station at LCLS. We have demonstrated in a flexible pump-probe scheme that the HHG wavefront can be used as an ultrafast diagnostic of the optical and structural properties of a dense plasma. Here we use, for the first time, high harmonic generation from optical lasers to create an ultrashort soft X-ray pulse to probe solid aluminum or titanium heated by an XFEL pulse, revealing the theorized effect of lattice order on the extreme ultra-violet (EUV) optical properties. Probing with XUV pulses created by high harmonic generation (HHG), for which solid density is undercritical, allows the measurement of the XUV refractive index with unprecedented time and spatial resolution. By heating a solid target (aluminum, titanium) with a short (60 fs) XFEL pulse, the heating of the electrons and ions, which are individually complex processes, are naturally separated in time. The analysis of the wavefront plasma induced distortions is still under process. Additionally to these measurements, absorption measurements of the harmonics were performed. The results show unambiguously the effect of the heated electron distribution and crystal lattice order over the relevant timescales (up to 25 ps), and that increase in opacity in the wavelength range used in this study is nearly entirely due to loss of crystal order causing increased absorption up to a few picoseconds, and that the heated electron distribution has a relatively minor effect.

In **Chapter III** we presented the work conducted through the development of a HH imaging beamline to extend our previous 2D ultrafast nanoscale imaging techniques to obtain 3D images. Indeed, most samples of physical interest require 3D perception. However, the usual method based on many orientation projections of the specimen suffers from extended exposure time to X-rays which could induce damages. Ultrafast single shot 3D stereo imaging allows lowering the impact of X-ray exposure. Moreover, when dynamics are studied, the single shot regime is mandatory: some phenomena are not reversible and solid state samples are often not perfectly reproducible. Stereo imaging is based on human vision. Our right and left eyes take two 2D images at different observation angles of the object and the brain combines these images to give the perception of 3D depth.

I have been working in the implementation of two different experimental solutions for the 2 sources stereo setup using high harmonic generation. The first idea was to realize two parallel beams before focusing using off axis parabola. The separation of the main beam is realized with two grazing incidence silicon mirrors before the parabolic mirror. Half of the harmonic beam is reflected and the other half goes straight to the parabola. The reflected half-beam is then reflected by a second multilayer mirror toward the parabola. The two half-beams are focused by the parabola onto the sample. This first solution confirmed the possibility of capturing two diffraction patterns with the CCD camera at the same time. Moreover, the parabola size limits the maximum distance between the incoming beams which can induce an overlap of the two diffraction patterns. As a consequence, the spatial



resolution was restricted by the overlap between the two diffraction patterns on the detector. Note also that in this geometry the two beams are not synchronized. A new setup with a femtosecond synchronization of the two beams has then been designed.

A second stereo lensless imaging setup was proposed. This setup splits the beam after the off axis parabola by using a prism and two mirrors recombines the beams at focus. The angle between and the temporal synchronization of the two beams was controlled by adjusting the position of the mirrors. This setup has shown to be more flexible than the previous one. We were able to scan over various stereo angles. We have optimized the distance between the two diffraction patterns on the CCD camera avoiding the overlap. This allowed us to reach much higher spatial resolution. A future development will be to introduce a double cell setup to increase the photon flux to achieve single shot imaging.

In **Chapter IV** we presented the extension of holographic imaging techniques to discrete broadband multi-wavelength soft X-ray sources. Spectrally resolved image reconstructions were experimentally demonstrated. This work demonstrates a holographic technique which allows the use of such sources in a Fourier transform holographic scheme. The technique employs careful placement of the reference aperture, which allows image reconstruction with a single 2D Fourier transform of the hologram, and no iterative image retrieval methods. In Fourier Transform Holography (FTH), the hologram is formed by the diffraction pattern of the reference and object pair. Reconstruction of the image is achieved by a 2D Fourier transform of the digital hologram, which yields a convolution of the object reference pair in the image plane, yielding the image of the object if the reference is a point source. The technique is versatile, and with the correct considerations, can be adapted to low-signal target designs such as the use of extended references, or even more complex reference geometries. With a pinhole reference, the object appears at the distance of the pinhole relative to the object,  $\vec{r}_0$ , in the image. The real space scaling of the image pixels is dependent on the wavelength, so different wavelengths will have a different number of pixels for the same distance,  $\vec{r}_0$ , in the image plane, separating the images in space. The degree of this separation is directly proportional to  $\vec{r}_0$ . For large reference-object distance we propose to use a double HHG source setup, i.e. similar to the one exposed as a perspectives of the stereo imaging in Chapter 3. For imaging using non-discrete broadband XUV sources, such as those supporting isolated attosecond pulses, an interference pattern consisting of a single characteristic spatial frequency can be recorded when the reference position is chosen correctly, albeit at the cost of spatial resolution. This work demonstrates a relatively simple technique to obtain 100 nm scale spatially resolved image using broadband XUV pulses with a discrete or continuous spectrum, that can support trains or isolated attosecond pulses, highlighting possible future applications for the imaging of attosecond timescale electronic or magnetic phenomena in nanometer-scale features in solid-state materials.

# REFERENCES

---

- [1] Abbey B, Whitehead LW, Quiney HM, Vine DJ, Cadenazzi GA, Henderson CA, Nugent KA, Balaur E, Putkunz CT, Peele AG, Williams GJ, and McNulty I. *Lensless imaging using broadband X-ray sources*. Nature Photonics **5**, 420–424 (2011).
- [2] Alonso MA. *planar obstacles in the Wigner representation*. America **26**, 1588–1597 (2009).
- [3] Andrulleit H, Geisen M, and Stäger S. *Stereo-microscopy of coccolithophores - modern applications for imaging and morphological analysis*. Journal of Nannoplankton Research **28**, 1–16 (2006).
- [4] Attwood D. *Soft x-rays and extreme ultraviolet radiation: principles and applications*. Cambridge University Press (2000).
- [5] Baker KL. *X-ray wavefront characterization with two-dimensional wavefront sensors: shearing interferometers and Hartmann wavefront sensors*. Optical Engineering **52**, 026501 (2013).
- [6] Barty A, Boutet S, Bogan MJ, Hau-Riege S, Marchesini S, Sokolowski-Tinten K, Stojanovic N, Tobey R, Ehrke H, Cavalleri A, Düsterer S, Frank M, Bajt S, Woods BW, Seibert MM, Hajdu J, Treusch R, and Chapman HN. *Ultrafast single-shot diffraction imaging of nanoscale dynamics*. Nature Photonics **2**, 415–419 (2008).
- [7] Barty a, Marchesini S, Chapman HN, Cui C, Howells MR, Shapiro Da, Minor aM, Spence JCH, Weierstall U, Ilavsky J, Noy A, Hau-Riege SP, Artyukhin aB, Baumann T, Willey T, Stolken J, van Buuren T, and Kinney JH. *Three-dimensional coherent x-ray diffraction imaging of a ceramic nanofoam: determination of structural deformation mechanisms*. Physical review letters **101**, 055501 (2008).
- [8] Bates RHT. *Fourier phase problems are uniquely solvable in more than one dimension. I: Underlying theory*. Optik **61**, 247–262 (1982).
- [9] Bellini M, Lyngå C, Tozzi A, and Gaarde M. *Temporal coherence of ultrashort high-order harmonic pulses*. Physical Review Letters pages 297–300 (1998).
- [10] Chalupský J, Krzywinski J, Juha L, Hájková V, Cihelka J, Burian T, Vyšín L, Gaudin J, Gleeson A, Jurek M, Khorsand AR, Klinger D, Wabnitz H, Sobierajski R, Störmer M, Tiedtke K, and Toleikis S. *Spot size characterization of focused non-Gaussian X-ray laser beams*. Opt. Express **18**, 27836–27845 (2010).
- [11] Chapman HN and Nugent Ka. *Coherent lensless X-ray imaging*. Nature Photonics **4**, 833–839 (2010).
- [12] Chapman HN, Barty A, Bogan MJ, Boutet S, Frank M, Hau-Riege SP, Marchesini S, Woods BW, Bajt S, Benner WH, London Ra, Plönjes E, Kuhlmann M, Treusch R, Düsterer S, Tschentscher T, Schneider JR, Spiller E, Möller T, Bostedt C, Hoener M, Shapiro Da, Hodgson KO, van der Spoel D, Burmeister F, Bergh M, Caleman C, Huldt G, Seibert MM, Maia FRNC, Lee RW, Szöke A, Timneanu N, and Hajdu J. *Femtosecond diffractive imaging with a soft-X-ray free-electron laser*. Nature Physics **2**, 839–843 (2006).
- [13] Chapman HN, Hau-Riege SP, Bogan MJ, Bajt S, Barty A, Boutet S, Marchesini S, Frank M, Woods BW, Benner WH, London Ra, Rohner U, Szöke A, Spiller E, Möller T, Bostedt C, Shapiro Da, Kuhlmann M, Treusch R, Plönjes E, Burmeister F, Bergh M, Caleman C, Huldt G, Seibert MM, and Hajdu J. *Femtosecond time-delay X-ray holography*. Nature **448**, 676–9 (2007).
- [14] Chen B, Dilanian Ra, Teichmann S, Abbey B, Peele AG, Williams GJ, Hannaford P, Van Dao L, Quiney HM, and Nugent Ka. *Multiple wavelength diffractive imaging*. Physical Review A **79**, 023809 (2009).
- [15] Chini M, Zhao K, and Chang Z. *The generation, characterization and applications of broadband isolated attosecond pulses*. Nature Photonics **8**, 178–186 (2014).
- [16] Cho S, Alonso Ma, and Brown TG. *Measurement of spatial coherence through diffraction from a transparent mask with a phase discontinuity*. Optics letters **37**, 2724–6 (2012).
- [17] Cho S, Brown TG, and Alonso Ma. *Simple methods for measuring spatial coherence and their relation to the Wigner function*. 2012 11th Euro-American Workshop on Information Optics pages 1–3 (2012).
- [18] Corkum PB. *NoPlasma perspective on strong field multiphoton ionization*. Physical Review Letters **71**, 1994–1997 (1993).

- [19] Cundiff ST. *Femtosecond combs: Simplified stabilization*. *Nature Photonics* **4**, 410–411 (2010).
- [20] Deroff LL, Salières P, and Carré B. *Temporal and spatial coherence of high order harmonics*. *Laser Physics* **10**, 294–302 (2000).
- [21] Dilanian Ra, Chen B, Williams GJ, Quiney HM, Nugent Ka, Teichmann S, Hannaford P, Dao LV, and Peele AG. *Diffraction imaging using a polychromatic high-harmonic generation soft-x-ray source*. *Journal of Applied Physics* **106**, 023110 (2009).
- [22] Drescher M, Hentschel M, and Kienberger R. *Time-resolved atomic inner-shell spectroscopy*. *Nature* **419**, 803–807 (2002).
- [23] Eisebitt S, Lüning J, Schlotter W, and Lörger M. *Lensless imaging of magnetic nanostructures by X-ray spectro-holography*. *Nature* **432**, 885–888 (2004).
- [24] F M. *No Title*. *Naturwissenschaften* **27**, 511–522 (1939).
- [25] Fang L, Hoener M, Gessner O, Tarantelli F, Pratt ST, Kornilov O, Buth C, Gühr M, Kanter EP, Bostedt C, Bozek JD, Bucksbaum PH, Chen M, Coffee R, Cryan J, Glowina M, Kukk E, Leone SR, and Berrah N. *Double Core-Hole Production in N<sub>2</sub>: Beating the Auger Clock*. *Phys. Rev. Lett.* **105**, 83005 (2010).
- [26] Ferray M, L’Huillier A, Li XF, Lompre La, Mainfray G, and Manus C. *Multiple-harmonic conversion of 1064 nm radiation in rare gases*. *Journal of Physics B: Atomic, Molecular and Optical Physics* **21**, L31–L35 (1988).
- [27] Fienup J. *Phase retrieval algorithms: a comparison*. *Applied optics* **21** (1982).
- [28] Fienup J. *Reconstruction of a complex-valued object from the modulus of its Fourier transform using a support constraint*. *JOSA A* **4**, 118–123 (1987).
- [29] Fienup JR. *Reconstruction of an object from the modulus*. *Opt. Lett.* **3**, 27–29 (1978).
- [30] Gabor D. *A new microscopic principle*. *Nature* **161**, 777–778 (1948).
- [31] Gauthier D. *Imagerie nanométrique ultra-rapide par diffraction cohérente de rayonnement extrême-UV produit par génération d’harmoniques d’ordre élevé*. PhD thesis, Université Paris Sud XI, Orsay, France, (2012).
- [32] Gauthier D, Guizar-Sicairos M, Ge X, Boutu W, Carré B, Fienup JR, and Merdji H. *Single-shot Femtosecond X-Ray Holography Using Extended References*. *Physical Review Letters* **105**, 093901 (2010).
- [33] Ge X. *Imagerie ultrarapide à l’échelle nanométrique par diffraction XUV cohérente*. Theses, Université Paris Sud - Paris XI, (2012). URL <https://tel.archives-ouvertes.fr/tel-00828058>.
- [34] Ge X, Boutu W, Gauthier D, Wang F, Borta A, Barbrel B, Ducouso M, Gonzalez AI, Carré B, Guillaumet D, Perdrix M, Gobert O, Gautier J, Lambert G, Maia FRNC, Hajdu J, Zeitoun P, and Merdji H. *Impact of wave front and coherence optimization in coherent diffractive imaging*. *Optics express* **21**, 11441–7 (2013).
- [35] Ge X, Boutu W, Gauthier D, Wang F, Borta A, Barbrel B, Ducouso M, Gonzalez AI, Carré B, Guillaumet D, Perdrix M, Gobert O, Gautier J, Lambert G, Maia FRNC, Hajdu J, Zeitoun P, and Merdji H. *Impact of wave front and coherence optimization in coherent diffractive imaging*. *Opt. Express* **21**, 11441–11447 (2013).
- [36] Gerchberg RW and Saxton WO. *Practical algorithm for determination of phase from image and diffraction plane pictures*. *Optik* **35**, 237 – 246 (1972).
- [37] González AI and Mejía Y. *Nonredundant array of apertures to measure the spatial coherence in two dimensions with only one interferogram*. *Journal of the Optical Society of America. A, Optics, image science, and vision* **28**, 1107–1113 (2011).
- [38] Goodman JW. *Statistical optics*. John Wiley and Sons, New York (1985).
- [39] Goodman JW. *Introduction to Fourier Optics*. McGraw-Hill Series in Electrical and Computer Engineering: Communications and Signal Processing. McGraw-Hill (1996). ISBN 9780070242548.
- [40] Goulielmakis E, Schultze M, and Hofstetter M. *Single-cycle nonlinear optics*. *Science* **320**, 1614–1617 (2008).
- [41] Guizar-Sicairos M and Fienup JR. *Holography with extended reference by autocorrelation linear differential operation*. *Optics express* **15**, 17592–612 (2007).
- [42] Hasegawa A. *Free Electron Laser*. *Bell System Technical Journal* **57**, 3069–3089 (1978).
- [43] Hentschel M, Kienberger R, and Spielmann C. *Attosecond metrology*. *Nature* (2001).
- [44] Jacobsen C and Rothman S. *X-ray holographic microscopy using photoresists*. *Journal of Optical Society of America A* **7**, 1847–1861 (1990).
- [45] Kienberger R and Goulielmakis E. *Atomic transient recorder*. *Nature* **427**, 817–821 (2004).
- [46] Kim S, Jin J, Kim YJ, Park IY, Kim Y, and Kim SW. *High-harmonic generation by resonant plasmon field enhancement*. *Nature* **453**, 757–60 (2008).

- [47] Kirz J and Jacobsen C. *The history and future of X-ray microscopy*. Journal of Physics: Conference Series **186**, 012001 (2009).
- [48] Künzel S, Williams GO, Boutu W, Galtier E, Barbrel B, Lee HJ, Nagler B, Zastrau U, Dovillaire G, W. LR, Merdji H, Zeitoun P, and Fajardo M. *Shot-to-shot intensity and wavefront stability of high-harmonic generation*. Applied optics **54**, 4745–4749 (2015).
- [49] Labat M. *Injection d'un Laser à Electrons Libres : Exemples de SPARC, UVSOR-II et perspectives pour ARC-EN-CIEL*. Thèse, Université Paris Sud, (2008).
- [50] Le Déroff L, Salières P, Carré B, Joyeux D, and Phalippou D. *Measurement of the degree of spatial coherence of high-order harmonics using a Fresnel-mirror interferometer*. Physical Review A **61**, 1–9 (2000).
- [51] M L, P B, MY I, A L, and PB C. *Theory of high-harmonic generation by low-frequency laser fields*. Physical Review A **49**, 2117–2132 (1994).
- [52] Maia FRNC, Ekeberg T, Timneanu N, van der Spoel D, and Hajdu J. *Structural variability and the incoherent addition of scattered intensities in single-particle diffraction*. Physical review. E, Statistical, nonlinear, and soft matter physics **80**, 031905 (2009).
- [53] Malacara D. *Optical Shop Testing*. Wiley Series in Pure and Applied Optics. Wiley (2007). ISBN 9780470135969.
- [54] Mandel L and Wolf E. *Optical Coherence and Quantum Optics*, volume 64. Cambridge University Press, New York (1995). ISBN 0521417112.
- [55] Marchesini S, He H, Chapman H, Hau-Riege S, Noy A, Howells M, Weierstall U, and Spence J. *X-ray image reconstruction from a diffraction pattern alone*. Physical Review B **68**, 1–4 (2003).
- [56] McNulty I, Kirz J, and Jacobsen C. *High-resolution imaging by Fourier transform x-ray holography*. Science (1992).
- [57] Mcpherson A, Gibson G, H J, U J, TS L, IA M, K B, and CK R. *Studies of multiphoton production of vacuum-ultraviolet radiation in the rare gases*. Journal of Optical Society of America B **4**, 595–601 (1987).
- [58] Mejía Y and González AI. *Measuring spatial coherence by using a mask with multiple apertures*. Optics Communications **273**, 428–434 (2007).
- [59] Mercère P, Zeitoun P, Idir M, Pape SL, Levecq X, Dovillaire G, Bucourt S, Goldberg KA, Naulleau PP, and Rekawa S. *Hartmann wave-front measurement at 13.4 nm with  $\lambda_{EUV} / 120$  accuracy*. Optics letters **28**, 1534–1536 (2003).
- [60] Miao J, Sayre D, and Chapman HN. *Phase retrieval from the magnitude of the Fourier transforms of nonperiodic objects*. Journal of Optical Society of America A **15**, 1662–1669 (1998).
- [61] Miao J, Charalambous P, Kirz J, and Sayre D. *Extending the methodology of X-ray crystallography to allow imaging of micrometre-sized non-crystalline specimens*. Nature **400**, 342–344 (1999).
- [62] Miao J, Ishikawa T, Johnson B, Anderson E, Lai B, and Hodgson K. *High Resolution 3D X-Ray Diffraction Microscopy*. Physical Review Letters **89**, 4–7 (2002).
- [63] Mocella V, Brun E, Ferrero C, and Delattre D. *Revealing letters in rolled Herculaneum papyri by X-ray phase-contrast imaging*. Nature communications **6**, 5895 (2015).
- [64] Nagata Y, Furusawa K, Nabekawa Y, and Midorikawa K. *Single-Shot Measurement of Spatial Coherence of 13-nm High-Order Harmonic - Technical Digest (CD)*. In *Conference on Lasers and Electro-Optics/Quantum Electronics and Laser Science Conference and Photonic Applications Systems Technologies*, page JThD1, Long Beach, California, (2006). Optical Society of America.
- [65] Niikura H, Légaré F, and Hasbani R. *Probing molecular dynamics with attosecond resolution using correlated wave packet pairs*. Nature **421**, 0–3 (2003).
- [66] Nishino Y, Takahashi Y, Imamoto N, Ishikawa T, and Maeshima K. *Three-Dimensional Visualization of a Human Chromosome Using Coherent X-Ray Diffraction*. Physical Review Letters **102**, 8–11 (2009).
- [67] Nugent K. *Wave field determination using three-dimensional intensity information*. Physical review letters **68** (1992).
- [68] Park I, Kim Sw, Choi J, Lee D, and Kim Y. *Plasmonic generation of ultrashort extreme-ultraviolet light pulses*. Nature ... **5**, 677–681 (2011).
- [69] Paul PM, Toma ES, Breger P, Mullot G, Audebert F, Balcou P, Muller HG, and Agostini P. *Observation of a train of attosecond pulses from high harmonic generation*. Science (New York, N.Y.) **292**, 1689–92 (2001).
- [70] Platt BC and Shack R. *Wavefront Sensing*. Journal of Refractive Surgery **17** (2003).

- [71] Raimondi L, Svetina C, Mahne N, Cocco D, Abrami A, De Marco M, Fava C, Gerusina S, Gobessi R, Capotondi F, Pedersoli E, Kiskinova M, De Ninno G, Zeitoun P, Dovillaire G, Lambert G, Boutu W, Merdji H, Gonzalez A, Gauthier D, and Zangrando M. *Microfocusing of the FERMI@Elettra FEL beam with a K-B active optics system: Spot size predictions by application of the WISE code*. Nuclear Instruments and Methods in Physics Research Section A: Accelerators, Spectrometers, Detectors and Associated Equipment **710**, 131–138 (2013).
- [72] Raines KS, Salha S, Sandberg RL, Jiang H, Rodríguez Ja, Fahimian BP, Kapteyn HC, Du J, and Miao J. *Three-dimensional structure determination from a single view*. Nature **463**, 214–7 (2010).
- [73] Ravasio a, Gauthier D, Maia F, Billon M, Caumes JP, Garzella D, Géléoc M, Gobert O, Hergott JF, a M. Pena, Perez H, Carré B, Bourhis E, Gierak J, Madouri a, Mailly D, Schiedt B, Fajardo M, Gautier J, Zeitoun P, Bucksbaum P, Hajdu J, and Merdji H. *Single-Shot Diffractive Imaging with a Table-Top Femtosecond Soft X-Ray Laser-Harmonics Source*. Physical Review Letters **103**, 028104 (2009).
- [74] Reusch T, Schülein F. JR, Nicolas J. D, Osterhoff M, Beerlink A, Krenner H. J, Müller M, Wixforth A, and Salditt T. *Collective Lipid Bilayer Dynamics Excited by Surface Acoustic Waves*. Phys. Rev. Lett. **113**, 118102 (2014).
- [75] Röntgen WC. *Eine neue art von strahlen (A new type of radiation)*. Sitzungsberichte der Würzburger Physik-med. (1895).
- [76] Sandberg R, Paul A, Raymondson D, Hädrich S, Gaudiosi D, Holtsnider J, Tobey R, Cohen O, Murnane M, Kapteyn H, Song C, Miao J, Liu Y, and Salmassi F. *Lensless Diffractive Imaging Using Tabletop Coherent High-Harmonic Soft-X-Ray Beams*. Physical Review Letters **99**, 098103 (2007).
- [77] Sansone G, Villoresi P, Altucci C, Velotta R, Stagira S, Silvestri SD, and Nisoli M. *REPORTS Isolated Single-Cycle Attosecond Pulses*. Science **1005**, 443–447 (2006).
- [78] Santarsiero M and Borghi R. *Measuring spatial coherence by using a reversed-wavefront Young interferometer*. Optics Letters **31**, 861–863 (2006).
- [79] Sayre D. *The squaring method: a new method for phase determination*. Acta Crystallographica **5**, 60–65 (1952).
- [80] Sayre D. *Imaging Process and Coherence in Physics*. In et. al. Schlenker, A, editor, *Imaging Process and Coherence in Physics*, volume 112, pages 229–235. Springer, (1980).
- [81] Sayre D, Chapman H, and Miao J. *On the extendibility of X-ray crystallography to noncrystals*. . . . A: Foundations of Crystallography pages 232–239 (1998).
- [82] Schafer K, Yang B Y, Dimauro L, and Kulander K. *Above threshold ionization beyond the high harmonic cutoff*. Physical Review Letters **44**, 2021–2022 (1997).
- [83] Seibert MM, Ekeberg T, Maia FRNC, Svenda M, Andreasson J, Jönsson O, Odić D, Iwan B, Rocker A, Westphal D, Hantke M, DePonte DP, Barty A, Schulz J, Gumprecht L, Coppola N, Aquila A, Liang M, White Ta, Martin A, Caleman C, Stern S, Abergel C, Seltzer V, Claverie JM, Bostedt C, Bozek JD, Boutet S, Miahnahri aA, Messerschmidt M, Krzywinski J, Williams G, Hodgson KO, Bogan MJ, Hampton CY, Sierra RG, Starodub D, Andersson I, Bajt S, Barthelmeß M, Spence JCH, Fromme P, Weierstall U, Kirian R, Hunter M, Doak RB, Marchesini S, Hau-Riege SP, Frank M, Shoeman RL, Lomb L, Epp SW, Hartmann R, Rolles D, Rudenko A, Schmidt C, Foucar L, Kimmel N, Holl P, Rudek B, Erk B, Hömke A, Reich C, Pietschner D, Weidenspointner G, Strüder L, Hauser G, Gorke H, Ullrich J, Schlichting I, Herrmann S, Schaller G, Schopper F, Soltau H, Kühnel KU, Andritschke R, Schröter CD, Krasniqi F, Bött M, Schorb S, Rupp D, Adolph M, Gorkhover T, Hirsemann H, Potdevin G, Graafsma H, Nilsson B, Chapman HN, and Hajdu J. *Single mimivirus particles intercepted and imaged with an X-ray laser*. Nature **470**, 78–81 (2011).
- [84] Sivis M, Duwe M, Abel B, and Ropers C. *Nanostructure-enhanced atomic line emission*. Nature **485**, E1–2; discussion E2–3 (2012).
- [85] Stroke GW and Gabor D. *An introduction to coherent optics and holography*. Academic Press (1969).
- [86] Takahashi Y, Zetsu N, Nishino Y, Tsutsumi R, Matsubara E, Ishikawa T, and Yamauchi K. *Three-dimensional electron density mapping of shape-controlled nanoparticle by focused hard X-ray diffraction microscopy*. Nano letters **10**, 1922–6 (2010).
- [87] Thibault P and Menzel A. *Reconstructing state mixtures from diffraction measurements*. Nature **494**, 68–71 (2013).
- [88] Vartanyants I, Singer A, Mancuso AP, Yefanov OM, Sakdinawat A, Liu Y, Bang E, Williams GJ, Cadenazzi G, Abbey B, Sinn H, Attwood D, Nugent Ka, Weckert E, Wang T, Zhu D, Wu B, Graves C, Scherz A, Turner JJ, Schlotter WF, Messerschmidt M, Lüning J, Acremann Y, Heimann P, Mancini DC, Joshi V, Krzywinski J, Soufli R, Fernandez-Perea M, Hau-Riege S, Peele AG, Feng Y, Krupin O, Moeller S, and Wurth W. *Coherence Properties of Individual Femtosecond Pulses of an X-Ray Free-Electron Laser*. Physical Review Letters **107**, 144801 (2011).
- [89] Vinko SM, Ciricosta O, Cho BI, Engelhorn K, and Chung HK. *Creation and diagnosis of a solid-density plasma with an X-ray free-electron laser*. Nano letters **482**, 59–62 (2012).
- [90] Whitehead LW, Williams GJ, Quiney HM, Vine DJ, Dilanian Ra, Flewett S, Nugent Ka, and McNulty I. *Diffractive Imaging Using Partially Coherent X Rays*. Physical Review Letters **103**, 243902 (2009).

- 
- [91] Williams G, Quiney H, Peele A, and Nugent K. *Coherent diffractive imaging and partial coherence*. Physical Review B **75**, 104102 (2007).
- [92] Witte S, Tenner VT, Noom DW, and Eikema KS. *Lensless diffractive imaging with ultra-broadband table-top sources: from infrared to extreme-ultraviolet wavelengths*. Light: Science & Applications **3**, e163 (2014).
- [93] Zewail A.H. *Femtochemistry: Atomic-scale dynamics of the chemical boundt*. Journal of Physical Chemistry A **104**, 5660–5694 (2000).

